IMT School for Advanced Studies, Lucca

Lucca, Italy

Structural and functional neuroimaging using Quantitative Susceptibility Mapping and ultra-high field Magnetic Resonance Imaging

PhD Program in Cognitive and Cultural Systems

Track in Cognitive, Computational and Social Neuroscience

XXXIII Cycle

Marta Lancione

2021

The dissertation of Marta Lancione is approved.

PhD Program Coordinator: Prof. Pietro Pietrini, IMT School for advanced Studies Lucca

Advisor: Dr. Luca Cecchetti, IMT School for Advanced Studies Lucca

Co-Advisor: Dr. Mauro Costagli, IRCCS Stella Maris, Pisa, Italy; University of Genova, Genova, Italy

The dissertation of Marta Lancione has been reviewed by:

Prof. Luca Roccatagliata, University of Genova, Genova, Italy

Prof. Chunlei Liu, University of California, Berkeley, CA, USA

IMT School for Advanced Studies, Lucca

2021

Contents

Publications

Journal publications resulting from this thesis

Lancione, M., Costagli, M., Handjaras, G., Tosetti, M., Ricciardi, E., Pietrini, P., Cecchetti, L. (2021). *Complementing canonical fMRI with functional Quantitative Susceptibility Mapping (fQSM) in modern neuroimaging research*, NeuroImage, 244, 118574

Lancione, M., Donatelli, G., Cecchi, P., Cosottini, M., Tosetti, M., & Costagli, M. (2019). *Echo-time dependency of quantitative susceptibility mapping reproducibility at different magnetic field strengths.* NeuroImage, 197, 557-564.

Costagli, M., Lancione, M., Cecchetti, L., Pietrini, P., Cosottini, M., Ricciardi, E., & Tosetti, M. (2019). *Quantitative susceptibility mapping of brain function during auditory stimulation.* IEEE Transactions on Radiation and Plasma Medical Sciences, 3(4), 516-522.

Conference abstracts presented during the PhD program [selection]

Lancione M, Costagli M, Handjaras G, Tosetti M, Ricciardi E, Pietrini P, Cecchetti L, *Assessment of functional QSM in advanced experimental paradigms for neuroimaging research*, 38th Annual Scientific Meeting of ESMRMB, 2021 [Oral presentation]

Cencini M, Lancione M, Biagi L, Kurzawski JW, Pasquariello R, Donatelli G, Dosi C, Ticci C, Battini R, Buonincontri G, Tosetti M, *Myelin Water Fraction Mapping in developing children using Magnetic Resonance Fingerprinting*, 29th Annual Meeting of ISMRM, 2021 [Oral – *Magna cum laude* award]

Lancione M, Cencini M, Costagli M, Donatelli G, Tosetti M, Pacchetti C, Cortelli P, Cosottini M, *Quantifying iron deposition in Multiple System Atrophy via multi-echo Quantitative Susceptibility Mapping*, 29th Annual Meeting of ISMRM, 2021 [Poster]

Lancione M, Costagli M, Tosetti M, *Quantitative Susceptibility Mapping of Brain Function at 7T*, Pre-congress workshop of the 27th Annual Meeting of SIPF, Ferrara, Italy, 2019 [Oral]

Lancione M, Buonincontri G, Cecchetti L, Costagli M, Kurzawski J, Ricciardi E, Solana AB, Schulte RF, Tosetti M, *Silent fMRI with visual and auditory stimulation using 3D radial T2*-weighted ZTE-BURST sequence*, 25th OHBM Annual meeting, Roma, Italy, 2019 [Poster]

Lancione M, Donatelli G, Cecchi P, Cosottini M, Tosetti M, Costagli M, *Echo-time-dependent reproducibility of Quantitative Susceptibility Mapping at different field strength*, 27th Annual Meeting of ISMRM, Montreal, Canada, 2019 [Poster]

Lancione M, Buonincontri G, Cecchetti L, Costagli M, Kurzawski J, Ricciardi E, Solana AB, Schulte RF, Tosetti M, *Silent fMRI with visual and auditory stimulation using 3D radial T2*-weighted ZTE-BURST sequence*, 10th Annual Meeting of AIRMM - ISMRM Italian Chapter, Milano, Italy, 2019 [Power pitch]

Lancione M, Lettieri G, Handjaras G, Costagli M, Pietrini P, Cecchetti L and Ricciardi E, *Fine-grained tonotopic architecture is retrieved from resting state connectivity in the auditory cortex*, 19th World Congress of Psychophysiology, Lucca, Italy, 2018 [Poster]

Lancione M, Tosetti M, Cecchi P, Donatelli G, Cosottini M, Costagli M, *Quantitative Susceptibility Mapping at high and ultra-high field: a reproducibility study*, 26th Joint Annual Meeting of ISMRM - ESMRMB, Paris, France, 2018 [Poster]

Lancione M, Tosetti M, Cecchi P, Donatelli G, Cosottini M, Costagli M, *Quantitative Susceptibility Mapping at high and ultra-high field: a reproducibility study*, 9th Annual Meeting of AIRMM - ISMRM Italian Chapter, Padova, 2018 [Oral]

Abstract

In the last decade, Quantitative Susceptibility Mapping (QSM) has been proven a promising Magnetic Resonance Imaging (MRI) tool for the non-invasive quantification of clinically relevant biomarkers, such as iron stores and myelination. The relative simplicity of QSM implementation, which does not require dedicated hardware or acquisition sequence, and its validation with histological evidence favored the diffusion of this technique in the clinical practice, particularly in the diagnosis and follow-up of neurodegenerative diseases. In this thesis, we discussed a critical issue affecting quantification, namely the dependence on acquisition parameters, and its implications for clinical and fundamental research. Specifically, we investigated QSM potential in the study of synucleinopathies, that is a group of neurodegenerative disorders including Multiple System Atrophy (MSA) and Parkinson's disease (PD), and its capability of detecting brain function via functional QSM (fQSM).

As a first step, we assessed how TE-dependence affects QSM intra- and inter-scanner reproducibility by performing repeated measurements on the same participants acquired with both a 3T and a 7T scanner. Then, we explored the impact of TE on the diagnostic accuracy of this technique by acquiring multi-echo data at 7T on MSA patients with Parkinsonian and cerebellar phenotypes and a group of Healthy Controls (HC). In this study, we also assessed the potential of histogram analysis in enhancing QSM diagnostic power. In a third work, we aimed to identify a presymptomatic biomarker in patients at risk for synucleinopathies using 7T QSM. Specifically, we measured and compared iron deposition in nigrosome 1 (a small ovoid-shaped structure located within the dorsolateral portion of the Substantia Nigra pars compacta (SNc)) of PD, idiopathic Rapid Eye Movement (REM) sleep Behavior Disorder (iRBD) patients and HC. Finally, we implemented fQSM and explored its potential compared to fMRI using

7T MRI, a stimulation paradigm for tonotopic mapping, and univariate and multivariate analysis approaches.

Overall, these studies emphasize the importance of QSM in both structural and functional studies and prove that QSM is a versatile and powerful tool for a wide range of neuroimaging applications.

Abbreviations

AC: Anterior Commissure

ARC: Autocalibrating Reconstruction for Cartesian imaging

ASSET: Array Coil Spatial Sensitivity Encoding

AUC: Area Under the Curve

BOLD: Blood Oxygenation Level Dependent

BW: Bandwidth

CBF: Cerebral Blood Flow

CBV: Cerebral Blood Volume

CI: Confidence Interval

CMRO2: Cerebral Metabolic Rate of Oxygen

CN: Caudate Nucleus

COSMOS: Calculation of Susceptibility through Multiple Orientation Sampling

dHb: deoxy-Hemoglobin

DLB: Dementia with Lewy Body

DN: Dentate Nucleus

ePD: early Parkinson's disease

EPI: Echo-Planar Imaging

FA: Flip Angle

fMRI: functional Magnetic Resonance Imaging

FOV: Field Of View

fQSM: functional Quantitative Susceptibility Mapping

FSPGR: Fast SPoiled Gradient Echo

FWHM: Full Width at Half Maximum

GLM: General Linear Model

GM: Gray Matter

GP(i/e): Globus Pallidus (internus/externus)

GRE: Gradient Recalled Echo

H&Y: Hoenh and Yahr score

Hb: Hemoglobin

HC: Healthy Controls

HG: Heschl's Gyrus

HS: Heschl's Sulcus

IR: Inversion Recovery

IRB: Institutional Review Board

iRBD: idiopathic REM sleep Behavior Disorder

iRBD+/-: iRBD with positive/negative T2*-w imaging

iRBD-C: iRBD Converted to synucleinopathies

iRBD-NC: iRBD Not Converted to synucleinopathies

LOOCV: Leave-One-Out Cross-Validation

LOPD: Late-Onset Parkinson's Disease

MDS: MultiDimensional Scaling

MEDI: Morphology Enabled Dipole Inversion

MMSE: Mini-Mental State Examination

MNI: Montreal Neurological Institute

MPRAGE: Magnetization-Prepared Rapid Gradient Echo

MR: Magnetic Resonance

MRI: Magnetic Resonance Imaging

MRS: Magnetic Resonance Spectroscopy

MSA: Multiple System Atrophy

MSAc: Multiple System Atrophy Cerebellar variant

MSAp: Multiple System Atrophy Parkinsonian variant

MSDI: Multi-Scale Dipole Inversion

MVPA: MultiVoxel Pattern Analysis

N1: Nigrosome 1

oHb: oxy-Hemoglobin

PC: Posterior Commissure

PD: Parkinson's Disease

PIGD: Postural Instability Gait Disorder

ppm / ppb: parts per million/billion

pRF: population Receptive Field

PT: Planum Temporale

Pu: Putamen

QSM: Quantitative Susceptibility mapping

RBD: REM sleep Behavior Disorder

rBW: receiver Bandwidth

RDM: Representational Dissimilarity Matrix

REM: Rapid Eye Movement

RN: Red Nucleus

ROC: Receiver Operating Characteristic

ROI: Region Of Interest

RSA: Representational Similarity Analysis

SE: Spin Echo

SHARP: Sophisticated Harmonic Artifact Reduction for Phase Data

SI: International System of Units

SN(c/r): Substantia Nigra (pars compacta/reticulata)

SNR: Signal-to-Noise Ratio

SRA: Sound Responsive Area

STAR-QSM: STreaking Artifact Reduction for QSM

STG: Superior Temporal Gyrus

STI: Susceptibility Tensor Imaging

STN: Subthalamic Nucleus

STS: Superior Temporal Sulcus

SWAN: Susceptibility Weighted ANgiography

TD: Tremor Dominant

TE: Echo Time

Th: Thalamus

TKD: Thresholded k-space Division

TR: Repetition Time

UHF: Ultra-High Field

UPDRS: Unified Parkinson's Disease Rating Scale

WM: White Matter

YOPD: Young-Onset Parkinson's Disease

List of Figures

List of Supplementary Figures

List of Tables

Acknowledgement

This thesis incorporates materials from two published papers and from two papers in progress. At the beginning of each chapter, the corresponding work is cited and coauthors are listed.

A research project is never a solo work and I would like to acknowledge the people who helped me and inspired me during this life-changing journey of professional and personal growth.

Firstly, I would like to thank my supervisor Dr. Luca Cecchetti, for all he taught me and for introducing me to Neuroscience. I owe my deep gratitude to my co-advisor Dr. Mauro Costagli, for his constant availability, guidance and support.

I am grateful to Prof. Pietro Pietrini for teaching me how to be a critical researcher and how to communicate my scientific results. I would also like to thank Dr. Giacomo Handjaras, Prof. Emiliano Ricciardi and, above all, my PhD fellows at IMT.

My sincere gratitude goes to Dr. Michela Tosetti for providing me with the excellent opportunity of performing my research on the 7T scanner. I also want to thank my present and past colleagues in the 7T MRI group, Dr. Laura Biagi, Dr. Graziella Donatelli, Dr. Guido Buonincontri, Dr. Jan Kurzawski, Dr. Paolo Bosco, Emilio Cipriano, Luca Peretti, Paolo Cecchi and Constantin Lipsa for creating a friendly environment in which it has been a pleasure to work. Thanks to Prof. Mirco Cosottini for his help and guidance. I am grateful to all the volunteers, the patients and their families who participated in these studies.

I am extremely thankful to my friends of a lifetime Valentina and Vanessa for their emotional aid during hard times, and to my friends from college for being my family in Pisa and now all over the world.

Lastly, but most importantly, heartfelt thanks go to my family and Matteo for unparalleled support and unconditional love. You are my roots and wings.

Chapter 1 Introduction

1.1 General framework

Since its invention in the early 1970s in the laboratories of Damadian and of the Nobel laureates Lauterbur and Mansfield, Magnetic Resonance Imaging (MRI) has blossomed into an exceptionally dynamic and powerful tool and into an exciting multidisciplinary research field in which physics, chemistry, engineering, neuroscience and medicine merge together.

The success and widespread diffusion of MRI scanners are due to the unprecedented potential of obtaining detailed information on the structure, the function and the metabolism of the human body, and of the brain above all, with a safe and non-invasive procedure. Moreover, the possibility of sensitizing the MR signal to a broad range of tissue properties makes MRI extremely flexible in exploring a variety of biological biomarkers.

During the whole MRI history, manufacturers worked towards the development of MRI scanners incorporating magnets with increasingly higher static magnetic field strength (B_0), progressing from the low field (< 0.5 T) systems used in the 1980s to the 1.5 T and the 3 T clinical system in use nowadays, to the ultra-high field (UHF) (≥ 7 T) scanners developed in the last two decades. The efforts to address the issues conveyed by ultra-high field strength, e.g., field inhomogeneities and higher energy depositions in the tissues, are justified as the two main factors determining image quality, i.e., tissue contrast and Signal-to-Noise Ratio (SNR), increase with field strength. The nearly linear growth rate of SNR with increasing magnetic field intensity can be spent in improving several image properties, depending on the application of interest. In structural imaging, UHF MRI provides images with higher spatial resolution (up to ~100 μm), allowing the depiction of small anatomical structures and their pathological alterations. On the other hand, the gain in sensitivity can be used to improve acquisition time and

time resolution, favoring applications to, e.g., cardiac imaging requiring high frame rate acquisition. Metabolic studies performed via Magnetic Resonance Spectroscopy (MRS) also benefit from higher field strength, as chemical shift among the resonance frequencies of metabolites and spectral resolution show a direct proportionality to B_0. Moreover, UHF MRI opens up new possibilities in multinuclear imaging. The imaging of nuclei other than hydrogen-1 (^{1}H), such as sodium-23 (^{23}Na), phosphorus-31 (^{31}P), oxygen-17 (^{17}O) and carbon-13 (^{13}C), could provide unique information, as they play a critical role in metabolic pathways and cellular processes. MRI of these nuclei at conventional field strength is hindered because of their small gyromagnetic ratio, fast relaxation rate and low concentration in biologic tissue. Nevertheless, UHF MRI boosts the signal of these nuclear species enabling multinuclear imaging in clinically feasible acquisition time. Furthermore, increasing the field strength provides the opportunity to enhance novel contrast mechanisms. In this context, magnetic susceptibility contrast emerged in the last few years as one of the major strong points of UHF MRI.

1.1.1 Magnetic susceptibility

Magnetic susceptibility (χ) is a physical property of materials that measures the degree of their magnetization in the presence of an external magnetic field B_0. Susceptibility is a dimensionless quantity and it is reported in parts per million (ppm) in the International System of Units (SI). The magnetization of a χ source induces a non-local modification of the surrounding B_0 field that is described by the perturbation produced by a magnetic dipole. The dipole field for unit magnetization, depicted in Figure 1.1, is written as follows:

$$D(\boldsymbol{r}) = \frac{1}{4\pi}\frac{3cos^2\theta - 1}{|\boldsymbol{r}|^2} \qquad 1.1$$

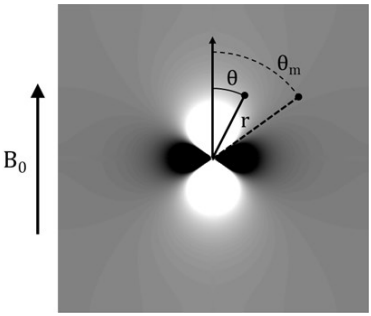

Figure 1.1: Illustration of the magnetic field D(**r**) induced by a unit magnetic dipole described by Equation 1.1. Between the positive and negative lobes, at the so-called magic angle $\theta_m = 54.7°$ with respect to the direction of the external magnetic field, the dipole perturbation D(**r**) takes on zero values.

Biological tissues show weak magnetic behavior ($|\chi| \ll 1$) and the magnetization M is linearly dependent on B_0:

$$M = \chi B_0 \qquad 1.2$$

The magnetic induction B observed in the presence of a susceptibility source is then:

$$B = \mu_0(M + B_0) = \mu_0(1 + \chi)B_0 \qquad 1.3$$

Based on the sign of χ, materials can be divided into paramagnetic (χ>0) and diamagnetic (χ<0) tissues. Diamagnetism is the magnetic effect observed in closed-shells atoms, i.e., that have a null magnetic moment: the external B_0 causes the precession of electrons and the so-generated current induces a macroscopic magnetization opposite to B_0, according to Lenz's law. Hence, in the presence of diamagnetic materials, the resulting magnetic field is decreased. Paramagnetism is found in molecules with an intrinsic magnetic moment: in the presence of an external magnetic field, the magnetic moment aligns with B_0. Macroscopically, this results in a magnetization parallel to the external

field. Hence, in the presence of paramagnetic materials, the resulting magnetic field is increased.

MRI measures susceptibility on a macroscopic scale, i.e., by averaging the concentration of molecules and their effects within a voxel. Biological tissues are mostly composed of water, which is diamagnetic with $\chi_{H_2 0} = -9.053$ ppm [1], thus almost all soft tissues in the body are diamagnetic and their susceptibility generally lies within a range of 10-20% of $\chi_{H_2 0}$ [1]. Therefore, in MRI the terms paramagnetic and diamagnetic are used relative to the susceptibility of water $\chi_{H_2 0}$, rather than that of vacuum. Biological diamagnetic tissues include calcification, lipids in myelin sheath and oxygenated blood while examples of paramagnetic ones are ferritin, hemosiderin and deoxygenated blood.

1.1.2 Magnetic susceptibility effect in MRI

The frequency of precession, i.e., the Larmor frequency, of spins at position **r** in an external magnetic field B is given by the following formula:

$$\omega(\boldsymbol{r}) = \gamma B(\boldsymbol{r}) \qquad 1.4$$

where γ is the gyromagnetic ratio of the hydrogen proton (^{1}H; $\gamma = 2\pi \cdot 42.6 \cdot 10^6 rad\ T/s$).

The distortion of the magnetic field caused by susceptibility sources within and outside themselves affects the image formation process in MRI, as the actual Larmor frequency is different by the expected $\omega_0 = \gamma B_0$. This causes image distortions due to the mapping of spins to erroneous locations [2]. Moreover, local differences in magnetic field cause spins with different Larmor frequencies to dephase with each other during time. Dephasing can be recovered by refocusing the magnetization with Spin Echo (SE) techniques which provide T2-weighted images. When Gradient Recalled Echo (GRE) acquisition sequences are used, dephasing is not recovered, and the effects of magnetic susceptibility become prominent. This represents one of the

main mechanisms at the basis of T2* relaxation. Specifically, the relation existing between the magnetic field perturbations ΔB and T2* is the following:

$$\frac{1}{T_2^*(\boldsymbol{r})} = \frac{1}{T_2(\boldsymbol{r})} + \frac{\gamma}{2}\Delta B(\boldsymbol{r}) \qquad 1.5$$

and the magnitude $M(\boldsymbol{r}, t)$ of the signal measured at position r decays in time as follows:

$$M(\boldsymbol{r}, t) = M(\boldsymbol{r}, 0)e^{-t/T_2^*(\boldsymbol{r})} \qquad 1.6$$

and it is therefore referred to as T2*-weighted.

The susceptibility effect in T2*-weighted images provokes dramatic signal loss, in the presence of both diamagnetic and paramagnetic tissues. These artifacts are more pronounced at the interfaces of two media with noticeably different χ values, e.g., at the air-tissues interfaces at paranasal sinuses or in auditory canals. However, the phase of the GRE signal is linearly dependent on the field perturbation and evolves according to the following:

$$\Delta\phi(\boldsymbol{r}, t) = \gamma\Delta B(\boldsymbol{r})t = \gamma D(\boldsymbol{r}) * \chi(\boldsymbol{r})B_0 t \qquad 1.7$$

where $\Delta\phi(\boldsymbol{r}, t) = \phi(\boldsymbol{r}, t) - \phi(\boldsymbol{r}, 0)$.

The GRE signal phase provides a more direct measurement of susceptibility effect, as it can distinguish between diamagnetic and paramagnetic sources, which exhibit positive and negative phase accumulation respectively. Notably, the magnetic field deformation grows linearly with B_0, making UHF MRI more sensitive to susceptibility differences. However, the information provided by phase imaging is inherently non-local, as the field distortion extends beyond the susceptibility source itself, it is not isotropic and depends on the geometry and orientation of the tissue. The goal of Quantitative Susceptibility Mapping (QSM) is to solve Equation 1.7 for χ spatial

distribution in order to obtain a quantitative and local measurement of an intrinsic tissue property.

1.1.3 Quantitative Susceptibility Mapping (QSM)

One of the main paradigm shifts in MRI is quantitative imaging. Conventional MRI relies mostly on qualitative techniques based on contrast-weighted images: the diagnostic process is based on the visual inspection performed by radiologists that retrieve information from the contrast between different tissues. Besides suffering from the subjective evaluation performed by the specific radiologist, contrast-weighted images show spoiled reproducibility across different exams and scanners, also limiting the potential of longitudinal and multi-center studies. These limitations can be overcome by quantitative MR techniques, consisting in the measurement of intrinsic tissue properties by the removal of spurious contributions to the signal. The signal of a GRE sequence is susceptibility-weighted and QSM aims at removing unwanted contributions in order to get a quantitative map of tissue susceptibility. The conceptual steps of QSM reconstruction are shown in Figure 1.2.

The phase image from GRE acquisition is the starting point for QSM and is computed as the inverse tangent of the ratio of the real and the imaginary part of the signal. Because of the periodicity of the inverse tangent function, raw phases are wrapped over the interval $(-\pi, \pi]$, while the actual phase can take on any value. The wrapping artifact gets more severe in the presence of strong susceptibility variation, e.g., at the air-tissue interfaces, and for long echo times (TE). Phase unwrapping algorithms recover the original phase ϕ from the wrapped one ϕ_{wr}, that are related by the following:

$$\phi(\boldsymbol{r}) = \phi_{wr}(\boldsymbol{r}) + 2\pi n(\boldsymbol{r}) \qquad 1.8$$

with $n(\boldsymbol{r})$ an integer number. Among the several phase unwrapping strategies that have been developed, the Laplacian-based approach [3–5]

is the most frequently adopted in QSM preprocessing pipelines, thanks to its simplicity, robustness to noise and fast computation [6].

The field map $\Delta B(\boldsymbol{r})$ measured by the GRE phase in the area of interest, e.g., the brain, results from the sum of two contributions, i.e., the local field $\Delta B_l(\boldsymbol{r})$ originating by the local susceptibility distribution inside the area of interest, and the background field $\Delta B_b(\boldsymbol{r})$ induced by other sources. These contributions include high susceptibility variations (about 9 ppm) [1] at air-tissue interfaces at the outer surface of the head or in inner areas such as sinus cavities, χ differences from structures of no interest, e.g., the skull, B_0 inhomogeneities and macroscopic currents, e.g., in MRI shim coils [7]. The background field is usually dominant (i.e., one order of magnitude larger than local fields) and needs to be removed. After selecting the area of interest via a masking operation, background field removal is usually performed via Laplacian-based methods, such as Sophisticated Harmonic Artifact Reduction for Phase data (SHARP) [8] that exploits the spherical mean value property of harmonic functions.

After these preprocessing steps, QSM aims to solve the phase-to-susceptibility inverse problem. Equation 1.7 can be transformed into the k-space domain via Fourier transform to obtain the following:

$$\chi(\boldsymbol{k}) = \frac{\phi(\boldsymbol{k})}{\gamma B_0 D(\boldsymbol{k})\mathrm{TE}} \tag{1.9}$$

where TE is the echo time at which the signal is sampled and

$$D(\boldsymbol{k}) = \frac{1}{3} - \frac{k_z^2}{|\boldsymbol{k}|^2} \tag{1.10}$$

is the Fourier transform of Equation 1.1, that is the dipole convolution kernel for a point source of susceptibility, being $\boldsymbol{k}$ a k-space vector and k_z its component along the direction of B_0. $D(\boldsymbol{k})$ takes on zero values when $|\boldsymbol{k}|^2 = 3k_z^2$, i.e., when the angle between the **k**-vector and B_0 is equal to 54.7° or 125.3° (Figure 1.1), the so-called magic angles, creating a cone of singularities in which Equation 1.9 cannot be solved via a direct

division. Hence, the QSM inverse problem is ill-posed and its computation leads to artifacts in the reconstructed χ maps. The gold standard for QSM reconstruction is known as Calculation of Susceptibility through Multiple Orientation Sampling (COSMOS) [9] and requires the acquisition of images with the subject's head rotated at multiple orientations. This procedure allows filling the missing data inside the cone of singularities at the magic angles of one orientation using data acquired in the others. However, this method is unfeasible in clinical settings because of patients' discomfort and long scanning time. For this reason, several single orientation approaches have been proposed to solve the ill-posed inverse problem and suppress streaking artifacts, such as Thresholded k-space Division (TKD) [10,11], iLSQR [12,13], STAR-QSM [14], Morphology Enabled Dipole Inversion (MEDI and MEDI+0) [15,16] and Multi-Scale Dipole Inversion (MSDI) [17], as well as the novel deep learning-based methods [18,19].

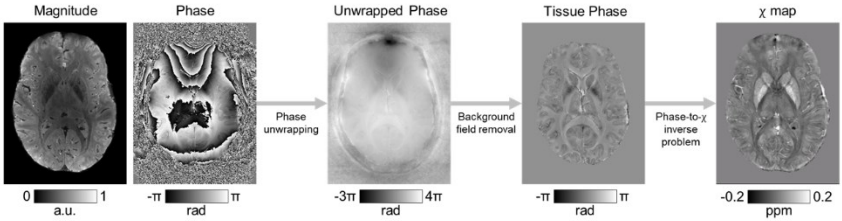

Figure 1.2: Reconstruction pipeline of susceptibility maps. The raw images obtained from a GRE acquisition are the magnitude and phase shown on the left. The phase undergoes the following processing steps in QSM: phase unwrapping, background field removal and finally the deconvolution of the dipole kernel (Equation 1.9).

1.1.4 QSM potentials and pitfalls

QSM can non-invasively provide a local and quantitative measurement of a physical tissue property. One of its first clinical applications consisted in the discrimination between calcifications and hemorrhages

[20], i.e., between diamagnetic and paramagnetic lesions that appear indifferently as hypointensities in T2*-weighted images. Moreover, QSM provides unprecedented views of brain morphology, depicting structures such as basal ganglia and brainstem structures with exceptional anatomical detail [21,22], and representing a potential tool for the optimization of pre-surgical planning in deep brain stimulation [23,24]. Histological studies in humans and ex-vivo experiments on animal models assessed the correlation between measured susceptibility values and biomarkers of paramount importance, such as iron stores [25–27] and myelination [28–31]. The quantitative assessment of biomarkers provides the opportunity to perform longitudinal evaluation and follow-up in clinical settings and in multi-center studies. QSM is then gaining increasing importance in the study of many developmental, aging and pathological processes and it is entering clinical practice. Brain tumors [32,33] and traumatic brain injuries [34,35] are two examples of clinical applications that can benefit from this technique, but nowadays the research field in which QSM is most widely spreading is the study of neurodegenerative disorders [36,37], e.g., Alzheimer's disease [38–42], Parkinson's disease [43,44,53,45–52], amyotrophic lateral sclerosis [54–60], Wilson's disease [61–63], Huntington's disease [64–66], multiple sclerosis [31,67–69] and Friedreich's ataxia [70–72]. It was demonstrated that QSM can detect increased magnetic susceptibility in brain regions involved in the pathological processes corresponding to each disorder, indicating iron accumulation, and susceptibility values correlate with disease duration and with clinical scores associated with disease severity.

In this thesis, QSM was performed on healthy controls and on patients with Parkinson's disease or atypical Parkinsonism to explore its diagnostic performance. In this clinical framework, the quantitative assessment of susceptibility can be a powerful tool for longitudinal follow-up and for the diagnosis and the differential diagnosis of these populations of patients, which is often challenging.

One of the main drawbacks of QSM concerns the erroneous implicit assumption that χ is a scalar quantity. It was observed that, in the

presence of highly organized microstructures, measured susceptibility depends on the orientation of the tissues with respect to the external magnetic field. In fact, magnetic susceptibility is a second-order tensor, whose complete estimation requires at least six acquisitions with the patient's head oriented along different directions with respect to B_0. This approach, known as Susceptibility Tensor Imaging (STI) [73–75], , would provide a more accurate assessment of the magnetic properties of the tissues but it is not suitable for clinical applications due to dramatically long acquisition time and patient discomfort. Even though in single acquisition QSM protocols susceptibility anisotropy impairs QSM accuracy, in the brain this issue is mainly limited to white matter, due to the highly ordered anisotropic lipid molecules constituting the myelin sheath [76–78].

It has to be noticed that, even though QSM ability to distinguish between calcified and hemorrhagic lesions facilitates the diagnosis process, the disentanglement of myelin and iron content is a challenging issue. Measured susceptibility results from the interplay of multiple contributions as brain tissues present complex composition and organization. Iron in white matter oligodendrocytes and mitochondria and myelinated fibers in deep gray matter nuclei represent confounding factors in the evaluation of myelination and iron stores respectively. An interesting example is provided by multiple sclerosis plaques in which the processes of demyelination and iron accumulation may colocalize [79,80]. Other quantitative techniques, patient history and clinical evaluation should be combined with QSM in order to disentangle each contribution and establish the source of susceptibility alteration. In this context, the emerging research line of sub-voxel multi-component imaging may prove useful in probing structure heterogeneity at a sub-voxel level.

Another limitation of susceptibility mapping is that it can quantify susceptibility only with respect to a reference value rather than in absolute terms, since the maps have an unknown region-independent offset due to the singularity of the k-space kernel (Equation 1.10) at the origin of k-space ($\boldsymbol{k} = 0$) [81,82]. Hence, χ values have to be referred to a

reference region that should be easy to delineate and ideally not affected by age, disease and head orientation. Several brain structures have been suggested [83,84], including cerebrospinal fluid in the ventricles, frontal white matter, internal capsule or the whole brain average. However, it was observed that this correction represents a negligible adjustment [85] with respect to other effects such as aging and it was suggested to keep susceptibility values unreferenced in order to avoid making assumptions on brain areas spared by the disease.

An issue that has to be tackled in clinical practice concerns physiological motion. Whole-brain acquisitions for susceptibility mapping require long scanning time and patient motion and physiological fluctuations (e.g., respiration, blood flow and oxygenation changes) introduce phase shifts that compromise the accuracy of χ maps [86]. Prospective motion correction approaches [87,88] have been recently applied to QSM and proved successful in image quality improvement and artifacts reduction.

1.1.5 QSM dependence on echo time

An important issue that needs to be addressed concerns the dependence of the accuracy of χ quantification and its reproducibility on some acquisition settings, such as voxel size and anisotropy, spatial coverage [89,90] and echo time [91,92]. In order to shorten scanning time, acquisition sequences employed in clinical imaging are often prescribed with partial brain coverage, thick slices and large spacing. This results in reduced susceptibility contrast and in underestimated χ values with increasing slice thickness and spacing and with decreasing coverage [90,93–95]. Moreover, echo time is usually set to its scanner default value with no targeted optimization. The SNR of phase images is maximized when TE equals the T2* relaxation time of the tissue of interest but χ values obtained via QSM should theoretically be inherently TE-independent, as phase accumulation is assumed to be a linear process in time (Equation 1.7). However, inconsistently with this assumption, susceptibility of several brain regions in both white and gray matter was reported to be variable when calculated from different TEs of multi-echo

acquisitions [91,92]. These variations reach up to 100 parts per billion (ppb) in intact tissues and beyond 1000 ppb in cerebral microbleeds [92].

Factors that can possibly flaw the assumption of linear phase evolution at the basis of QSM reconstruction are related to those responsible for multi-exponential T2* decay: sub-voxel compartmentalization, tissue composition and microstructures, which are not modeled in Equation 1.7 [91,96–98]. While multi-component fittings in gray matter are particularly challenging due to its complex microstructure, attempts at modelling white matter signal were performed via a three-pool (axonal, myelin, and extra-axonal space) hollow cylinder model [96,99]. However, it failed to explain QSM signal behavior at short TEs [92], suggesting the existence of a shorter T2* component that is missing in the model, whose contribution to the phase rapidly vanishes over time. Moreover, this simple model did not take complex geometrical factors into account, such as the variable orientation and curvature and the irregular cross-section size and shape of the white matter fibers that are found within a voxel.

It was also demonstrated that TE-dependence is not attributable to artifacts introduced by algorithms for background field removal and dipole field inversion, but voxelwise-unwrapped data show notably reduced χ variability compared to Laplacian-unwrapped data [92]. This was attributed to the subtraction of the phase of the first echo which may remove the contributions from rapidly decaying components, reinforcing the hypothesis of a biophysical origin of this effect [92].

As it raises important concerns on the accuracy of this technique, the TE-dependence of QSM needs to be addressed in order to guarantee reproducibility. On the other hand, further exploration of this effect in multi-echo GRE acquisition may provide information on sub-voxel microstructure, which could be exploited to maximize diagnostic accuracy. The study of the influence of TE-dependence on reproducibility and diagnostic power of QSM was part of this thesis project and will be further discussed in the following chapters.

1.1.6 Magnetic susceptibility of hemoglobin

Hemoglobin (Hb) is an iron-containing protein in red blood cells that is responsible for carrying oxygen to cells from the lungs. Due to its molecular structure and to the reconfiguration it undergoes when binding or releasing oxygen, hemoglobin shows peculiar magnetic properties. The structure of a molecule of deoxyhemoglobin is approximately spherical and consists of four protein chains each containing one paramagnetic iron ion (Fe++). It can bind four paramagnetic oxygen molecules and undergo an extreme structural change resulting in an oxyhemoglobin molecule with no net spin, which is therefore diamagnetic [1,100]. This variability of the magnetic properties of hemoglobin linked to oxygenation can be observed via T2*-weighted images and measured through QSM. As it is the dominant contribution to blood susceptibility and it relates to physiological and physiopathological processes, it represents a useful and informative biomarker.

Blood fractional oxygen saturation Y, i.e., a physiological parameter describing the amount of oxygen dissolved in blood, can be estimated from the difference in susceptibility between blood and the surrounding parenchymal tissues $\Delta\chi_{blood-water}$ via the following:

$$\Delta\chi_{blood-water} = \Delta\chi_{do} \cdot \mathrm{Hct} \cdot (1 - Y) \qquad 1.11$$

where Hct is the hematocrit, that is the volume fraction of red blood cells whose average value is 0.4 [101], $\Delta\chi_{do} = \Delta\chi_{deoxy} - \Delta\chi_{oxy} = 3.39$ ppm (in SI units) [102,103] is the susceptibility difference between fully deoxygenated and oxygenated blood per unit hematocrit [104]. The mapping of blood oxygenation saturation may help in understanding processes undergoing pathological conditions such as strokes [105,106] and tumors [107].

1.1.7 BOLD effect and functional QSM

The difference in susceptibility between deoxy- and oxy-hemoglobin is the basic physical principle of Blood Oxygenation Level Dependent (BOLD) effect exploited in functional MRI (fMRI) and schematized in Figure 1.3. Brain metabolism requires a continuous supply of oxygen and glucose, which is provided by Cerebral Blood Flow (CBF). When a portion of the brain is involved in a task, the consumption of glucose and the Cerebral Metabolic Rate of Oxygen consumption (CMRO2) are increased and their necessary intake is ensured by an increase in CBF and in Cerebral Blood Volume (CBV). This interaction between neural activity and vascular response is known as neurovascular coupling. The increase in CMRO2 is counterbalanced and overcome by the increase in CBV and CBF, leading to a net increase in blood oxygenation, making the tissue hyperoxic. Due to oxyhemoglobin diamagnetism, the tissue becomes less paramagnetic when involved in neural activity than at rest, leading to an increase in the intensity of T2*-weighted images. Hence, hemoglobin acts as an endogenous magnetic contrast agent, leaving a fingerprint on the GRE signal which depends on the functional state of the tissue. In conventional fMRI, brain activity is revealed by the variation in signal intensity but this information is neither quantitative nor local, as it relies on T2*-weighted images and suffers from the blooming effect due to dipole field perturbation.

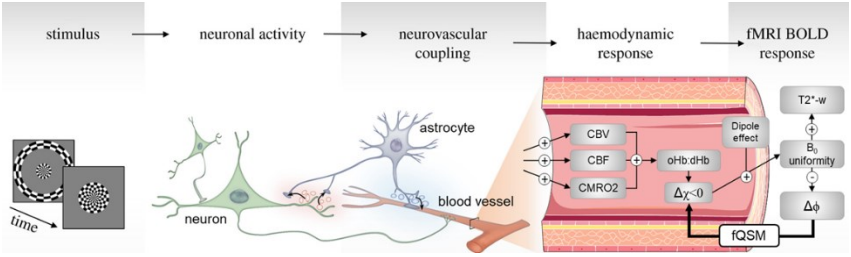

Figure 1.3: Schematic illustration of the biophysical principles of BOLD effect. Following stimulation, e.g., visual stimulation with a contracting checkerboard ring on gray background, the neuronal activity elicits a response of the vascular

system via a mechanism known as neurovascular coupling, which gives rise to the hemodynamic response. The interplay between the increase in Cerebral Blood Flow and Volume (CBF and CBV) and the increase in Cerebral Metabolic Rate of Oxygen (CMRO2) results in a net increase of oxy-hemoglobin (oHb) with respect to deoxy-hemoglobin (dHb), making the tissue less paramagnetic ($\Delta\chi<0$). The inhomogeneities of the static magnetic field diminish in the correspondence of the susceptibility source and, because of the magnetic dipole effect, in its surroundings. Hence, the T2*-weighted signal, i.e., the magnitude of the GRE signal, increases while the phase shift is reduced. fQSM enables the reconstruction of $\Delta\chi$ maps, by removing the non-local dipole effect and providing a measurement that is closer to the actual hemodynamic response with respect to conventional fMRI. Part of this figure was adapted and modified from Tsvetanov et al., 2021 (CC BY 3.0) [108] and from Servier Medical Art (CC BY 4.0) [109].

The use of QSM in functional studies can address both issues and allow a more direct assessment and a more precise localization of brain activity, by measuring from the phase signal the susceptibility changes that underlie magnitude signal variation (Figure 1.3). The feasibility of this novel strategy called functional QSM (fQSM) was recently assessed [95,110–115], showing that it can extract complementary information to fMRI from the same complex-valued time series. Importantly, the signals of fMRI and fQSM are inversely correlated, as the increase in signal intensity following brain activity is due to a decrease in tissue susceptibility. One of the research lines of this thesis deals with the characterization of this technique and its applicability in a state-of-the-art neuroimaging scenario.

1.2 Aims and structure of this thesis

This thesis project is structured into three major research lines focusing on potentials and pitfalls of QSM from a methodological perspective (Chapters 2 and 3), on its application in the clinical practice (Chapters 3 and 4), and on its implementation in functional studies (Chapter 5).

In the last decade, QSM has been proven a promising technique, thanks to the improvement of reconstruction algorithms on the one hand and

its assessment as a powerful histologically-validated diagnostic tool for a variety of disorders on the other. However, some concerns were raised regarding the influence of acquisition parameters on χ measurements, that could impair the accuracy and the reproducibility of this technique. Thus, it is critical to further explore these confounding factors and be aware of their effect, in order to exploit the full potential of QSM in longitudinal and multi-center studies.

In light of this, we investigated the impact of echo time on the reproducibility of QSM at two different strengths of the static magnetic field, i.e., using a clinical 3T and a 7T MRI system from the same vendor. It has been shown that UHF MRI is more sensitive to the susceptibility effect yielding higher SNR and contrast, which can be crucial in finding new biomarkers. However, as no additional or dedicated sequences and hardware are required to perform QSM, it is growingly spreading in clinical protocols performed at lower field strength, i.e., 1.5T and 3T. To allow for a comparison between findings obtained at different magnetic fields, it is important to ensure reproducibility across scanners and assess which sets of echo times maximize the detection of changes in susceptibility. This work is presented in Chapter 2.

Chapter 3 shows the effects of this acquisition parameter on the clinical application of QSM. Specifically, we highlighted how TE-dependence influences not only χ values but also the diagnostic performances of QSM. To this purpose, we acquired a multi-echo GRE sequence on a 7T scanner and compared the susceptibility in deep gray matter nuclei of Multiple System Atrophy (MSA) patients and healthy controls at each individual TE. We also explored the potential of histogram analysis, which may provide further insight on pathological processes, by revealing information not just on the overall iron deposition but also on its pattern heterogeneity.

A further project on the employment of QSM as a diagnostic tool in the clinical setting was carried out on a 7T MRI system to establish biomarkers for the diagnosis and the differential diagnosis of patients with Parkinson's Disease (PD) and Rapid Eye Movement (REM) sleep Behavior Disorder (RBD). Susceptibility values in Nigrosome 1 (N1)

were compared between healthy controls and the two groups of patients and were also correlated with disease duration. This study is reported in Chapter 4.

The last research line, presented in Chapter 5, concerns the translation of QSM to functional studies via fQSM, with a focus on the characterization of activations and on its potential in the discrimination of brain responses evoked by different perceptual stimulus features. In fact, to date only simple "On/Off" stimulation experiments and conventional analysis techniques (e.g., the classic mass-univariate General Linear Model - GLM) have been applied to fQSM studies. Here, we assessed fQSM performances at 7T with a complex auditory stimulation paradigm under different analysis approaches, ranging from the classic GLM to state-of-the-art techniques such as population Receptive Field method (pRF) and Multivoxel Pattern Analysis (MVPA).

The final Chapter 6 summarizes the main results of this thesis and discusses their potential implications for future research.

1.3 Contributions to this work

The work presented in this thesis resulted in four first-authored manuscripts and it is the outcome of a choral and collaborative effort of several interdisciplinary research groups. The institutions involved in this project are the following:

- Molecular Mind Laboratory (MoMiLab), IMT School for Advanced Studies Lucca (Lucca, Italy);
- IMAGO7 Research Center (Pisa, Italy);
- Laboratory of Medical Physics and Magnetic Resonance, IRCCS Stella Maris (Pisa, Italy);
- Neuroradiology Unit, University Hospital of Pisa (Pisa, Italy);
- Neurology Unit, University Hospital of Pisa (Pisa, Italy);
- Parkinson and Movement Disorder Unit, IRCCS Mondino Foundation (Pavia, Italy);
- Department of Biomedical and NeuroMotor Sciences, University of Bologna (Bologna, Italy)

- Neurological Clinic, IRCCS Institute of Neurological Sciences of Bologna (Bologna, Italy)

The 7T MR images employed in this thesis were acquired at the IMAGO7 Research Center in Pisa, while the 3T MR images were acquired at the Neuroradiology Unit of the University Hospital of Pisa.

Chapter 2 Echo-time dependency of quantitative susceptibility mapping reproducibility at different magnetic field strengths

The study presented in this chapter was conducted thanks to the collaboration of the Neuroradiology Unit of the University Hospital of Pisa (Pisa, Italy), IRCCS Stella Maris and the IMAGO7 Research Center (Pisa, Italy).

This work has been published as follows [116]:

Lancione, M., Donatelli, G., Cecchi, P., Cosottini, M., Tosetti, M., Costagli, M., (2019). *Echo-time dependency of quantitative susceptibility mapping reproducibility at different magnetic field strengths.* Neuroimage 197, 557–564.

2.1 Abstract

Quantitative Susceptibility Mapping (QSM) provides a way of measuring iron concentration and myelination non-invasively and has the potential of becoming a tool of paramount importance in the study of a host of different pathologies. However, several experimental factors and the physical properties of magnetic susceptibility (χ) can impair the reliability of QSM, and it is therefore essential to assess QSM reproducibility for repeated acquisitions and different field strength. In particular, it has recently been demonstrated that QSM measurements strongly depend on echo time (TE): the same tissue, measured on the same scanner, exhibits different apparent frequency shifts depending on the TE used. This study aims to assess the influence of TE on intra-scanner and inter-scanner reproducibility of QSM, by using MRI systems operating at 3T and 7T. To maximize intra-scanner reproducibility, it is necessary to match the TEs of the acquisition protocol, but the

application of this rule leads to inconsistent QSM values across scanners operating at different static magnetic field. This study however demonstrates that, provided a careful choice of acquisition parameters, and in particular by using TEs at 3T that are approximately 2.6 times longer than those at 7T, highly reproducible whole-brain χ maps can be achieved also across different scanners, which renders QSM a suitable technique for longitudinal follow-up in clinical settings and in multi-center studies.

2.2 Introduction

Quantitative Susceptibility Mapping (QSM) [10,94,117–121] provides a way of measuring tissue magnetic susceptibility (χ) non-invasively by means of Magnetic Resonance Imaging (MRI). QSM enables a quantitative characterization of myelination [28,29] and of the concentration of calcium, iron [25] and blood compounds like hemoglobin, and therefore it has opened new possibilities in the study of a host of different pathologies including, for example, neurodevelopmental disorders, brain tumors, and neurodegenerative diseases [32,38,49,55,57,68]. The increasing importance of QSM in medical research and its use in the clinical practice make reproducibility an important issue.

Tissues with magnetic susceptibility introduce, in their surroundings, microscopical distortions of the static magnetic field B_0. These B_0 inhomogeneities cause shifts in the local resonance frequency that are reflected in the MR signal phase, and QSM images are obtained from the frequency shift maps by deconvolving out the magnetic dipole field generated by susceptibility sources. In general, it is assumed that one voxel is a point (one-dimensional) susceptibility source containing one single chemical species: therefore, the signal phase ϕ of one voxel is generally assumed to linearly follow B_0 and the acquisition echo time (TE), as described in the following relation in the k-space [11]:

$$\tilde{\phi}(\mathbf{k}) = -\gamma \, \mathrm{B_0 TE} \, \mathrm{D}(\mathbf{k}) \cdot \tilde{\chi}(\mathbf{k}) \qquad 2.1$$

The symbol "~" indicates the 3D Fourier transform, and $\boldsymbol{k}$ represents the k-space vector; γ is the gyromagnetic ratio and B_0 is the main magnetic field; $D(\boldsymbol{k}) = \left(\frac{1}{3} - \frac{k_z^2}{|\boldsymbol{k}|^2}\right)$ represents the Fourier transform of the dipole convolution kernel for a point source of susceptibility, being k_z the k-space vector component along the direction of B_0.

However, several experimental factors may impair the reliability of QSM as a quantitative tool in multi-center studies and for longitudinal follow-up: an important role is played by the physical properties of magnetic susceptibility itself, such as χ anisotropy [76–78], which make subject positioning an important aspect; moreover, to maximize the QSM reproducibility it is also important to match acquisition parameters, such as coverage [89,90], spatial resolution [90,93], and echo times (TE) [91,92] across different sessions. In particular, it has been shown that the phase signal in brain tissues, including deep gray matter nuclei and white matter regions, exhibits different nonlinear behaviors as a function of TE, which are possibly caused by factors such as sub-voxel compartmentalization, tissue composition and microstructure [91,96–98], that are not taken into account in the model described by Equation 2.1. The extent of this TE-dependency, previously studied at 3T, is such that QSM values can vary up to approximately 100 ppb in intact tissues, and beyond 1000 ppb in the presence of cerebral microbleeds [92]. The interplay between phase contributions colocalizing in the same voxel is not trivial, not only for varying TE, but also at different operating field strengths.

Taken together, these considerations drive the motivation to especially investigate the case where scanners operating at different field strength are involved, because in such a scenario the choice of TEs might be crucial to obtain reproducible QSM results. Due to the higher signal- and contrast-to-noise ratio achievable with scanners operating at ultra-high field strength, many researchers attempted to find biomarkers for diseases by using 7T MRI systems [43,55,64,122–128]. To relate these results to the growing amount of findings obtained with QSM at clinical field strength [38,44,49,57,67,68,129], it is crucial to ensure the reproducibility of susceptibility measures across scanners. Multi-center

studies have been carried out on 1.5T and 3T scanners on both healthy subjects and patients [17,84,130–134]. At fields ≥ 7T, QSM reproducibility was quantitatively investigated only using phantoms [135], while in-vivo it was assessed only qualitatively [17].

Here we aim to assess the influence of echo time on intra-scanner and inter-scanner reproducibility of QSM acquired on healthy subjects using MRI systems operating at 3T and 7T.

2.3 Methods

2.3.1 Subjects

Five volunteers (S1~S5, aged 26-41, 32 ± 6 years, two females) with no history of neurological diseases or psychiatric disorders participated to this study, with their understanding and written consent in accordance with the protocol approved by the competent ethics committee, and in compliance with national legislation and the Declaration of Helsinki.

2.3.2 MRI acquisition hardware

All subjects underwent both 3T and 7T MRI examinations, using scanners from the same vendor (systems GE-MR750 and GE-MR950, respectively, both manufactured by GE Healthcare, Milwaukee, Wisconsin, U.S.A.). Both scanners were equipped with the same gradient system (maximum amplitude = 50 mT/m; slew rate = 200 mT/m/ms). On the 3T scanner, radiofrequency power was transmitted with the system's body coil, while the MR signal was acquired with an 8-channel receive-only head coil. On the 7T scanner, a two-channel transmit / 32-channel receive head coil (Nova Medical, Wilmington, MA, U.S.A.) was used.

2.3.3 Data acquisition

Each subject underwent four QSM examinations (two at 3T and two at 7T) within one month. All QSM data were acquired by using a 3D

Gradient-Recalled Multi-Echo sequence (product name: SWAN) prescribed axially with whole-brain coverage, with the subject lying in supine position. The two 3T scans (hereafter referred to as "3T1" and "3T2") and the two 7T scans (referred to as "7T1" and "7T2") were acquired in different examinations, therefore with slightly different head position, pre-scan and shimming steps. All scans shared the following acquisition parameters: Time of Repetition TR=54.1ms, receiver bandwidth rBW = 100 kHz, 11 echo times equally spaced between 5ms to 42ms, flip angle (FA) = 15°, parallel imaging ASSET (Array Coil Spatial Sensitivity Encoding) acceleration factor = 2, flow compensation. All scans had voxel size of 1 mm^3 isotropic, obtained by using acquisition matrices of sizes equal to the extent, in mm, of the Field Of View (FOV): at 3T, the in-plane FOV was 240 mm (frequency encoding along the posterior-anterior direction) × 192 mm (phase encoding along the left-right direction) with acquisition matrix of size 240 × 192 (scan duration: 9min 56s), while at 7T the FOV was 240 × 168 mm^2 with matrix of size 240 × 168 (scan duration: 8min 30s). The prescriptions included the entire brain of all subjects, with the same coverage of 158 mm in the inferior-superior direction. Both the real and imaginary parts of the images obtained at each echo were saved and converted into phase and magnitude data.

For anatomical reference, 3D T_1-weighted images with isotropic spatial resolution of 1mm^3 were obtained for all subjects by using an inversion recovery (IR) fast spoiled gradient recalled (FSPGR) sequence prescribed sagittally on the 3T scanner. The acquisition parameters were: TE = 5.6 ms, TR = 54.1 ms, matrix size = 256 × 256 × 170, FA = 12°, receiver bandwidth = 62.5 kHz, parallel imaging ARC (Autocalibrating Reconstruction for Cartesian imaging) acceleration factor = 2.

2.3.4 Data processing

Data processing and analysis were performed using FSL 5.0.9 [136] (FMRIB Software Library, Oxford Centre for Functional MRI of the Brain, Oxford, UK) and MATLAB 2017a (Mathworks, Natick, MA, USA).

QSM images were obtained as follows, with the same processing pipeline for both 3T scans and 7T scans. First, T_2*-weighted images from each of the SWAN acquisitions were generated by averaging the magnitude images of all the echoes, and were used to obtain brain masks by using FSL (Brain Extraction Tool BET [137] followed by an erosion step using a flat disk-shaped structuring element with a radius of 3 mm). The raw phase images of individual echoes underwent the following procedure by using STI Suite (MATLAB code from UC Berkeley, Berkley, CA, USA) [138]. Phases were unwrapped using a Laplacian-based algorithm [3,12] and the brain masks were used for the removal of the background field via V-SHARP [8]. The iLSQR [12,13] method was applied to the processed phase of each individual echo separately to compute χ maps. One average QSM, obtained by averaging the χ maps obtained for each echo of one acquisition, was also computed [139].

2.3.5 Data analysis

Reproducibility was assessed via a voxel-wise analysis, conducted on each individual subject separately. The four SWAN datasets of each subject were co-registered to first one acquired at 3T via FSL-FLIRT [136] by using nearest neighbor interpolation. All voxels inside the subject's brain mask were considered, and the orthogonal linear fit and Pearson's correlation for each pair of TEs were computed. For each TE of one scan, the corresponding TE in another scan that maximized QSM reproducibility was selected as the one that produced the angular coefficient m closest to 1, obtained by linear regression. The optimal pairs of TEs between scans were linearly fitted to obtain the relationship between TEs that maximized reproducibility. A leave-one-out cross-validation (LOOCV) approach was adopted. The TEs that maximize reproducibility were identified on the aggregate dataset of all-but-one subjects, and were applied on the left-out subject. The procedure was repeated for every subject.

2.4 Results

Typical QSM images obtained at 3T and 7T by averaging susceptibility maps across TEs are displayed in Figure 2.1 for one representative subject (S4).

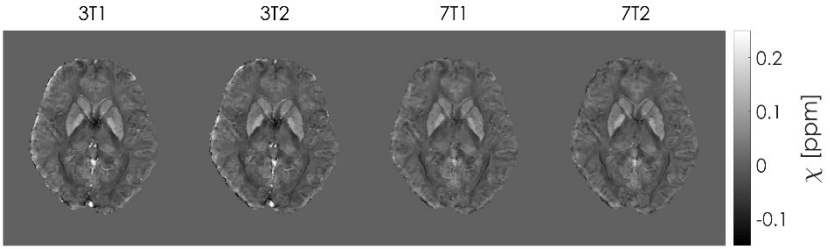

Figure 2.1. Susceptibility maps computed as the average of QSM images across TEs for each scan for one representative subject (S4). The labels 3T1, 3T2, 7T1 and 7T2 indicate the first and the second QSM acquisition performed at 3T and 7T respectively.

The scatter plots in Figure 2.2 demonstrate the excellent intra-scanner reproducibility of χ maps obtained this way on that subject (panels A and B).

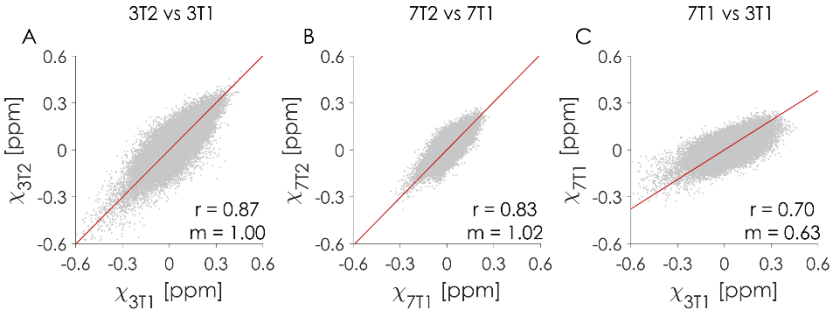

Figure 2.2. Scatter plots show a comparison between QSM measurements from the whole brain in different scans (gray dots) for one representative subject (S4).

The red line shows the result of the orthogonal linear fit. Excellent intra-scanner reproducibility (m~1) is observed for both 3T and 7T acquisitions (panels A and B) but inter-scanner reproducibility is considerably lower (panel C).

Values of m and r for all subjects for both intra-scanner analyses are reported in Tables 2.1 and 2.2. The average values of m across subjects were 1.01 ± 0.09 for scans at 3T and 1.00 ± 0.01 at 7T, while the average values of r were 0.78 ± 0.07 at 3T and 0.83 ± 0.03 at 7T. QSM intra-scanner reproducibility was therefore better at 7T than at 3T, as testified also by the average confidence intervals C.I. of the quantitative measures of χ (C.I. = 0.055 ± 0.009 ppm at 3T and 0.034 ± 0.003 ppm at 7T) obtained by a Bland-Altman analysis. On the contrary, inter-scanner reproducibility was very limited (Figure 2.2, panel C), with average angular coefficient across subjects m = 0.61 ± 0.04, significantly smaller than the ideal value m = 1. Values of m and r for all subjects for inter-scanner analyses are shown in Table 2.3.

The intercepts computed by linear fitting were of the order of 1 ppb or less.

	m	**q [ppm]**	**r**	**CI [ppm]**
Subject 1	1.06	0.0002	0.77	0.05
Subject 2	0.86	0.0013	0.68	0.07
Subject 3	1.03	-0.0006	0.81	0.05
Subject 4	1.00	0.0002	0.87	0.04
Subject 5	1.09	0.0004	0.75	0.06

Table 2.1. Intra-scanner reproducibility at 3T. Slope m, intercept q and Pearson's correlation coefficient r that characterize QSM reproducibility in two datasets acquired for each subject on the same 3T scanner. Confidence intervals C.I. of the quantitative measures of χ are also indicated.

	m	q [ppm]	r	CI [ppm]
Subject 1	0.99	0.00011	0.83	0.033
Subject 2	1.01	0.00008	0.87	0.029
Subject 3	0.99	-0.00003	0.80	0.038
Subject 4	1.02	-0.00002	0.83	0.035
Subject 5	1.01	-0.00008	0.82	0.035

Table 2.2. Intra-scanner reproducibility at 7T. Slope m, intercept q and Pearson's correlation coefficient r that characterize QSM reproducibility in two datasets acquired for each subject on the same 7T scanner. Confidence intervals C.I. of the quantitative measures of χ are also indicated.

	m	q [ppm]	r
Subject 1	0.62	0.00023	0.62
Subject 2	0.53	0.00008	0.62
Subject 3	0.63	-0.00009	0.67
Subject 4	0.63	-0.00008	0.70
Subject 5	0.63	0.00014	0.71

Table 2.3. Inter-scanner reproducibility at different field strength. Slope m, intercept q and Pearson's correlation coefficient r that characterize QSM reproducibility in two datasets: one acquired on the 3T scanner the other acquired on the 7T scanner. The fact that the quantitative measures of χ are not reproducible is certified by $m \ll 1$ for all subjects.

The comparison between χ maps obtained from single echoes revealed high dependence on TEs, as shown in Figure 2.3. The four images along the diagonal (panels A, F, K, P) demonstrate, for data acquired from different echoes in the *same* acquisition, the systematic dependence of QSM values on the TE: the values of m in the lower right side with respect to the diagonal are systematically > 1, while in the upper left side m values are < 1. This observation indicates that, in a whole-brain comparison, QSM values tend to be smaller, on average, when they are computed from data obtained using longer TE. Matrices depicting the values of Pearson's coefficients of correlation are shown in Figure 2.4. For data acquired within the same acquisition, panels A, F, K, P indicate that r decreases for increasing differences between the TEs used.

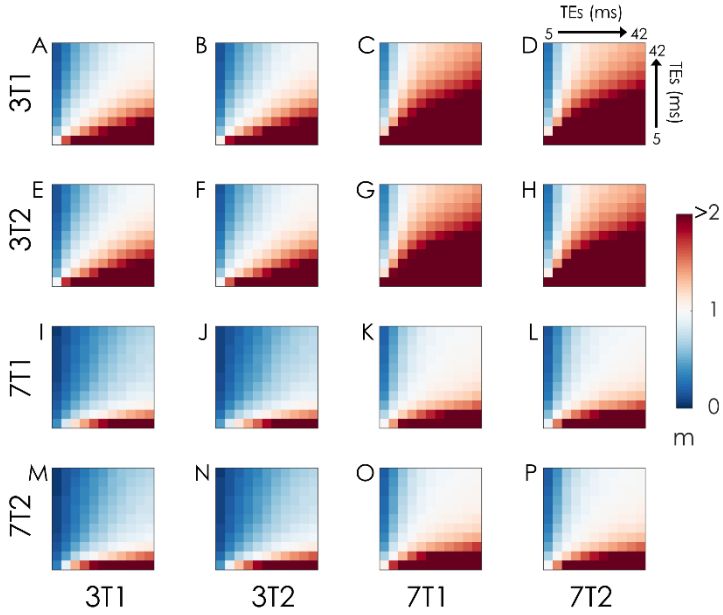

Figure 2.3. Matrices showing the dependence of QSM reproducibility on echo time for one representative subject. Each element of the matrices refers to the comparison between two QSMs obtained with different echoes, from the scans indicated on each axis. The colour indicates the value of the angular coefficient

m obtained by linearly fitting, voxel-wise, QSM measurements at different TEs: $QSM_{TEy} = m \times QSM_{TEx}$, where QSM_{TEy} and QSM_{TEx} indicate the χ maps obtained from the TEs indicated on the vertical and horizontal axes, respectively. Panels on the diagonal (A, F, K, P) show TE-dependence of reproducibility within the same scan; panels B, E and L, O show intra-scanner reproducibility for repeated scans on MRI systems operating at 3T and 7T respectively; panels C, D, G, H, I, J, M, N refer to inter-scanner reproducibility at different field strength.

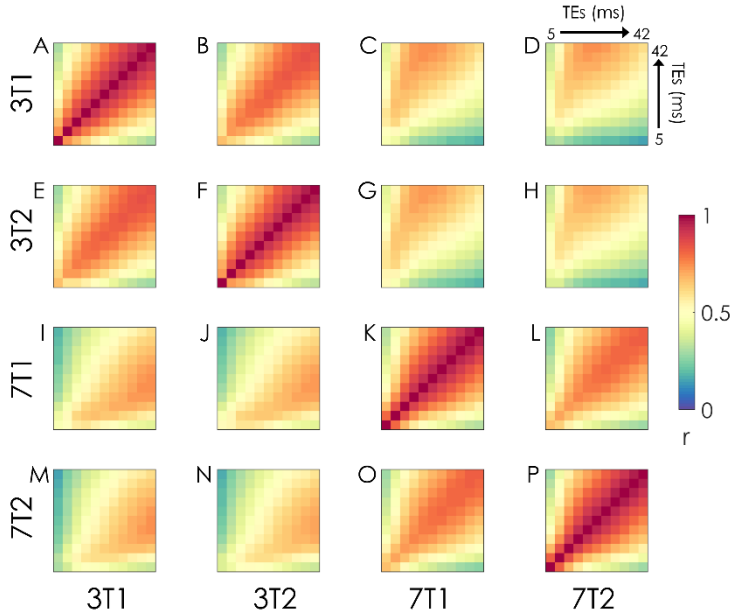

Figure 2.4. Matrices showing the TE-dependence of voxel-wise correlation between χ maps for one representative subject. Each element of the matrices refers to the comparison between two QSMs obtained with different echoes, from the scans indicated on each axis. The color indicates the value of the Pearson's correlation coefficient r obtained by voxel-wise comparison of QSM measurements for different TEs and scan pairs. Panels on the diagonal (A, F, K, P) show TE-dependence of correlation coefficient within the same scan; panels B, E and L, O show intra-scanner comparison for repeated scans on MRI systems operating at 3T and 7T respectively; panels C, D, G, H, I, J, M, N refer to inter-scanner comparison at different field strength.

The relationship between QSM values obtained for individual echoes in *different* acquisitions on the *same* scanner are shown in Figure 2.3, in panels B and E (3T scanner) and L and O (7T scanner). The highest reproducibility (m closest to 1) is observed for pairs of QSMs obtained at identical TE (the diagonal elements in each panel), with average values of m = 1.00 ± 0.01 across subjects and scanners for the 11 echo pairs. The same panels in Figure 2.4 indicate, however, that r has the highest values for longer TE: along the diagonal, r at 3T increases from 0.56 for the shortest echo pair, to 0.79 for the longest TEs, while at 7T r ranges from 0.67 to 0.80.

The remaining eight panels in Figures 2.3 and 2.4 (C, D, G, H, I, J, M, N) describe the reproducibility of QSM in acquisitions on *different* scanners. The combinations of TE that produce m coefficients closest to 1 are not on the panels' diagonals, indicating that best reproducibility is obtained by using longer echoes at 3T than at 7T.

The optimal pairs of TEs that maximize reproducibility in whole-brain scans computed on pooled datasets of all but one subjects are shown in Figure 2.5: for each TE at the field strength indicated on the x-axes, gray dots indicate the optimal TE at the field strength on the y-axes, to maximize QSM reproducibility. The red lines show the results of linear fits: TEs should be matched for intra-scanner measurement while TEs selected at 3T should be approximately 2.6 times the ones at 7T to obtain maximum reproducibility in the whole-brain. For example, Panel C shows that the QSM obtained from first echo at 7T is best matched by the QSM obtained with the third echo at 3T.

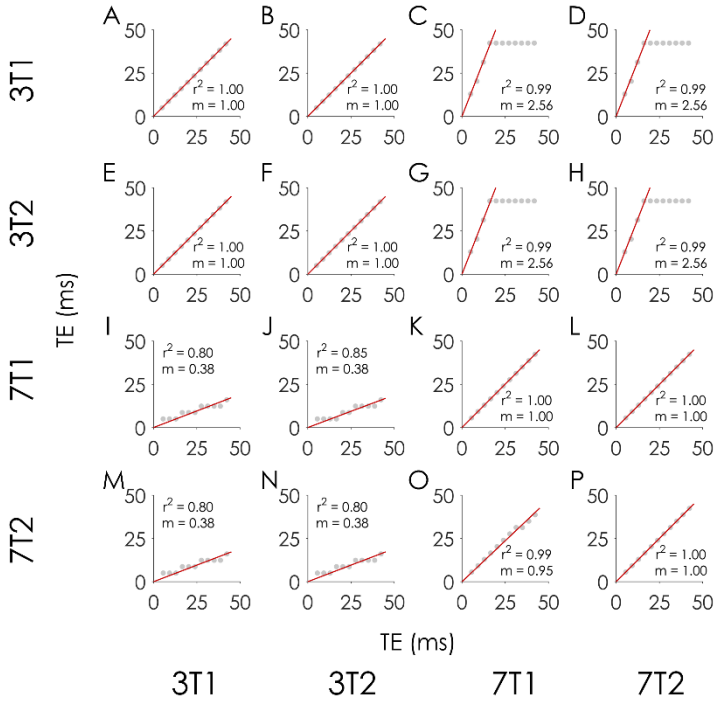

Figure 2.5. Optimal pairs of TEs obtained by pooling datasets from all-but-one subjects. In this case subject S4 was excluded. For each TE at the field strength indicated on the x-axes, gray dots indicate the optimal TE at the field strength on the y-axes, to maximize QSM reproducibility. The red lines show the results of linear fits. In panels C, D, G, H the data points at the plateau are excluded from the fit. TEs must obviously be matched for intra-scanner measurement while TEs selected at 3T should be approximately 2.6 times the ones at 7T to obtain maximum reproducibility in whole-brain scans.

Figure 2.6 shows the results of one application of the LOOCV approach to the corresponding left-out subject. It indicates improved reproducibility that can be obtained between 3T and 7T scans when optimal pairs of echoes are carefully selected: in Panel A, the resultant QSM obtained for one representative subject by averaging the QSMs generated from echoes 1 through 4 in scan 7T1 is compared to the

resultant QSM obtained by averaging the QSMs from echoes 3, 5, 8, 11 in scan 3T1 (that is, the optimal echo pairs that were fitted in Figure 2.5 Panel C). Figure 2.6 Panel B shows the Bland-Altman plot of the comparison considered in Panel A, which indicates the absence of significant biases between the two measures (mean difference between QSMs = 0.0013 ppm), with C.I. = 0.06 ppm. Table 2.4 shows the values that characterize inter-scanner reproducibility in all subjects, when the TEs of 3T and 7T acquisitions are selected as explained above. Compared to those in Table 2.3, the values of m and r in each of all subjects have systematically and significantly improved (paired t-tests; $p < 0.0005$ for m; $p < 0.01$ for r). Across subjects, the average values of m were 0.97 ± 0.044, r = 0.68 ± 0.04, and C.I. = 0.063 ± 0.004 ppm. The bar plot in Figure 2.7 shows the improved values of m and r in inter-scanner (3T vs 7T) QSM reproducibility, when only the appropriate echo times are selected.

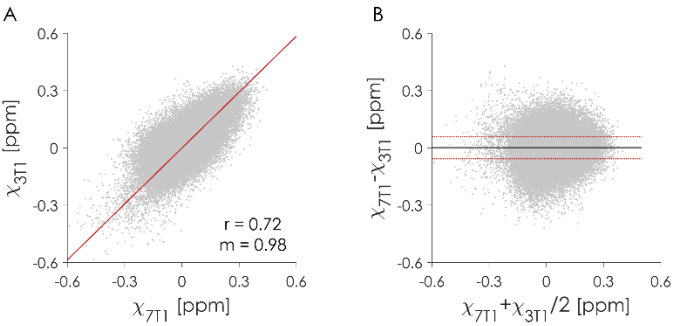

Figure 2.6. Scatter plot (panel A) and Bland-Altman plot (panel B) obtained as a result of the leave-one-out cross-validation for subject S4 by averaging the χ maps computed at the TEs that maximize inter-scanner reproducibility. Excellent reproducibility (m~1) can be achieved by choosing the appropriate combination of TEs. χ_{7T1} is obtained by averaging the QSMs generated from echoes 1 through 4 in scan 7T1; χ_{3T1} is obtained by averaging the QSMs from echoes 3, 5, 8, 11 in scan 3T1 (refer to the optimal echo pairs that were fitted in Figure 2.5 Panel C). Bland-Altman plots show absence of any bias or trend together with good agreement between the two measurements.

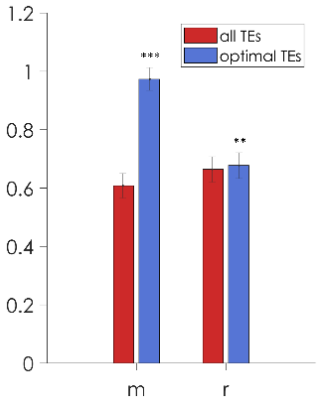

Figure 2.7. Bar plot showing the improvement in inter-scanner (3T vs 7T) QSM reproducibility, when only the appropriate echo times are selected. Each bar indicates the average and standard deviation across subjects of m and r. Red bars refer to QSMs obtained by averaging the χ maps derived from all acquired echoes (as in Figure 2.2 and Table 2.3). Blue bars refer to QSMs obtained by averaging only the χ maps derived from appropriate echoes (as in Figure 2.6 and Table 2.4). Both the improvements in m and r are statistically significant (paired t-tests; *** indicates $p < 0.0005$; ** indicates $p < 0.01$).

	m	**q [ppm]**	**r**	**CI [ppm]**
Subject 1	0.91	-0.0013	0.64	0.063
Subject 2	1.02	-0.0010	0.63	0.069
Subject 3	0.99	-0.0016	0.69	0.064
Subject 4	0.98	-0.0012	0.72	0.058
Subject 5	0.96	-0.0018	0.72	0.060

Table 2.4. Inter-scanner reproducibility at different field strength with optimal TEs. Slope m, intercept q and Pearson's correlation coefficient r that characterize

QSM reproducibility in two datasets (one acquired on the 3T scanner the other acquired on the 7T scanner) when only the susceptibility maps obtained at the optimal echo times are averaged. The values of the angular coefficient m are much closer to 1 than those in Table 2.3.

2.5 Discussion

The assessment of reproducibility of quantitative measurements of χ is essential to apply QSM as a regular technique in clinical MRI protocols of multi-center studies and for longitudinal follow-up. We compared the data of multiple QSM acquisitions obtained on healthy subjects at 3T and, for the first time, at 7T. The assessment was conducted by using acquisition protocols with harmonized scanning parameters, similar to those typically reported in the literature and used for clinical applications, and a standardized and well-established post-processing pipeline.

The main sources of magnetic susceptibility in healthy subjects are myelin in white matter fibers, iron in cortical and subcortical structures and hemoglobin in veins. The transient changes in blood susceptibility, which can be measured via QSM by using EPI acquisition [95,110,111,113,114,140], cannot be appreciated with the standard QSM protocol used in this study. Therefore, it is reasonable to assume that the sources of susceptibility remained unaltered in each subject between the first and last QSM acquisition (all exams were performed within one month). Our data and analyses directly demonstrate that quantitative measures of χ vary with TE. This aspect is attributed to the nature of the phase signal, which does not evolve linearly with TE due to mechanisms involving tissue microstructure and intra-voxel compartmentalization [91,92,96,97,118,141] and may not be observable in studies that investigated QSM reproducibility by using phantoms [135].

The TE-dependency of QSM does not impact the reproducibility of quantitative χ measures in studies where only one MR system (or only one static magnetic field) is used, provided that scanning parameters, including coverage [89,90], imaging resolution [90,93] and of course TEs

[91,92], are matched, and provided also that the subject's head is positioned approximately in the same orientation to avoid issues arising from the anisotropic behavior of susceptibility [76–78]. When multi-echo acquisitions are used, averaging the QSMs obtained from all individual echoes [139] produces coefficients of correlation between measures that are higher than those between single-echo QSMs, possibly as a consequence of improved Signal-to-Noise Ratio (SNR).

The main result of our study is that excellent QSM reproducibility can be achieved, even across systems operating at different field strengths, provided that acquisition parameters are properly selected. By scanning the same group of healthy subjects on 3T and 7T scanners, with same spatial resolution and whole-brain coverage, we demonstrated that optimal reproducibility is obtained when TEs at 3T are ~2.6 times longer than those at 7T. It is worth pointing out that, since the number of TEs used in this study is finite and TEs are systematically the same with the same echo-spacing in all scans, the ratios between them can assume only a limited number of possible values. The factor of 2.6 found in this study may slightly change in protocols with different TEs. Moreover, this factor has been computed with the aim to maximize QSM reproducibility in the whole brain: the computation of the optimal ratio between TEs in studies targeting only specific anatomical regions at different field strengths might require further investigation. To this purpose, it is possible and desirable to select appropriate echo times by using a small group of travelling-heads, especially when performing multi-center studies with scanners operating at different field strength.

Our data show that r steadily increases when long TEs are used, as maps obtained by using shorter TEs suffer from lower phase contrast and reduced dynamic range. It should not be straightforwardly inferred, though, that the use of even longer TEs would improve reproducibility. Phase data have maximal SNR when the TE is equal to the T2* of the tissue of interest [142]; data with longer TE might be considerably noisier and especially tissues with short T2* relaxation could be affected. Similarly, studies focusing on specific regions instead of the whole brain may benefit from the use of reproducible QSM protocols specifically

designed to take into account TE dependencies and SNR issues in the targeted tissues.

In the 7T vs 3T comparison, Pearson's r values using the optimally chosen pairs of TEs are significantly higher than those in the non-calibrated case (Figure 2.7). However, they still remain lower than the intra-scanner correlation coefficients, in accordance with what was also reported in other studies at lower field strengths [130]. The limited increase in correlation coefficient can be explained by a series of possibly concomitant reasons. First, the correlation coefficients in Figure 2.2 are measured by averaging all echoes: the SNR of the susceptibility maps obtained this way is higher than in QSM obtained by using only a few echoes. Second, the TEs that maximize the reproducibility include the shortest TEs of the 7T acquisition which, as shown in Figure 2.4, are associated to smaller correlation values. Third, the relative phase contribution of intra-voxel compartments may differ between 3T and 7T, even when optimal pairs of TEs are chosen. This aspect might limit the improvement in Pearson's correlation that can be achieved in the comparison between QSMs obtained at different magnetic fields. While the proposed procedure of echo selection and averaging favors overall unbiased and reproducible QSM measures at different magnetic fields across the whole brain, the presence of voxels with different QSM values at different field strengths, attributable to intra-voxel compartmentalization, remains an open issue. Last, lower inter-scanner correlation coefficients may be a consequence of different B_0 inhomogeneities and head positioning related to the different head coil conformation: each subject is more likely to have the head in positions that are more similar when lying inside the same head coil and scanner.

Any step in the QSM processing pipeline may introduce errors. For example, it is worth mentioning that, in the presence of strong susceptibility sources, phase unwrapping may fail [92]. Moreover, in the background field removal step, VSHARP may not be reliable close to the boundaries of the brain mask, as the small kernel used in these regions to minimize erosion may lead to the amplification of the phase error [143]. However, since the phase-processing pipeline is equally applied

to all datasets in this study, and it affects only a small number of voxels, this aspect should have only a marginal impact on the presented results. Different QSM algorithms produce different χ maps [144]. However, a recent study [92] obtained similar results with iLSQR [12,13] and other methods, namely streaking artifact reduction for QSM (STAR-QSM) [14] and thresholded k-space division with modified dipole kernel inversion [10,145], and concluded that TE-dependencies occur consistently, irrespectively of the QSM algorithm used.

In conclusion, our study demonstrated high consistency of susceptibility measures across repeated acquisition at 3T, as reported by previous works [84,130–134], and for the first time it assessed QSM stability in-vivo at 7T. Albeit care should be taken when comparing susceptibility maps acquired at different field strength due to the uncertain and relative contribution of voxel compartments to the signal, QSM can be considered as a suitable technique for longitudinal follow-up in clinical settings and in multi-center studies, provided that acquisition parameters, including TE, are suitably set.

Chapter 3 Diagnostic accuracy of Quantitative Susceptibility Mapping in Multiple System Atrophy: the impact of echo time and the potential of histogram analysis

The work presented in this chapter was performed thanks to the collaboration of the Neuroradiology Unit of the University Hospital of Pisa (Pisa, Italy), the Department of Biomedical and NeuroMotor Sciences of the University of Bologna and the IRCCS Institute for Neurological Sciences of Bologna (Bologna, Italy), the Parkinson and Movement Disorder Unit of the IRCCS Mondino Foundation (Pavia, Italy) and the IMAGO7 Research Center (Pisa, Italy).

It was presented at the 29th Annual Meeting of ISMRM in 2021, and the manuscript is currently in preparation for submission to a peer-reviewed journal:

Lancione M, Cencini M, Costagli M, Donatelli G, Giannini G, Tosetti M, Calandra-Buonaura G, Zangaglia R, Pacchetti C, Cortelli P, Cosottini M, *Diagnostic accuracy of Quantitative Susceptibility Mapping in Multiple System Atrophy: the impact of echo time and the potential of histogram analysis.*

3.1 Abstract

The non-invasive quantification of iron stores via Quantitative Susceptibility Mapping (QSM) can play an important role in the diagnosis and the differential diagnosis of atypical Parkinsonisms. However, the susceptibility (χ) values measured via QSM depend on echo time (TE). This effect relates to the microstructural organization within the voxel, whose composition can be altered by the disease. Moreover, pathological iron deposition in a brain area may not be

spatially uniform, and conventional Region of Interest (ROI)-based analysis may fail in detecting alterations. Therefore, in this work we evaluated the impact of echo time on the diagnostic accuracy of QSM on a population of patients with Multiple System Atrophy (MSA) of either Parkinsonian (MSAp) or cerebellar (MSAc) phenotypes. In addition, we tested the potential of histogram analysis to improve QSM classification accuracy.

We enrolled 32 patients (19 MSAp and 13 MSAc) and 16 healthy controls, who underwent a 7T MRI session including a gradient-recalled multi-echo sequence for susceptibility (χ) mapping. Nine histogram features were extracted from the χ maps computed for each TE in atlas-based ROI covering deep brain nuclei, and compared among groups.

Alterations of susceptibility distribution were found in Putamen, Substantia Nigra, Globus Pallidus and Caudate Nucleus for MSAp and in Substantia Nigra and Dentate Nucleus for MSAc. Increased iron deposition was observed in a larger number of ROIs for the two shortest TEs and the standard deviation and the 90th percentile were the most informative features yielding excellent diagnostic accuracy with area under the ROC curve > 0.9.

In conclusion, short TEs may enhance QSM diagnostic performances, as they can capture variations in rapidly-decaying contributions of high χ sources. The analysis of histogram features allowed to reveal fine heterogeneities in the spatial distribution of susceptibility alteration, otherwise undetected by a simple evaluation of ROI χ mean values.

3.2 Introduction

Multiple System Atrophy (MSA) is a rare neurodegenerative disorder characterized by a combination of autonomic dysfunctions (cardiovascular autonomic failure and urogenital dysfunctions) plus cerebellar syndrome and/or Parkinsonism. The current diagnostic criteria define three degrees of certainty for diagnosis (possible, probable and definite) and two phenotypes, Parkinsonian (MSAp) or cerebellar (MSAc), according to the predominant features at the time of evaluation

[146]. Even though it is still a matter of debate whether iron accumulation is a cause or a consequence of the neurodegenerative process [147], increased iron deposition has been documented in many deep grey matter nuclei of MSA patients. Histopathological studies, indeed, reported iron deposition in the posterolateral putamen [148], in substantia nigra pars compacta, globus pallidus [149], caudate nucleus [150] and dentate nucleus [151].

Iron store represents an important biomarker for the diagnosis and the differential diagnosis of neurodegenerative diseases and Quantitative Susceptibility Mapping (QSM) is a powerful tool for its non-invasive and quantitative assessment in vivo via Magnetic Resonance Imaging (MRI) [10,94,117–121]. QSM derives the magnetic susceptibility of the tissues, which correlates with iron concentration [25], from the phase of a T2*-weighted Gradient Recalled Echo (GRE) signal. The provided information is quantitative and spatially specific, as the non-local distortions induced by susceptibility sources on the magnitude of T2*-weighted signals are removed. For these reasons, QSM is gaining increasing importance in the study of neurodegenerative disorders [36], including Parkinson's disease [43,45,49,152] and atypical Parkinsonisms [153,154]. Concerning MSA, previous studies reported altered susceptibility in putamina, substantia nigra, red nuclei, subthalamic nuclei and, for MSAc, in dentate nuclei [46,47,51,155], yielding good diagnostic accuracy in discriminating MSA patients to both healthy controls and other Parkinsonisms.

Recent works reported that measured susceptibility values depend on several experimental factors. First of all, susceptibility anisotropy impairs QSM accuracy in white matter, where the highly organized microstructure of myelin sheath introduces a dependence of measured susceptibility on the orientation of fibers with respect to the external magnetic field [28,77,78,156]. In addition, the dependence of QSM on acquisition parameters such as coverage [89,90], spatial resolution [90,93] and Echo Time (TE) [91,92,116,157] was demonstrated. The dependence on TE is due to the non-linear time-evolution of the phase signal, possibly reflecting the presence of multiple signal components

caused by sub-voxel compartmentalization and microstructures [91,96–98]. A previous study at 3T reported that it can yield variations of QSM values in intact tissues up to approximately 100 parts per billion (ppb) and beyond 1000 ppb for cerebral microbleeds [92]. On these premises, as pathological processes can affect sub-voxel composition, we hypothesize that χ maps computed at different TEs may provide different and complementary diagnostic information.

The vast majority of QSM studies targeting the deep gray matter nuclei are based on the measurement of mean susceptibility in manually-drawn or automatically-selected regions of interest (ROI). However, the iron deposition in nuclei affected by the disease might not be uniform, as also reported by histological studies (e.g., in MSA the putamen is mainly involved in its posterolateral portion [148]). In these cases, the mean value would provide a partial and inaccurate estimate of iron distribution. Histogram analysis performed on the whole nucleus may provide a more comprehensive overview of the susceptibility distribution and the underlying iron deposition pattern, reflecting its spatial heterogeneity [158].

The goal of the present study was twofold. First, we aimed to assess the impact of TE-dependency of QSM on the accuracy of differential diagnosis in a cohort of MSA patients of both Parkinsonian and cerebellar variants and a population of healthy controls. Second, we explored the potential of histogram analysis in enhancing the diagnostic performance of QSM. To these purposes, we enrolled a cohort of patients with MSA and a population of healthy controls and acquired multi-echo GRE data on a 7T MRI system. We reconstructed a susceptibility map for each TE separately and performed histogram analysis on a set of ROIs selected from published atlases covering ten deep gray matter nuclei.

3.3 Methods

3.3.1 Study group

We enrolled patients with a diagnosis of possible or probable MSA referring to the Movement Disorders and Autonomic Disorders centers of the University of Bologna, Italy, and to the Parkinson and Movement Disorder Unit of IRCCS Mondino Foundation in Pavia, Italy during 2019-2020. Diagnosis of MSA was independently confirmed by three movement disorder specialized neurologists (PC, GCB, CP) according to current consensus criteria [146]. The MSA phenotype was defined as MSAp or MSAc on the basis of the predominant motor involvement at the time of the last clinical evaluation. The absence of non-supporting features for MSA were mandatory for inclusion in the study. Disease duration was defined as the time interval between the onset of the first MSA-related symptom and enrollment in this study.

We recruited 32 patients with MSA: 19 MSAp (11 females, 65±8 [51-76] years old, 4 possible and 15 probable MSAp, disease duration = 5.3 ± 2.2 [3-9]) and 13 MSAc patients (5 females, 60±7 [48-72] years old, all probable MSAc, disease duration = 6.0 ± 3.0 [3-13]). In addition, a population of 16 healthy controls (HC) and comparable age and sex distribution (6 females, 60±10 [43-76] years old) was enrolled. The study was performed in accordance with the Declaration of Helsinki and approved by the Independent Ethics Committee of the local health service of Bologna (CE number: 18056, 212/2018/OSS/AUSLBO) and of Pavia (CE number: p-20180049076); all participants gave their written informed consent.

3.3.2 MRI acquisition hardware

All subjects underwent an ultra-high field MRI examination at the IMAGO7 Foundation in Pisa, Italy, using a GE Healthcare Discovery MR950 7-T MRI system (GE Healthcare, Milwaukee, WI, USA). The patients were scanned within one month from the clinical evaluation.

The scanner was equipped with a two-channel transmitter/32-channel receiver head coil (Nova Medical, Wilmington, MA, USA) and a gradient system with maximum amplitude = 50 mT/m and slew rate = 200 T/m/s.

3.3.3 MRI imaging protocol

The MRI protocol included a 3D Gradient Recalled Multi-Echo sequence (Susceptibility Weighted Angiography – SWAN, GE Healthcare) for the quantitative assessment of iron deposition. The sequence was prescribed axially with whole-brain coverage. The acquisition parameters were set as follows: TR = 54.1ms; four equally spaced echoes: TE = 7.38, 16.36, 25.34, 34.32 ms; FA = 15°; voxel size = 0.6 × 0.6 × 1.2 mm^3; in-plane FOV = 173 × 173 mm^2; axial coverage = 165.6 mm; parallel imaging ASSET (Array Coil Spatial Sensitivity Encoding) acceleration factor = 2. Both the real and imaginary parts of the images obtained at each echo were saved and converted into magnitude and phase data.

3.3.4 Data processing

Susceptibility maps were computed via the following procedure. The raw phase images of individual echoes were unwrapped using a Laplacian-based algorithm [3,12]. A brain mask was generated using Brain Extraction Toolbox (bet) [137] in FSL 5.0.9 (FMRIB Software Library, Oxford Centre for Functional MRI of the Brain, Oxford, UK) on the T2*-weighted image averaged across echoes and then used for the removal of the background field via V-SHARP [8]. QSM images were obtained by applying the iLSQR [12,13] method separately to each individual echo. We used Laplacian-based phase unwrapping, V-SHARP and iLSQR implementations from STI Suite (MATLAB code from UC Berkeley, Berkley, CA, USA) [138].

A study-specific template was also created using skull-stripped T2*-weighted images averaged across TEs of all subjects with Greedy-SyN approach and cross-correlation similarity metric [159] setting the parameters of antsMultivariateTemplateConstruction2 as follows: six template-construction iterations, 0.1 gradient step size, maximum

1000×500×250×100 multi-resolution iterations per registration, shrink factors 12×8×4×2, smoothing factors 4×3×2×1. The susceptibility maps of each echo were warped to the template space by applying the corresponding transformation. Then, they were averaged to create a study-specific QSM template.

3.3.5 Qualitative data inspection

The T2*-weighted images obtained from the magnitude of the 3D GRE signal were evaluated by a neuroradiologist and graded based on the severity of motion artifacts into three categories: "none/mild" corresponding to non-visible or little motion artifact, "moderate" for detectable motion and "severe" for extreme motion artifacts. Images affected by "severe" motion artifacts were excluded from the analysis.

3.3.6 QSM ROI-based analysis

Regions of interest were selected from the PD25 atlas [160], from the probabilistic CIT168 atlas [161] and from the probabilistic DN atlas [162]. The selected ROIs were the following, each divided into left (L) and right (R) regions: Red Nucleus (RN), Subthalamic Nucleus (STN), Caudate Nucleus (CN), Putamen (Pu), Globus Pallidus externus (GPe) and internus (GPi), Thalamus (Th) from the PD25 atlas, Substantia Nigra pars compacta (SNc) and reticulata (SNr) from probabilistic CIT168 atlas, and Dentate Nucleus (DN) from DN atlas. Probabilistic ROIs were converted to binary masks by choosing a threshold of 0.5. The T2*-weighted template was non-linearly warped to the T2*-weighted version of the multi-contrast PD25 atlas via antsRegistration using cross-correlation similarity metric and nearest neighbor interpolation. By applying the inverse transformation, the ROIs from the PD25 atlas were warped to the study-specific template. To improve registration accuracy, the CIT168 atlas and DN atlas were warped from the MNI to the T1-weighted version of PD25 atlas and then to the study-specific template, after concatenating the two transforms in order to perform them in a single step.

For each ROI and for each subject in the study-specific template space we extracted the following histogram features for each TE: mean value, standard deviation, $10^{th}/25^{th}/50^{th}/75^{th}/90^{th}$ percentile, kurtosis and skewness. The histogram features were computed using the corresponding built-in function in MATLAB which employed the whole sample, making the calculation independent of histogram binning operations. The measured values of susceptibility were expressed in parts per million (ppm). QSM values were not referenced to any specific region [85] to avoid assumptions on brain areas spared by MSA.

3.3.7 Statistical analysis

Statistical analysis was performed in MATLAB (MathWorks, Natick, MA, USA). Sex and age distributions of the three populations (MSAc, MSAp and HC) were compared pair-wise via chi-square test and independent t-test respectively. The threshold of statistical significance was set to $p < 0.05$. Non-parametric statistical tests were employed to analyze QSM data: the feature values among the three groups were compared with Kruskal-Wallis omnibus test, followed by Dunn's test and Dunn-Sidak correction for post-hoc analysis. Diagnostic accuracy was evaluated via the Area Under the Curve (AUC) of the Receiver Operating Characteristic (ROC) curve.

3.4 Results

After visual inspection and rating of the T2*-weighted images by a neuroradiologist, four subjects (1 MSAp, 3 MSAc) were excluded from QSM analysis due to severe motion artifacts. The remaining population of patients was demographically distributed as follows: 18 MSAp (10 females, 65±8 [51-76] years old, disease duration = 5.4 ± 2.1 [3-9], 4 possible and 14 probable MSAp) and 10 MSAc patients (4 females, 60±7 [52-72] years old, disease duration = 5.8 ± 3.1 [3-13], all probable MSAc).

No statistically significant differences between the distribution of the demographic features of sex and age were reported between healthy controls and MSAc and MSAp patients.

Nine histogram features (mean, standard deviation, $10^{th}/25^{th}/50^{th}/75^{th}/90^{th}$ percentile, kurtosis and skewness) were computed for each subject, TE and ROI. These covered ten nuclei divided into left and right sides which are displayed in Figure 3.1 overlaid onto the study-specific template.

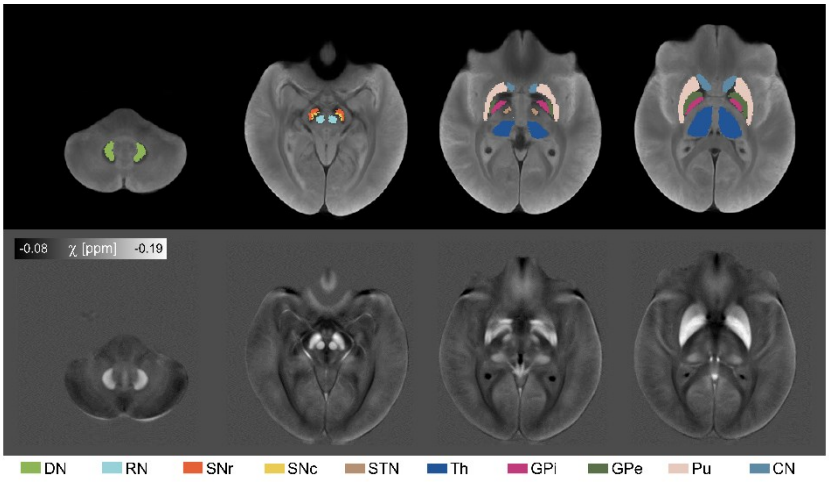

Figure 3.1: ROIs used in the QSM analysis overlaid onto the study-specific template (top row), which was computed from the across-TEs average of the T2*-weighted image of each subject. In the bottom row the corresponding susceptibility maps computed from the first TE averaged over all the subjects in the template space is displayed.

We compared the distribution of the histogram features between the MSAc and MSAp patients and healthy controls for each ROI and each TE. The obtained p-values are reported in Figure 3.2. Statistical significance was reached for several ROIs and features, e.g., for the mean, the 75^{th} percentile, and above all for the standard deviation and

the 90th percentile computed at the first (TE01) and the second TE (TE02), respectively, for which up to fourteen ROIs reported significant difference among groups. These findings indicate a distributed pattern of pathological iron deposition. The tests performed at shortest TEs (i.e., TE01 and TE02) yielded higher levels of statistical significance, detecting group differences that were not observed with longer TEs.

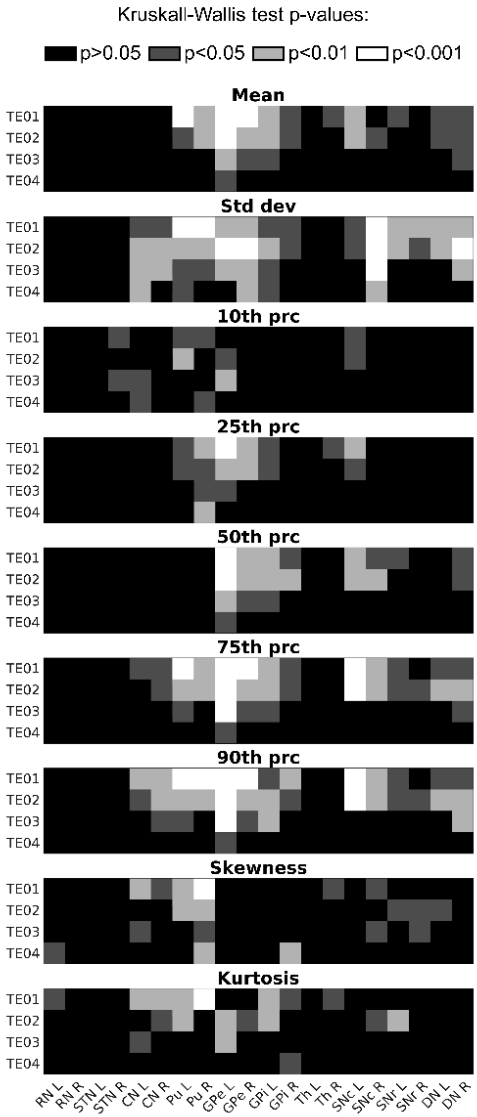

Figure 3.2: Results of group comparison of QSM histogram features. The gray-level in each plot indicates the p-values obtained by comparing a specific

histogram feature of QSM data among the three groups (HC, MSAc and MSAp) via Kruskal-Wallis test for each TE (indicated as TE01, TE02, TE03 and TE04) and each ROI. Overall, the features reaching the highest statistical significance in group discrimination are the mean, the standard deviation, the 75th and the 90th percentile. Smaller p-values are obtained with short TEs which enable to detect statistically significant differences even in ROIs that do not exhibit differences when long TEs are used.

In Figure 3.3, we reported the mean susceptibility values computed at TE01 in all the ROIs for all subjects, divided into the three groups. In the post-hoc analysis, MSAp patients showed higher susceptibility in Pu and GPe bilaterally with respect to MSAc and HC, and higher susceptibility in GPi bilaterally with respect to HC. Increased iron deposition was also reported in left SNc for both phenotypes with respect to HC and higher susceptibility was observed in DN bilaterally for MSAc with respect to MSAp. The 90th percentile and the standard deviation detected significant susceptibility differences between groups also in other ROIs, such as CN, SNr and right SNc (Supplementary Figures S3.1 and S3.2). However, when the same features were extracted from susceptibility maps computed at longer TEs, the χ difference between groups was reduced and did not reach statistical significance. Figure 3.4 displays the dependence on TE of an exemplary feature, i.e., mean susceptibility, in each ROI for the three groups. While short echo times, such as TE01 and TE02, allowed group discrimination, at longer TEs the measured values for each population were similar: at TE01 and TE02, we reported statistically significant group differences in 11 and 10 ROIs respectively, but only in 4 ROIs at TE03 and 1 at TE04. This finding indicates that the TE-dependence of the histogram features differs for the three populations.

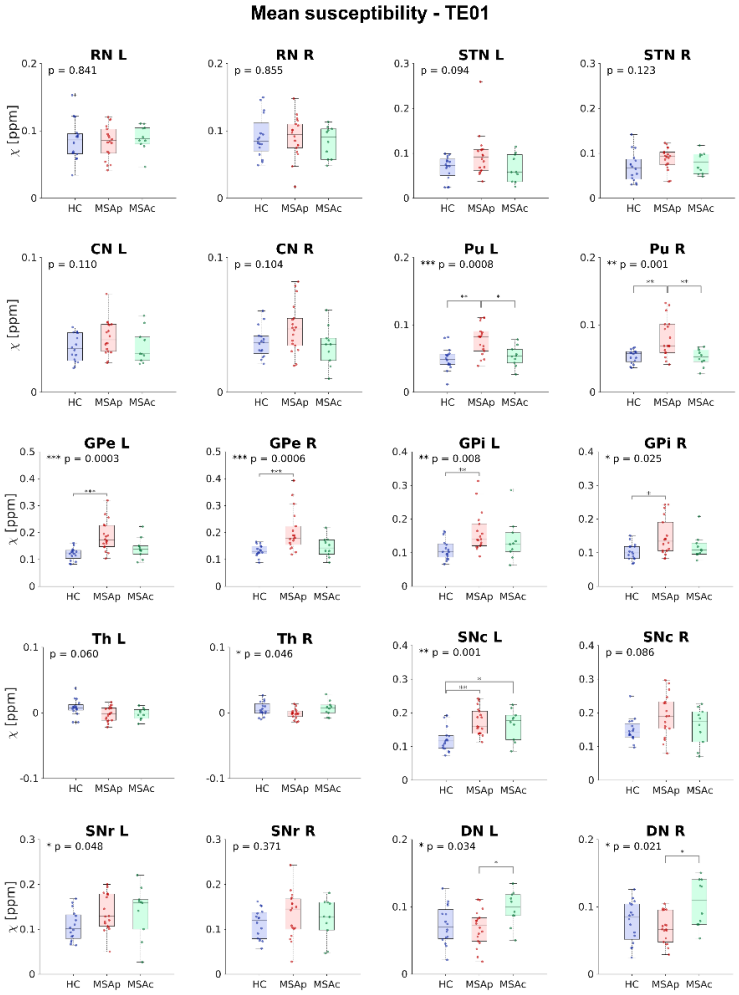

Figure 3.3: Box plots showing the mean QSM values in each ROI for all subjects (HC in blue, MSAp in red and MSAc in green) extracted from maps computed from the first TE, which shows the highest number of significant alterations. In the top-left corner of each plot the p-value from the Kruskal-Wallis test is reported. Post-hoc Dunn's tests reaching significance after Dunn-Sidak correction for multiple comparison are indicated by the asterisks (* $p < 0.05$, ** $p < 0.01$, *** $p < 0.001$).

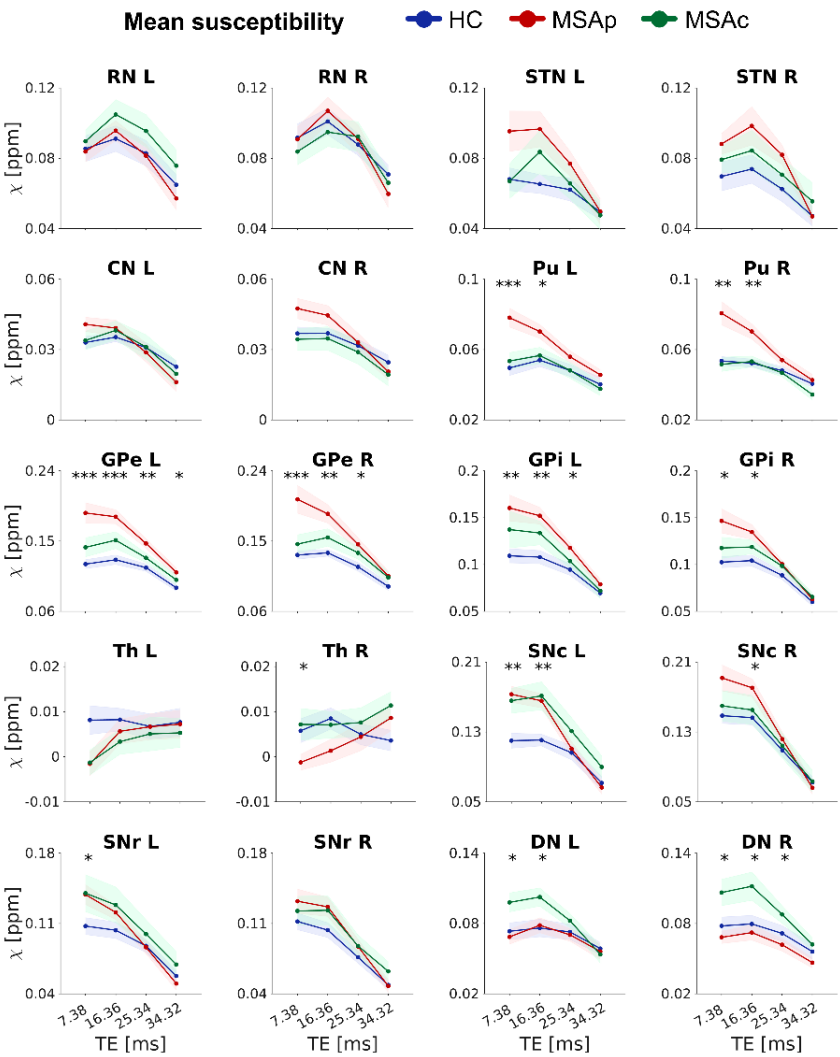

Figure 3.4: Dependence on TE of the group differences in mean susceptibility. Each plot displays the mean susceptibility in one ROI for the three groups: HC (blue line), MSAp (red line) and MSAc (green line). The shaded area represents the standard error of the mean, and the asterisks indicate the TEs at which the difference in mean susceptibility across groups reaches significance in the

Kruskal-Wallis omnibus test (* $p < 0.05$, ** $p < 0.01$, *** $p < 0.001$). At longer TEs the measured values for each population tends to converge, preventing groups discrimination.

The diagnostic accuracy provided by each histogram feature at each TE was evaluated via ROC analysis. In Figure 3.5, the AUC is reported as a measurement of diagnostic accuracy. Generally, the AUC tended to be higher for short TEs (i.e., TE01 and TE02), for which excellent diagnostic accuracy (up to 0.92) was achieved. The mean, the standard deviation and the 90th percentile yielded the highest accuracy overall. In the discrimination of MSAp and HC, the 75th percentile of the susceptibility distribution in left GPe at TE02 showed the highest AUC of 0.917, with a specificity of 0.938 and a sensitivity of 0.889. When considering MSAc and HC, the highest AUC of 0.919 was found for the standard deviation of TE02 in right DN with a specificity of 0.938 and a sensitivity of 0.800. In the classification of the two phenotypes of MSA, the standard deviation of TE02 in right DN yielded the highest AUC of 0.922 with a specificity of 0.944 and a sensitivity of 0.800. Instead, the simple mean-based analysis yielded lower AUC values: specifically, in discriminating MSAp from HC, MSAc from HC, and MSAp from MSAc, the highest AUC were 0.906 (left GPe at TE02), 0.775 (left SNc at TE01) and 0.828 (right Pu at TE01), respectively. The ROC curves computed for these features are shown in Figure 3.5.

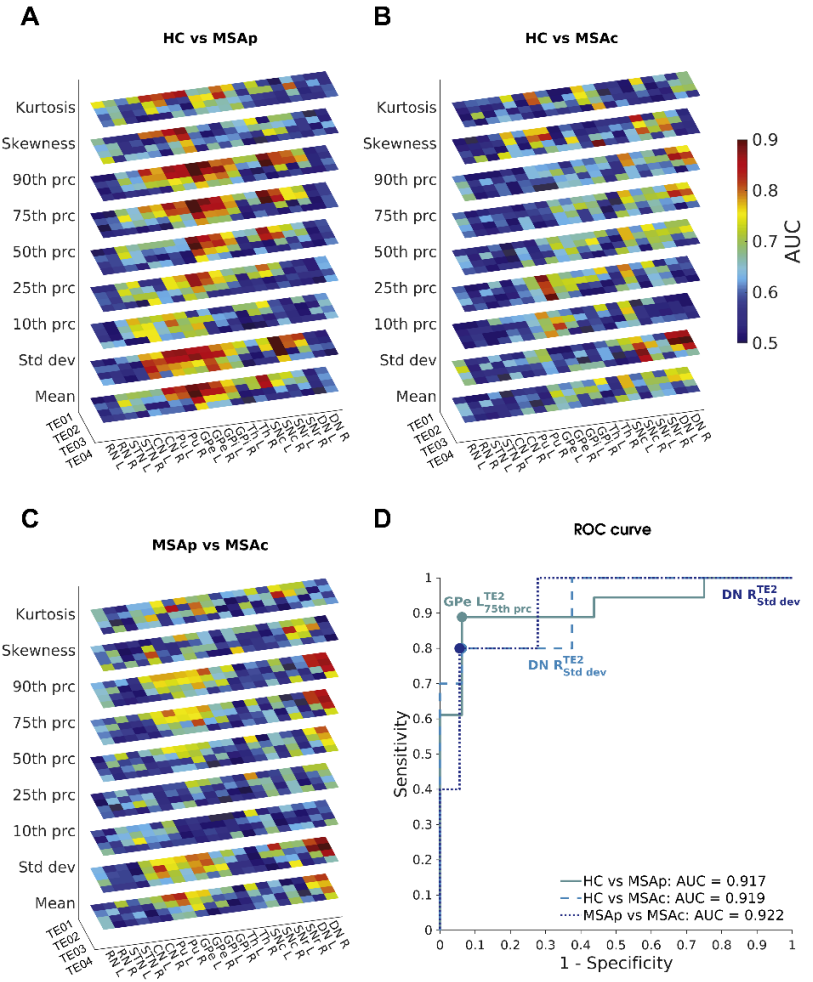

Figure 3.5: Diagnostic accuracy for each group pair (HC vs MSAp, HC vs MSAc and MSAp vs MSAc) is displayed in panels A-C. Colors represent the values of the area under the ROC curve (AUC) for each TE, for each ROI and for each histogram feature. It can be noticed that AUC values are higher for short TEs. In panel D, we reported the ROC curve computed for the combinations of TE, ROI and histogram feature yielding the highest AUC for each comparison between groups. The dots represent the optimal cut-off values of each curve.

3.5 Discussion

In this study we computed susceptibility maps on a population of patients with MSA of both cerebellar and Parkinsonian phenotypes and a population of healthy controls in order to investigate the diagnostic value of QSM. Specifically, we performed an ROI-based analysis targeting deep gray matter structures and explored the effect of TE on classification accuracy and the diagnostic potential of a set of histogram features.

We found alterations of the susceptibility distribution in several regions for both phenotypes, including Pu, SN, GP and CN for MSAp and SN and DN for MSAc, highlighting a distributed pattern of iron load alteration. These findings are in agreement with histopathological reports [148,149,151] and previous neuroimaging studies which reported higher susceptibility in Pu and SN for MSAp patients [46] and in SN and DN for MSAc patients [155] compared to healthy controls. Interestingly, we observed significantly increased iron deposition in MSA patients in a higher number of ROIs at short echo times, i.e., the first two TEs. These ROIs also included nuclei not previously reported in other QSM studies, such as GP and CN, but in agreement with post-mortem findings [149,150].

The dependence of the diagnostic accuracy of QSM on TE is attributable to the non-linear time-evolution of the phase signal. Previous studies observed this phenomenon in several brain tissues, involving both white and gray matter structures, and both cortical and subcortical regions [91,92], due to a mechanism involving tissue microstructure and intra-voxel compartmentalization [91,96–98]. Even though QSM provides reproducible measurements of tissue susceptibility for matching TEs at the same field strength [116,163,164] when scanning parameters such as coverage [89,90] and spatial resolution [90,93] are fixed and the subject's head is accurately positioned along the same orientation [76–78], the choice of these experimental factors can affect differently the susceptibility values measured in distinct populations. In fact, the rapidly-decaying contribution of strong susceptibility sources, which can be present to a different extent in patients and controls, vanished for

long TEs, preventing the detection of differences between the groups. Hence, when designing a clinical protocol involving single-echo QSM, TE must be chosen carefully, depending on the target ROI. On the other hand, each TE of multi-echo QSM sequences may be reconstructed and analyzed independently in order to get an insight into the tissue microstructures.

In addition to the mean susceptibility, other histogram features yielded excellent diagnostic accuracy in discriminating patients from controls and between phenotypes, with values of AUC above 0.9. In particular, the standard deviation and the 90th percentile were the most informative features. This may reflect the non-uniform alteration of the spatial distribution of iron deposition in some regions. For example, in patients with MSAp the putamina showed increased susceptibility in their posterolateral portion rather than the anterior part [47]. This effect may be detected more easily by analyzing histogram features relating to the tails of the distribution, rather than the mean, in agreement with a previous study that reported the highest diagnostic accuracy in differentiating patients with Parkinson's disease from healthy controls for the 10th/75th/90th percentiles and the skewness of the distribution [158]. Also, in ROIs presenting inner subdivisions that are difficult to identify especially in patients, such as the trilaminar structure of substantia nigra in Parkinson's disease, histogram analysis performed on the whole-volume of the ROI may help in separating the contributions of different structures [165,166]. Future studies should focus on the potential of radiomics second-order textures [166–168] and on the application of advanced multivariate methods based on multivoxel pattern analysis. These approaches may reveal fine-grained textures of iron loads and enhance the classification power of QSM in the early differential diagnosis of neurodegenerative disorders.

The relatively small population included in the current study, due to the low prevalence of MSA, may represent a limitation. However, the high level of statistical significance of the results here reported supports the reliability of findings. A larger cohort of subjects would enable the analysis of subgroups of patients based on the presence or the absence

of additional clinical manifestations of interest, as well as the application of machine learning algorithms for feature selection and cross-validation that could improve the diagnostic accuracy by combining the information coming from different features and ROIs [167,168]. One possible limitation is related to the risk of misdiagnosis, as patients were clinically evaluated without post-mortem pathological confirmation. However, the diagnosis was clinically confirmed in the follow-up evaluations for all patients. The ROIs employed in this study were selected from published atlases and automatically registered to the study-specific template, in order to avoid subjective biases affecting manual segmentation. Visual inspection by one experienced neuroradiologist excluded the presence of registration errors that could have affected the results of this study. Similarly, the adopted choice of using unreferenced QSM values (which are therefore referred to the average susceptibility in the acquired volume) should not have influenced our results, as the use of reference region provides negligible corrections [85].

In conclusion, we demonstrated that the use of short TEs enhances the diagnostic performance of QSM, improving its capability in detecting altered iron deposition in deep gray matter nuclei. Notably, it allowed the detection of significant susceptibility increase in previously unreported ROIs. Hence, a targeted choice of TE can increase QSM importance in the diagnosis and differential diagnosis of neurodegenerative diseases. Finally, the analysis of histogram features other than the mean may detect subtle differences in the pattern of susceptibility increase, reflecting not just the overall iron accumulation but also heterogeneities in its spatial distribution within a brain region.

Supplementary Figures

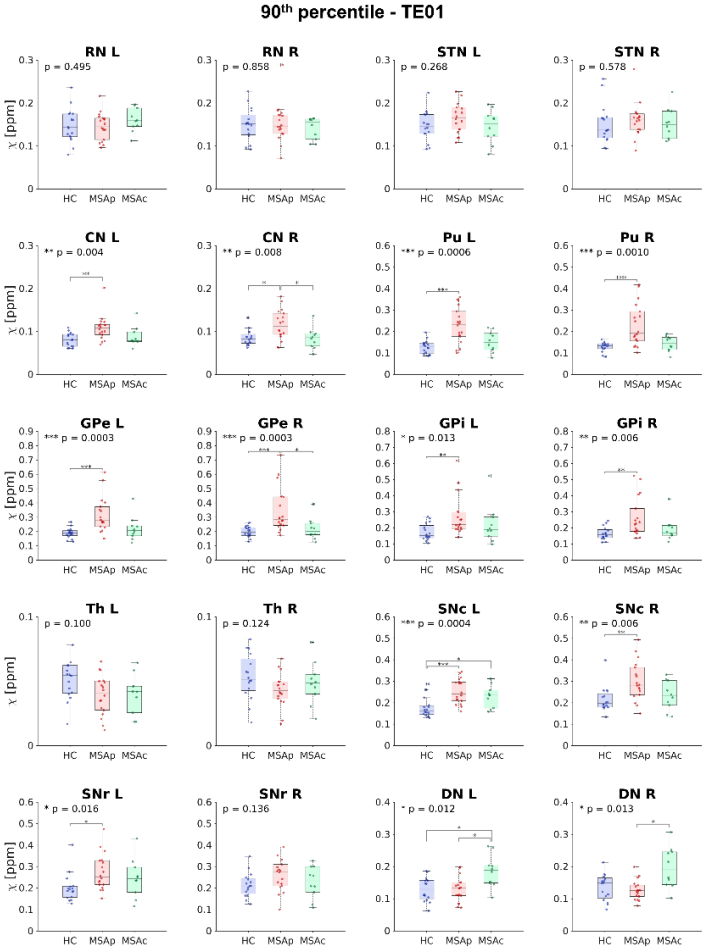

Figure S3.1: Box plots showing the 90th percentile of the distribution of QSM values in each ROI for all subjects (HC in blue, MSAp in red and MSAc in green) extracted from maps computed from the first TE. In the top-left corner of each plot the p-value from the Kruskal-Wallis test is reported. Post-hoc Dunn's tests reaching significance after Dunn-Sidak correction for multiple comparison are indicated by the asterisks (* $p < 0.05$, ** $p < 0.01$, *** $p < 0.001$).

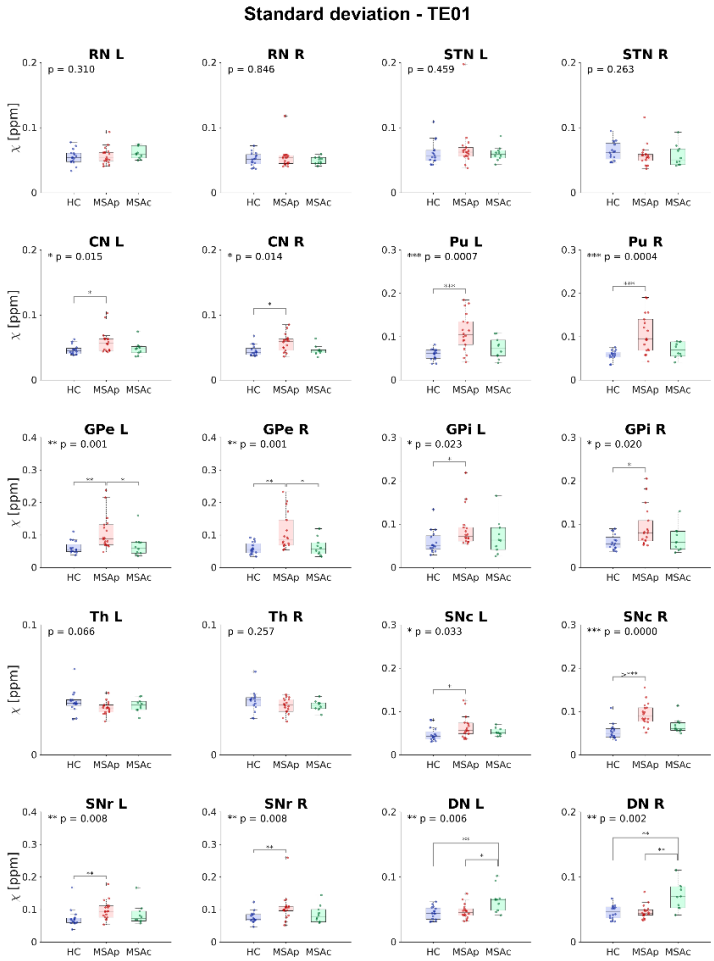

Figure S3.2: Box plots showing the standard deviation of the distribution of QSM values in each ROI for all subjects (HC in blue, MSAp in red and MSAc in green) extracted from maps computed from the first TE. In the top-left corner of each plot the p-value from the Kruskal-Wallis test is reported. Post-hoc Dunn's tests reaching significance after Dunn-Sidak correction for multiple comparison are indicated by the asterisks (* $p < 0.05$, ** $p < 0.01$, *** $p < 0.001$).

Chapter 4 Evaluation of iron overload in Nigrosome 1 via Quantitative Susceptibility Mapping as a presymptomatic biomarker in prodromal stages of Parkinson's disease

The work presented in this chapter was performed thanks to the collaboration of the Neurology and Neuroradiology Units of the University Hospital of Pisa (Pisa, Italy) and the IMAGO7 Research Center (Pisa, Italy).

The manuscript is currently in preparation for submission to a peer-reviewed journal:

Lancione M, Donatelli G, Del Prete E, Campese N, Frosini D, Cencini M, Costagli M, Lucchi G, Tosetti M, Godani M, Arnaldi D, Terzaghi M, Pacchetti C, Cortelli P, Bonanni E, Ceravolo R, Cosottini M, *Evaluation of iron overload in Nigrosome 1 via Quantitative Susceptibility Mapping as a presymptomatic biomarker in prodromal stages of Parkinson's disease*.

4.1 Abstract

Idiopathic rapid eye movement (REM) behavioral disorder (iRBD) is a prodromal stage of α-synucleinopathies, such as Parkinson's disease (PD), which are characterized by the loss of dopaminergic neurons in substantia nigra, associated with abnormal iron load. The assessment of presymptomatic biomarkers predicting the onset of neurodegenerative disorders is critical for monitoring early signs and understanding the causal relationship between iron accumulation processes and disease development. Here, we used Quantitative Susceptibility Mapping (QSM) and 7T MRI to quantify iron deposition in Nigrosome 1 (N1) in

PD patients, iRBD patients and healthy controls and investigated group differences and correlation with disease progression.

We evaluated the radiological appearance of N1 and analyzed its iron content in 46 PD patients, including 43 early PD (ePD), 36 iRBD patients and 14 healthy controls via T2*-weighted sequences and susceptibility (χ) maps. A follow-up scan was performed after 3 years on 8 iRBD patients. N1 ROIs were manually drawn on control subjects and warped onto a study-specific template to obtain probabilistic N1 ROIs. For each subject the N1 with the highest mean χ was considered for statistical analysis.

The appearance of N1 was rated pathological in 45% of iRBD patients. ePD patients showed increased N1 χ compared to iRBD patients and HC but no correlation with disease duration, indicating that iron load remains stable during the first stages of disease progression. Although no difference was reported in iron content between iRBD and HC, N1 χ in the iRBD group increases as the disease evolves, showing a steeper increment when approaching conversion to synucleinopathies.

QSM can reveal temporal changes in N1 iron content and its quantification may represent a valuable presymptomatic biomarker to assess neurodegeneration in the prodromal stages of PD.

4.2 Introduction

Parkinson's Disease (PD) is a progressive and disabling neurodegenerative disease more frequent in elderly people [169], characterized by striatal dopamine deficiency and motor symptoms as bradykinesia, muscular rigidity, rest tremor and postural instability [170].

Pathological hallmarks of the disease are the loss of dopaminergic neurons, mainly in substantia nigra (SN) pars compacta (SNc), and the accumulation of intra-cytoplasmic Lewy bodies inclusions containing misfolded α-synuclein [170,171]. Evidence suggests that these pathological changes appear years before the onset of symptoms

[170,171] and that 68% of dopaminergic neurons of the ventrolateral tier of the SNc are lost at the time of clinical onset [171].

Current medical therapies aim to treat motor symptoms mainly by restoring the striatal dopamine levels, whereas treatments to prevent, halt or slow the rate of disease progression are not yet available [169]. The future availability of neuroprotective and disease-modifying drugs would represent a milestone in the pharmacological treatment of PD. In this context, the presymptomatic phase of PD is of huge relevance in the search for biomarkers of neurodegeneration occurrence and of forthcoming phenoconversion.

Recently, the idiopathic rapid eye movement (REM) behavioral disorder (iRBD), a parasomnia characterized by dream enacting behaviors related to the loss of muscular atonia during REM sleep [172], has been recognized as a predictor of neurodegenerative diseases [173]. iRBD confirmed by polysomnography has a prevalence of about 0.74-1.15% in the general population [174–176] and patients have an increased risk of developing parkinsonism compared to control populations [177]. Synucleinopathies, in particular PD and Dementia with Lewy Bodies (DLB), are the neurodegenerative diseases more commonly developed by iRBD patients [173,178], with the overall risk for neurodegeneration increasing over time and reaching 96.6% at 14 years follow-up [173].

In recent years, an abnormal radiological appearance of SN has been reported in most PD patients [179–181] and then also in a variable share of iRBD patients [182–184]. In particular, the SNc ventralis and the Nigrosome 1 (N1), an ovoid shape area within the dorsolateral border of the SNc, were described as abnormally hypointense in T2*-weighted images.

The abnormal nigral iron storage has also been documented and estimated using Quantitative Susceptibility Mapping (QSM) assessing altered susceptibility (χ) in the whole SN [44,45,185–187], in the SN pars reticulata [188,189] and in the SN pars compacta [188–191], but without purposely targeting N1.

As the risk of forthcoming conversion is higher in iRBD patients with dopamine transporter Single Photon Emission Tomography (123I-FP-CIT SPECT) evidence of nigro-striatal involvement [192] and iRBD patients with N1 hypointensity also have reduced striatal 123I-FP-CIT uptake [182,184,193], MRI could represent a useful tool for improving our insight into the presymptomatic stage of PD and N1 abnormality may be a marker for short-term risk of overt synucleinopathy occurrence in iRBD patients [193].

Here we employed QSM at ultra-high magnetic field to investigate differences in N1 iron deposition between PD patients, iRBD patients and healthy controls, and between specific subgroups of patients. Then, we explored the evolution of N1 iron accumulation over time in both iRBD and PD patients.

4.3 Methods

4.3.1 Subjects

Consecutive outpatients referring to the Movement Disorders Center of the University of Pisa with a clinical diagnosis of PD or iRBD were recruited during 2015–2020. Diagnosis of PD was performed based on the UK Parkinson's Disease Brain Bank criteria (Hughes et al., 1992). The presence of RBD was diagnosed based on the *International classification of sleep disorders* of the American Academy of Sleep Medicine published in 2014 [194]. Exclusion criteria were claustrophobia or any other contraindication to perform MRI at 7T and the presence of gene mutations associated with PD. According to these criteria, 65 PD patients and 36 patients with iRBD were enrolled in this study, together with a population of 16 healthy controls (HC) with no movement disorder and no neurological or psychiatric diseases, and comparable sex and age distribution. Eight iRBD patients also underwent a follow-up MRI session after 3 years on average from the baseline scan. This study was

approved by the local ethical committee; all participants gave their written informed consent.

4.3.2 Clinical data

Patients were clinically evaluated by neurologists experienced in movement disorders on the day of the MRI exam and at follow-up examinations. On the day of the MRI procedure, the diagnosis of Parkinsonism in iRBD patients was excluded. At all clinical examinations of iRBD patients, the following data were recorded: age, sex, disease duration, follow-up duration and conversion time from iRBD to synucleopathies, when applicable. For PD patients, age, sex, disease duration, the Hoehn and Yahr (H&Y) [195] score, the presence of RBD and the clinical phenotype, i.e., Tremor Dominant (TD) or Postural Instability Gait Disorder (PIGD) were recorded. For all patients, motor function was assessed using the Unified Parkinson's Disease Rating Scale motor item (UPDRS-III), while cognitive screening was performed via Mini-Mental State Examination (MMSE).

4.3.3 MRI acquisition hardware

All subjects underwent an ultra-high field MRI examination at the IMAGO7 Foundation in Pisa, Italy, using a GE Healthcare Discovery MR950 7-T MRI system (GE Healthcare, Milwaukee, WI, USA). The scanner was equipped with a two-channel transmitter/32-channel receiver head coil (Nova Medical, Wilmington, MA, USA) and a gradient system with maximum amplitude = 50 mT/m and slew rate = 200 T/m/s.

4.3.4 MRI imaging protocol

The MRI protocol included two 3D Gradient Recalled Multi-Echo sequences (Susceptibility Weighted Angiography – SWAN, GE Healthcare). One was acquired for the qualitative evaluation of the structures affected by the diseases with the following parameters:

Repetition Time TR = 55.7 ms; eight equally spaced echoes with the Echo Time TE_1:ΔTE:TE_8 = 5.57 : 5.1 : 41.5 ms; acquired voxel size = 0.5 × 0.5 × 1.2 mm^3; reconstructed voxel size = 0.313 × 0.313 × 1.2 mm^3; Flip Angle FA = 8°; in-plane FOV = 160 × 160 mm^2; through-plane coverage = 24 mm; parallel imaging ASSET (Array Coil Spatial Sensitivity Encoding) acceleration factor = 2, scan duration = 4'02". The acquisition targeted the midbrain and was oriented in the plane perpendicular to the floor of the fourth ventricle. This T2*-weighted sequence will be hereafter referred to as "morphological".

The second sequence was acquired to perform a quantitative assessment of iron deposition via QSM, and will be hereafter referred to as "complex-valued" dataset. The acquisition parameters were set as follows: TR = 54.1 ms; seven equally spaced echoes with TE_1:ΔTE:TE_7 = 5.6 : 6.0 : 41.8 ms; voxel size = 0.6 × 0.6 × 0.6 mm^3; FA = 15°; in-plane FOV = 160 × 160 mm^2; through-plane coverage = 36 mm; parallel imaging ASSET (Array Coil Spatial Sensitivity Encoding) acceleration factor = 2, scan duration = 5'04". This sequence covered the brain from the pontomesencephalic junction to the splenium of the corpus callosum and was prescribed perpendicular to the floor of the fourth ventricle. Both the real and imaginary parts of the images obtained at each echo were saved and converted into magnitude and phase data.

4.3.5 QSM reconstruction pipeline

To obtain magnetic susceptibility maps, the processing of the "complex-valued" dataset was performed as follows. The raw phase images of individual echoes were unwrapped using a Laplacian-based algorithm [3,12]. A brain mask was generated using FSL 5.0.9 Brain Extraction Toolbox (*bet*) [137] (FMRIB Software Library, Oxford Centre for Functional MRI of the Brain, Oxford, UK) on the T2*-weighted image averaged across echoes and then used for the removal of the background field via V-SHARP [8]. QSM images were obtained by applying the iLSQR [12,13] method separately to each echo, and then averaged to obtain one susceptibility map with higher signal-to-noise ratio (SNR) for

statistical analyses [139]. The Laplacian-based algorithm for phase unwrapping, V-SHARP and iLSQR are implemented in STI Suite (MATLAB toolbox from UC Berkeley, Berkley, CA, USA) [138].

4.3.6 Qualitative data inspection

The T_2*-weighted images obtained from the magnitude of the 3D GRE signal were evaluated by a neuroradiologist and graded based on the severity of motion artifacts into three categories: "none/mild" corresponding to non-visible or little motion artifact, "moderate" for detectable motion and "severe" for extreme motion artifacts. Images affected by "severe" motion artifacts were excluded from the analysis.

4.3.7 Qualitative evaluation of T2-weighted "morphological" images*

The "morphological" T2*-weighted images were averaged across TEs to increase SNR. Then, they were visually inspected by a neuroradiologist experienced in neurodegenerative disorders and in ultra-high field MR imaging. The anatomy of the substantia nigra of each subject was examined according to established criteria [180], which assess the appearance of the trilaminar organization of the SN and the presence of an oval-shaped hyperintensity located dorsolaterally in the SN between two hypointense layers, corresponding to nigrosome 1. The images were labeled as "normal" where these structures were clearly visible in both left and right SN, or "pathological" when this was not the case in at least one side of the brainstem.

4.3.8 ROI selection

For the QSM-based quantitative analysis, we selected regions of interest (ROI) covering the nigrosomes 1 (N1) in both right (R) and left (L) hemispheres. These regions were manually segmented on the high-resolution T2*-weighted "morphological" images of healthy controls, on a single slice in which they were more clearly visible. Then, an atlas of

the corresponding probabilistic ROIs was created as follows. First, the correction of bias of the TE-averaged T2*-weighted "morphological" images was performed using *3dUnifize* in AFNI [196] and non-brain tissues were removed via *bet* in FSL 5.0.9. Then, these bias-corrected skull-stripped images of the healthy controls were employed to build a study-specific template using antsMultivariateTemplateConstruction routine in ANTs (Advanced Normalization Tools) with Greedy-SyN approach and cross-correlation similarity metric [159]. Afterward, the "morphological" image of each patient was warped to the template space via antsRegistration with Greedy-SyN approach and cross-correlation similarity metric [159]. The ROIs of each healthy control were warped to the study-specific template by applying the corresponding transformation. As we are dealing with 2-D ROIs, we employed linear interpolation method to avoid the loss of voxels belonging to the mask falling in between slices in the template space. Then, the obtained masks were binarized. Probabilistic ROIs were computed by averaging the transformed ROIs across all healthy controls and then thresholded to a probability of 0.4 for the following analyses. The pipeline for the creation of the template and of the probabilistic ROIs is schematized in Figure 4.1.

4.3.9 Quantitative analysis

The magnitude of the "complex-valued" datasets were bias-corrected via *3dUnifize* in AFNI and skull-stripped via *bet* in FSL 5.0.9. The "morphological" T2*-weighted image of each subject was aligned to the magnitude of corresponding "complex-valued" image by computing an affine transformation using *antsRegistration*. This transformation was inverted and concatenated to the non-linear deformation field calculated previously on the "morphological" images in order to warp the QSM images of each subject onto the template space (Figure 4.1). Then, they were averaged to create a study-specific QSM template. As the "morphological" image is missing for one patient, the corresponding magnitude of the "complex-valued" dataset was directly warped to the template space.

For each subject, we identified the N1 (left or right) showing the highest mean susceptibility (χ) and considered it for statistical analysis, according to radiological criteria [180] . Measured χ is reported in parts per million (ppm). To avoid assumptions on brain areas impaired by the disease, we did not reference QSM values with respect to any specific region [85].

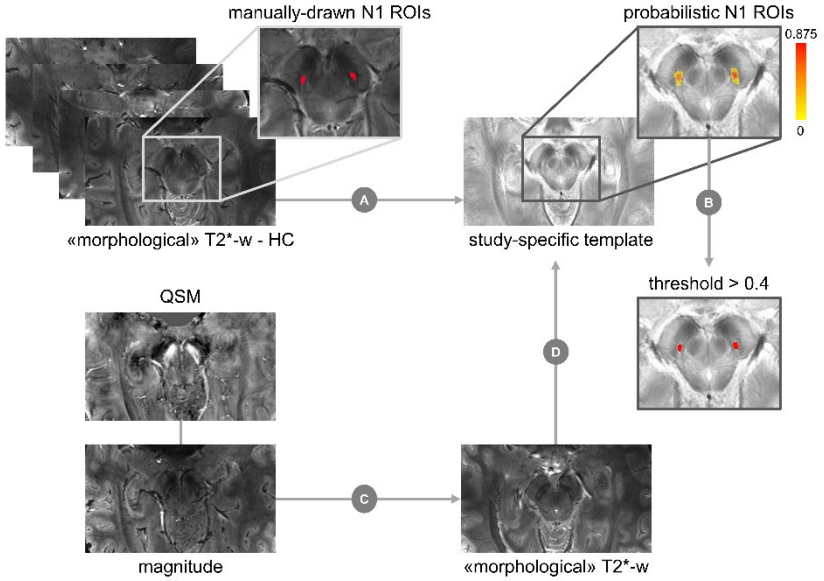

Figure 4.1: Pipeline for template creation and QSM registration. ROIs encompassing N1 were manually drawn on the "morphological" T2*-weighted images of healthy controls. These images were bias-corrected, skull stripped and used to create a study-specific template (A). The probabilistic N1 ROIs were obtained by averaging the ROIs drawn on each control subject and warped to the template and were then threshold to 0.4 and binarized (B). The magnitude of the "complex-valued" dataset of each subject was aligned to the corresponding "morphological" T2*-weighted image (C). Then, a transformation warp was computed to transform the "morphological" image to the template space (D). Finally, the transformations were concatenated to warp the QSM image onto the template (C+D).

4.3.10 Statistical analysis

Statistical analysis was performed in MATLAB (MathWorks, Natick, MA, USA). Sex distribution of the populations (PD, iRBD and HC) were compared using chi-square test. Clinical and QSM data were analyzed via non-parametric statistical tests, i.e., Kruskal-Wallis omnibus tests followed by Dunn's test for post-hoc analysis and Dunn-Sidak correction for multiple comparisons. The area under the curve (AUC) of the receiver operating characteristic (ROC) curve was employed as a measure of diagnostic accuracy. The correlation between susceptibility values and disease duration was evaluated with the Spearman rank correlation test. The threshold of statistical significance was set to $p < 0.05$.

4.4 Results

The study-specific template and the probabilistic ROIs were computed from the "morphological" dataset of all HC. After visual inspection and rating of the magnitude image of the "complex-valued" dataset by a neuroradiologist, 19 PD patients, 6 patients with iRBD and 2 controls were excluded from QSM analysis due to severe motion artifacts. The demographic and clinical distribution of the population used for QSM analysis are summarized in Table 4.1. Specifically, the QSM population included:

- 14 HC (7 females, 58 ± 10 [43-77] years old);
- 30 iRBD patients (6 females, 66 ± 10 [32-81] years old) with an average disease duration of 5 ± 4 [1-13] years and an average follow-up duration after the MRI of 24 ± 14 [5-50] months (3 patients were lost to follow-up);
- 46 PD patients (11 females, 59 ± 12 [35-81] years old). Among PD patients, 43 underwent MRI in early stages of PD (disease duration ≤ 4 years; 11 females, 60 ± 12 [35-81] years old) with either Young-Onset (YOPD; ≤ 45 years old; 8 patients, 1 female, 39 ± 4 [35-45] years old) or Late-Onset (LOPD; 35 patients, 10 females, 64 ± 8 [50-81] years old).

Five iRBD patients (17%) developed PD (4 patients) or Dementia with Lewy Body (DLB) (1 patient) by the end of the follow-up observation period.

Within the group of iRBD patients who underwent two MRI sessions, six had the diagnosis of iRBD confirmed, while two converted to PD before the second session. The average interval between the first MRI session and the follow-up was 38 ± 4 months (37 months on average for the non-converted patients and 42 and 43 months for the two converted patients).

We found no significant differences in sex distribution between groups. Age differences between groups were significant ($p < 0.01$): specifically, age distribution of the iRBD group was different from that of HC ($p < 0.05$) and PD ($p < 0.05$). However, no significant correlation was found between age and χ values in N1 for any group.

	PD	iRBD	HC
N	46	30	14
Sex (females)	11	6	7
Age (years)	69 ± 12 [35-81]	66 ± 10 [32-81]	58 ± 10 [43-77]
Disease duration (years)	3 ± 2 [0.5-11]	5 ± 4 [1-13]	-
Follow-up duration (months)	-	24 ± 14 [5-50]	-
Phenotype (PIGD/TD)	33% / 66%	-	-
H&Y	1.6 ± 0.5 [1-2.5]	-	-
UPDRS-III	17.3 ± 6.1 [7-33]	2.6 ± 2.1 [0-7]	-
MMSE	29.5 ± 0.7 [27-30]	28.9 ± 2.0 [20-30]	-
N1 χ [ppm]	0.071 ± 0.022	0.044 ± 0.027	0.047 ± 0.015

Table 4.1: Demographic and clinical information of the population used for QSM analysis. For the iRBD group, clinical scores reported here refers to the baseline evaluation at the time of the first MRI session. The reported χ value refers to the nigrosome 1 with the highest QSM value for each subject (i.e., either left or right side).

4.4.1 Qualitative imaging results

The appearance of nigrosome 1 in the "morphological" T2*-weighted images was labeled as pathological in 40/46 (87%) PD patients, in particular in 37/43 (86%) early PD and 3/3 (100%) late PD. At baseline evaluation in the iRBD group, one patient was excluded due to motion artifacts in the "morphological" image and 13/29 (45%) reported abnormal N1 appearance, while this was the case for 4/5 (80%) iRBD patients that converted to PD or DLB. The follow-up evaluation for the 6 iRBD patients who underwent two MRI sessions confirmed the baseline assessment in 3 cases (2 rated as normal and 1 as abnormal) and documented a worsening in N1 appearance in 1 case, rated as normal at the first exam and abnormal in the follow-up. The remaining 2 patients (1 with normal and 1 with abnormal imaging at the first scan) had the follow-up image excluded from the qualitative analysis due to motion artifact. In the control population, 2/14 (14%) exhibited N1 alterations. Normative and pathological imaging in exemplary subjects is displayed in Figure 4.2.

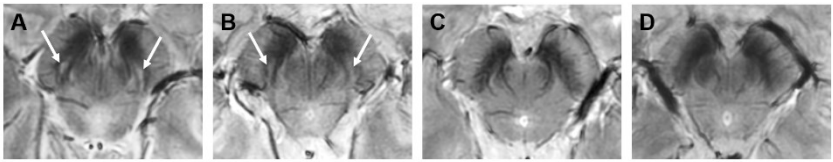

Figure 4.2: "Morphological" T2*-weighted images of the nigrosome 1 in four representative subjects. In healthy controls (A), N1 appears as an oval-shaped hyperintensity (white arrows) surrounded by two hypointense layers and located dorsolaterally in the SN. This structure is also visible in some patients with iRBD (B), while this is not the case for other iRBD patients (C) and for the great majority of PD patients (D).

4.4.2 Quantitative imaging results

After selecting the N1 ROI with the highest susceptibility for each subject, we compared the average QSM values between groups. No

significant differences between young- and late-onset PD were found (Figure 4.3A), so they were merged into one group of early PD (ePD) for further analysis. Similarly, χ values measured in iRBD patients who converted to synucleinopathies by the end of the follow-up period (iRBD-C) and in iRBD patients who had not yet converted (iRBD-NC) were not significantly different (Figure 4.3B), therefore the two groups were considered together. Susceptibility in N1 was not significantly different in ePD patients with or without RBD symptoms (Figure 4.3C).

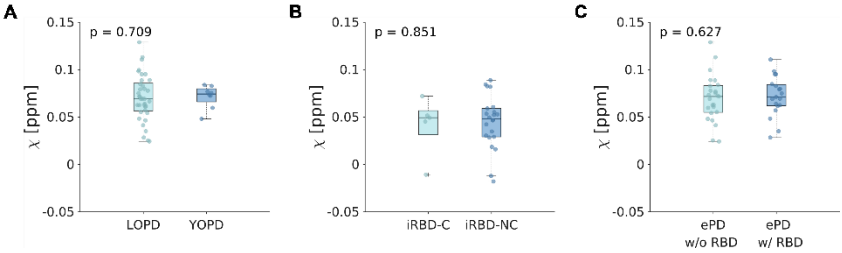

Figure 4.3: Box plots showing comparisons of N1 susceptibility between groups: no significant differences were found between LOPD and YOPD (panel A), between iRBD-C and iRBD-NC (panel B) and between PD patients with or without RBD (panel C). The p-value of the Dunn's test is reported in the top-left corner of the corresponding plot.

The omnibus test revealed significant differences in N1 susceptibility between ePD, iRBD and HC ($p < 0.0001$): in particular, ePD patients showed increased χ with respect to both HC ($p < 0.01$) and iRBD ($p < 0.0001$), as shown in Figure 4.4A. The AUC obtained in discriminating ePD from iRBD patients was 0.77, with a specificity of 0.80 and a sensitivity of 0.73. Moreover, PD and HC could be discriminated with an AUC of 0.83, a specificity of 0.93 and a sensitivity of 0.71 (Figure 4.4B).

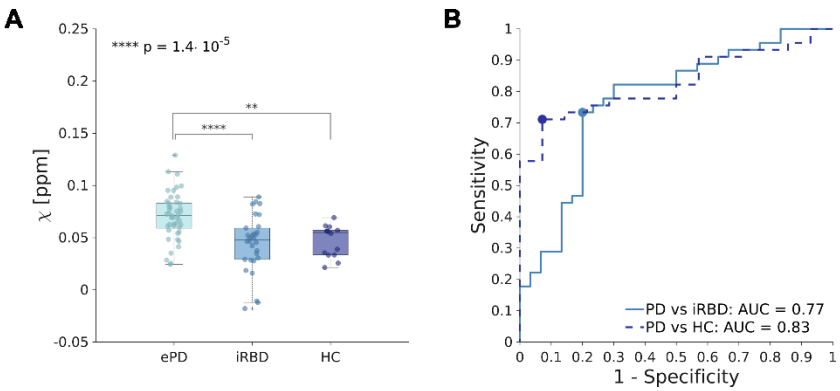

Figure 4.4: Box plot displaying group differences in N1 susceptibility between ePD patients, iRBD patients and HC (panel A). In the top left corner, we reported the p-value of the omnibus Kruskal-Wallis test. Post-hoc Dunn's tests reaching significance after Dunn-Sidak correction are indicated by asterisks (* $p < 0.05$, ** $p < 0.01$, *** $p < 0.001$, **** $p < 0.0001$). Panel B shows the ROC curves computed when discriminating PD from iRBD (solid line) and PD from HC (dashed line). The dots represent the optimal cut-off values of each curve.

We split the iRBD population into two subgroups: one including patients with normal N1 appearance in the T2*-weighted image (iRBD-) and one comprising those with pathological imaging (iRBD+). Although χ difference did not reach statistical significance, we measured higher QSM values in iRBD+ patients (Figure 4.5A). This led to a smaller difference with the ePD group ($p < 0.05$) (Figure 4.5B) compared to that reported when considering the entire iRBD cohort (Figure 4.5A), but no statistically significant difference is reported comparing iRBD+ to HC.

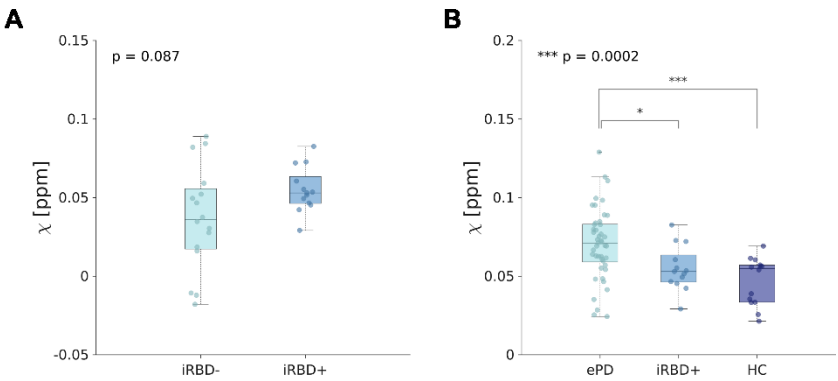

Figure 4.5: Box plot displaying group differences in N1 susceptibility considering iRBD patients with normal (iRBD-) and pathological (iRBD+) qualitative imaging separately. Although the difference does not reach significance, iRBD+ patients reported slightly higher χ, on average, than those in iRBD- group (panel A). Similarly, panel B shows that the difference in N1 χ with ePD patients is reduced when considering iRBD+ patients only instead of the whole iRBD population (Figure 4.4A). In the top left corner, we reported the p-value of the omnibus Kruskal-Wallis test. Post-hoc Dunn's tests reaching significance after Dunn-Sidak correction are indicated by the asterisks (* $p < 0.05$, ** $p < 0.01$, *** $p < 0.001$).

Statistically significant positive correlation ($r = 0.475$; $p < 0.01$) emerged between susceptibility in N1 and disease duration in iRBD patients (Figure 4.6A). Instead, no significant correlation was found between N1 χ and disease duration in PD patients (Figure 4.6B).

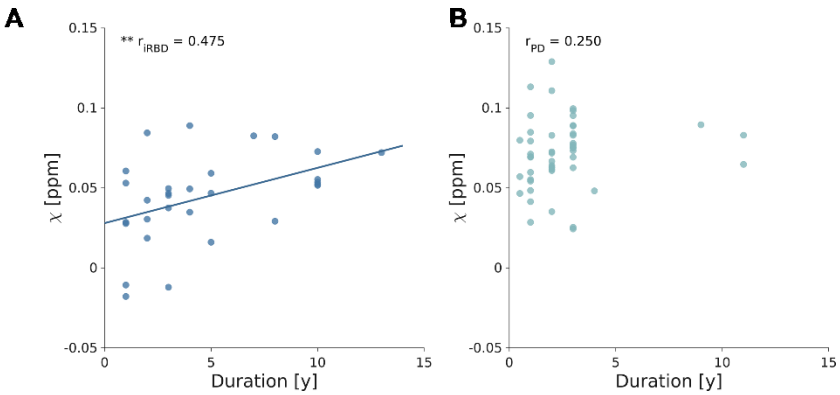

Figure 4.6: Correlation of N1 χ and disease duration. A significant positive correlation was found for iRBD ($p < 0.01$; panel A) but not for the PD group (panel B).

Longitudinal analysis was performed to assess variations of susceptibility in both left and right N1 (N1L and N1R, respectively) from the time of the first baseline acquisition (tB) to the time of the follow-up scan (tF). We compared iRBD patients who have not yet converted by the end of the observation period (iRBD-NC) and iRBD patients that developed PD by the second MRI session (iRBD-C). For these patients, we found a steeper χ increase over 3 years ($\Delta\chi_{N1R} = 0.0028\,ppm$, $\Delta\chi_{N1L} = 0.0194\,ppm$) with respect to iRBD-NC ($\Delta\chi_{N1R} = -0.0047\,ppm$, $\Delta\chi_{N1L} = -0.0019\,ppm$) (Figure 4.7A-B). However, the susceptibility at the time of the second MRI scan is not significantly different between the two groups.

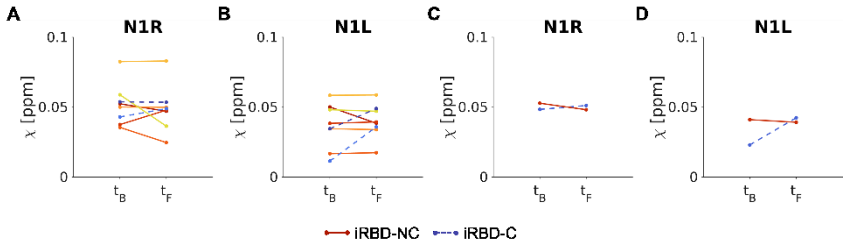

Figure 4.7: Longitudinal analysis. Panels A and B show the susceptibility measure at the time of the first (tB) and of the second (tF) MRI in right and left N1, respectively. Each color represents a subject. Reddish solid lines indicate iRBD-NC patients, while blueish dashed lines refer to iRBD-C patients. In panels C and D, we reported the data of panels A and B averaged over each group. The mean variation of χ is larger for iRBD-C patients compared to the iRBD-NC group.

4.5 Discussion

This study focused on exploring the potential of N1 magnetic susceptibility as a non-invasive biomarker for synucleinopathies and their prodromal stages, such as iRBD. Specifically, we recruited PD patients, iRBD patients and healthy controls and acquired a GRE sequence for susceptibility mapping on a 7T MRI system. We measured susceptibility in nigrosome 1 in order to detect group differences in iron load, assess its increase as long as the disease progresses and longitudinally evaluate its variability at the time of conversion to α-synucleinopathies. To the best of our knowledge, this is the first QSM study targeting N1 in a population of iRBD patients at 7T.

We reported increased N1 susceptibility in ePD patients with respect to the iRBD group and HC and demonstrated that QSM can discriminate ePD patients with good diagnostic accuracy. Instead, no differences between iRBD patients and HC were found. Within the ePD group, we explored the effect of clinical variables such as late- or young-onset and RBD presence: no significant differences emerged between LOPD and YOPD or between ePD with and without RBD symptoms. No differences

were detected between iRBD-C and iRBD-NC, as well. Susceptibility was higher -though not significantly- in iRBD+ patients than in iRBD- group. We found a significant positive correlation of N1 χ with disease duration in iRBD patients, while it was not the case for the PD group. The longitudinal analysis highlighted a larger variation of χ in iRBD patients that had converted to synucleinopathies by the time of the follow-up MRI scan, with respect to the ones for which the iRBD diagnosis was confirmed.

Iron concentration in N1 was higher for ePD patients than for the control group. This is in agreement with previous studies that investigated susceptibility in SNc [44,188–191,197] and in its dorsolateral portion [198]. The role of iron in neurodegeneration has not been completely elucidated, as the impairment of its metabolism can lead to cell damage via oxidative stress and/or it can be stored in cerebral tissue as the consequence of cell death [147]. Abnormal iron storage has been documented in target areas in PD [199] as well as in other neurodegenerative diseases [200,201]. In PD, the iron deposition in the SN, and especially in SNc, increases along with disease staging and has been found in many different cell types including inflammatory cells and melanized dopamine neurons of SNc [199]. We can then suppose that iron accumulation is related to neuronal death; in this case, the susceptibility increase in SNc and N1 of PD patients would not be surprising, as that is the SN region with the greatest disease-related neuronal loss [171].

The absence of a correlation between N1 χ and age in ePD patients, iRBD and control subjects is in line with the relatively limited involvement of the ventrolateral tier of SNc in aging, as it is the SN tier less affected by age-related neuronal loss (with an estimated cell loss of 11% at 60 years old) [171].

The accumulation of iron in N1 in the iRBD group is comparable to that in HC, in accordance with previous studies that observed no differences in T2* in SN between iRBD patients and controls [202,203] and with

recents works that considered average QSM values in the whole SN [204,205] or in its functional subregions [206]. However, another study reported higher susceptibility in iRBD patients compared to HC, but significantly lower than in PD [187]. The slightly inconsistent results reported so far can be accounted for by the different degree of striatal dopamine deficiency in iRBD patients enrolled in each study, and by the use of a reference region for susceptibility measures. Previous studies showed a variable prevalence of pathological MR imaging in iRBD patients, ranging between 27.5% and about 77% [182–184,193]. iRBD+ patients have a peculiar level of putaminal dopaminergic SPECT activity as it has been found lower than in both iRBD- patients [184,193] and healthy controls [193], but higher than in PD patients [193]. Therefore, the number of patients with impaired putaminal dopaminergic projections and the degree of the dopaminergic deficiency could affect the results of both qualitative and quantitative MR studies. Second, in our analysis and in two other studies [204,205] susceptibility values were not referenced to a specific anatomical area, to avoid assumptions on brain regions not involved in neurodegeneration, as the populations considered in this study may show a diffuse pattern of pathological alterations in both gray and white matter: this strategy may lead to slightly different results from those obtained with referencing [187,206]. In addition, we selected a small ROI covering only the nigrosome 1 while the whole SN was considered in other studies [187,204,205]. Further investigations are required to settle this discrepancy. Lastly, even though the degeneration affects SN subregions other than N1, it seems unlikely that the iron deposition could alter more the mean χ value of SNc than that of N1.

The correlation between N1 χ and duration of iRBD points out that iron accumulation increases along with the disease evolution, confirming a previous observation [187]. As no differences are reported between ePD patients with or without RBD, we hypothesize that the gradual increment in iron stores in N1 may happen prior to the emergence of motor symptoms, irrespective of the presence of RBD. Moreover, despite a slow increase over time, no correlation was found between PD duration and susceptibility in N1, so it can be assumed that further iron

accumulation is not significant once motor symptoms appear. Concerning this finding, the literature provides inconsistent observations, as the positive correlation of susceptibility in SN with disease duration was reported by some previous works [207], especially for PD patients with longer disease duration [197] but not confirmed by others [187]. In this regard, one possible confounding factor relates to the prevalence of PD patients with short disease duration generally enrolled in these studies. In this work, only 3 subjects had a disease duration longer than 4 years (i.e., 9, 11 and 11 years). This may cause long-term correlations to remain undetected. Another possible explanation is the different percentage of dopaminergic neurons which die after clinical onset in the whole SNc (where about 52% of cells are still alive) and in its ventrolateral tier (where there are still about 32% of cells) [171]. Even though the neuronal death continues exponentially, the influence on susceptibility measures is expected to be greater for SNc than for N1. On these premises, we may hypothesize that the iron load in N1 is not an index of disease progression and severity, at least in the first years of PD, but rather a marker of ongoing neurodegeneration in presymptomatic stages.

The longitudinal analysis on iRBD patients with a follow-up MRI examination after 3 years from the baseline revealed a larger increase of iron content in N1 for patients that developed α-synucleinopathies by the second examination, with respect to the ones for which the iRBD diagnosis was confirmed. However, the susceptibility values at the time of the follow-up are comparable between iRBD-C and iRBD-NC patients. This may suggest that iron load at the moment of the conversion to neurodegenerative motor disorders does not represent a fixed threshold, but it may show inter-subject variability ascribable to factors such as the capability of residual neurons to supply the dysfunctions caused by neuronal loss. However, this should be considered a preliminar and speculative result because of the small size of the sample available for this analysis. Further investigation will be carried out during future follow-ups.

From the methodological point of view, the ROIs covering N1 used in this study were manually drawn by an experienced neuroradiologist on a high-resolution T2*-weighted image of the control subjects. Then, a probabilistic atlas was created and used to evaluate N1 χ in all subjects. The rationale for this approach concerned the absence of a published N1 ROI and the critical issues in drawing it on structures with pathological appearance. This semi-automated approach removed the user's discretionality in drawing the small N1 ROIs on the single patient. To ensure that the results were not affected by coregistration errors, a neuroradiologist checked the alignment of each subject to the template. In the future development of this study, the rating of "morphological" T2*-weighted will be blindly repeated by the same radiologist and also performed by another, in order to provide measures of intra- and inter-rater reproducibility of the qualitative assessment of the images. In this work, we performed the statistical analysis on the χ map obtained by averaging QSM images across TEs to increase SNR [139]. Considering the known dependence of χ values on TE [91,92], we repeated group comparison analysis using maps obtained at individual TEs to assess the robustness of our results. As shown in Supplementary Figure S4.1, even though measured susceptibility varies, we obtained similar results for each TE except the longest one (41.8 ms), possibly due to low SNR. The stability of the statistical outcome across TEs could be due to a consistent difference in N1 iron accumulation for the three populations which reaches high levels of significance independently of TE.

An alternative approach for future studies may involve the usage of histogram and pattern analysis on the whole volume of SN. This would allow the exploration of the tails of the χ distribution and of its fine spatial variations, so as to also taking into account N1 spatial variants [208].

The choice of selecting and analyzing the N1 with the highest susceptibility is supported by clinical and radiological findings and pointed out to maximize the sensitivity in revealing neurodegeneration in both ePD and iRBD patients. Motor symptoms of PD are, indeed,

usually asymmetric [169] and this asymmetry matches with the different N1 visibility [209]. It is therefore commonly accepted to define an imaging "pathological" in case of the loss of N1 visibility in at least one side of the midbrain [179,180,210].

In conclusion, we reported that the iron content in N1 of iRBD patients is comparable to those in HC but it grows as the disease evolves, showing a steeper variation in the proximity of conversion to synucleinopathies. On the contrary, PD patients show increased N1 iron load with respect to iRBD and HC but our results suggest that it remains roughly unaltered during disease evolution. Even though N1 iron content may not be an index of PD progression, at least during its first stages, our work suggests the potential of N1 iron load detection via QSM as a presymptomatic biomarker for the assessment of PD and of ongoing neurodegeneration in its prodromal stages, such as iRBD. Longitudinal studies are warranted to get further insights into the mechanisms of iron accumulation and their causal relationship to disease development.

Supplementary Figures

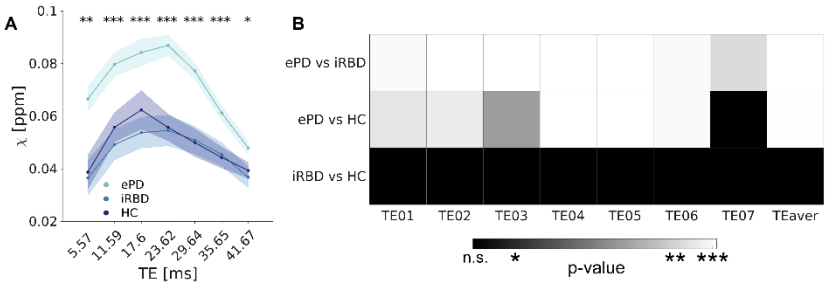

Figure S4.1: Dependence on TE of N1 QSM values (Panel A). Each plot displays the mean susceptibility in N1 for the three groups: ePD (aqua green), iRBD (pale blue) and MSAc (violet). The shaded area represents the standard error of the mean and the asterisks indicate the TEs at which the difference in mean susceptibility across groups reaches significance in the Kruskal-Wallis omnibus test (* $p < 0.05$, ** $p < 0.01$, *** $p < 0.001$). Panel B displays the statistical results of the post-hoc comparisons of QSM mean values in N1 among the three groups (HC, PD and iRBD) via Dunn's test followed by and Dunn-Sidak correction for multiple comparisons for each TE (indicated as TE01-TE07) and for the map obtained by averaging all TEs (TEaver). The gray-levels indicate p-values (n.s.: not significant; * $p < 0.05$, ** $p < 0.01$, *** $p < 0.001$). Similar results were obtained for each TE, except the longest one (41.8 ms) in the comparison between ePD and HC, probably due to low SNR.

Chapter 5 Complementing canonical fMRI with functional Quantitative Susceptibility Mapping (fQSM) in modern neuroimaging research

The work presented in this chapter was performed in collaboration with the IMAGO7 Research Center (Pisa, Italy).

It is an extension of a preliminary study published in 2019 [114]: Costagli, M., Lancione, M., Cecchetti, L., Pietrini, P., Cosottini, M., Ricciardi, E., & Tosetti, M. (2019). *Quantitative Susceptibility Mapping of Brain Function During Auditory Stimulation.* IEEE Transactions on Radiation and Plasma Medical Sciences, 3(4), 516-522.

It has been published as follows [211]:

Lancione, M., Costagli, M., Handjaras, G., Tosetti, M., Ricciardi, E., Pietrini, P., Cecchetti, L. (2021). *Complementing canonical fMRI with functional Quantitative Susceptibility Mapping (fQSM) in modern neuroimaging research.* NeuroImage, 244, 118574

5.1 Abstract

Functional Quantitative Susceptibility Mapping (fQSM) allows for the quantitative measurement of time-varying magnetic susceptibility across cortical and subcortical brain structures with a potentially higher spatial specificity than conventional fMRI. While the usefulness of fQSM with General Linear Model and "On/Off" paradigms has been assessed, little is known about the potential applications and limitations of this technique in more sophisticated experimental paradigms and analyses, such as those currently used in modern neuroimaging.

To thoroughly characterize fQSM activations, here we used 7T MRI, tonotopic mapping, as well as univariate (i.e., GLM and population

Receptive Field) and multivariate (Representational Similarity Analysis; RSA) analyses.

Although fQSM detected less tone-responsive voxels than fMRI, they were more consistently localized in gray matter. Also, the majority of active gray matter voxels exhibited negative fQSM response, signaling the expected oxyhemoglobin increase, whereas positive fQSM activations were mainly in white matter. Though fMRI- and fQSM-based tonotopic maps were overall comparable, the representation of frequency tunings in tone-sensitive regions was significantly more balanced for fQSM. Lastly, RSA revealed that frequency information from the auditory cortex could be successfully retrieved by using either methods.

Overall, fQSM produces complementary results to conventional fMRI, as it captures small-scale variations in the activation pattern which inform multivariate measures. Although positive fQSM responses deserve further investigation, they do not impair the interpretation of contrasts of interest. The quantitative nature of fQSM, its spatial specificity and the possibility to simultaneously acquire canonical fMRI support the use of this technique for longitudinal and multicentric studies and pre-surgical mapping.

5.2 Introduction

Quantitative Susceptibility Mapping (QSM) [10,94,117–121] is a well-established method based on the phase of the Magnetic Resonance (MR) signal acquired via a Gradient Recalled Echo (GRE) sequence, which allows the non-invasive quantification of tissue magnetic susceptibility (χ). Since susceptibility represents an important biomarker for the quantitative evaluation of iron loads [25], myelination [28,29], hemorrhages and calcification [20,21,212,213], its employment is particularly growing in clinical studies focusing on the diagnosis and follow-up of neurodegenerative diseases, such as Parkinson's disease [43,45,46,51,214], multiple sclerosis [67–69], amyotrophic lateral sclerosis [55,59] and Alzheimer's disease [38,40]. Information provided by QSM

is not only quantitative, but also reflects a local property of the tissues, as free from the non-local dipole effect created by susceptibility sources that instead affect T2*-weighted images.

QSM has been recently applied to functional MRI, as well (i.e., functional QSM - fQSM) [95,110–115,215]. This method relies on the acquisition of a complex-valued GRE-EPI signal (i.e., the simultaneous acquisition of both signal magnitude and phase) [216], with no increase in acquisition time. By removing the non-local dipole effect, fQSM guarantees a more direct measure of the susceptibility variation, which is responsible for the Blood Oxygenation Level-Dependent (BOLD) effect. Hence, fQSM can provide a quantitative and spatially specific correlate of neural activity.

Previous studies assessed the feasibility of fQSM [111,112] and highlighted some of its characteristics. In particular, fQSM has sufficient sensitivity - though lower than magnitude-based fMRI - to detect parenchymal activation [110,111]. This lower sensitivity is balanced by higher spatial specificity due to the removal of the non-local dipole field effect [110,114,115]. A potentially interesting but still unclear property of fQSM is related to the sign of the activation [110,113,114]. The net effect of the variation of the cerebral metabolic rate of oxygen and of cerebral blood flow and volume observed during neuronal activation determines a local increase of oxygenated blood in task-sensitive regions. As deoxy-hemoglobin is paramagnetic (i.e., it has positive susceptibility) and oxy-hemoglobin is diamagnetic (i.e., it has negative susceptibility), during task periods we observe a decrease in tissue susceptibility which leads to an increase in the T2*-weighted signal. Hence, in voxels showing a BOLD fMRI signal increase, a negative fQSM activation is expected. Although this is the case for the vast majority, some voxels show the same directionality in BOLD fMRI and fQSM signal change. Indeed, the presence of both positive and negative fQSM activations complicates the interpretation of contrasts of interest in task-based paradigms. Unexpected directionality in fQSM could be caused by incomplete dipole inversion [110,113], especially near strong susceptibility sources, such as veins. However, this effect has been observed using a broad

range of acquisition parameters and several reconstruction algorithms, suggesting that data processing has a limited impact on this. Therefore, new studies are needed to better clarify the biophysical principles that could explain task-related fQSM signal increments.

Previous works focused on the application of conventional analysis techniques to fQSM data, such as General Linear Model (GLM) for simple task-based "On/Off" experiments. Yet, GLM is not the only approach adopted by the neuroimaging community, and more advanced tools, namely multivariate methods, have become increasingly popular in neuroscientific analytical pipelines. Also, to precisely dissect complex cognitive and affective human abilities, simple "On/Off" task designs have been replaced by paradigms including several experimental conditions. Notwithstanding progress in functional neuroimaging data analysis and study design, a comprehensive assessment of the applicability of these approaches to fQSM data is currently missing.

Here, we used ultra-high field 7T-MRI and fine-grained tonotopic mapping to characterize "unexpected" fQSM responses (i.e., those voxels with equal activation sign in fQSM and fMRI) and to assess the ability of this technique to discriminate between brain responses elicited by different perceptual features, specifically tone frequency. To do this, we used three approaches typically adopted in modern neuroimaging studies: the classic mass-univariate GLM, the population Receptive Field (pRF) method [217], and the Representational Similarity Analysis (RSA) [218].

5.3 Methods

5.3.1 Subjects

Twelve healthy volunteers (6 females, aged 27 - 44 years, 33 ± 6 years old) with normal hearing and no history of neurological diseases or psychiatric disorders were recruited to participate in the study and

underwent a 7 Tesla MRI scan session. All subjects received a medical interview, including a brain structural MRI scan, to exclude any disorder that could affect brain structure or function. All participants gave their written informed consent after the study procedures and potential risks had been explained. The study protocol was approved by the local Institutional Review Board (IRB) (Comitato Etico Area Vasta Nord Ovest - CEAVNO; Protocol No. 1485/2017) and the research was conducted in accordance with national legislation and the Declaration of Helsinki.

5.3.2 Experiment and stimulus design

Stimuli for tonotopic mapping consisted of trains of pure tones (rate: 10 tones per second; duration: 75ms with 5ms cosine ramp in loudness) selected from ten perceptually uniform frequency bands based on the Bark scale [219]: (1) 100-200 Hz; (2) 300-400 Hz; (3) 510-630 Hz; (4) 770-920 Hz; (5) 1080-1270 Hz; (6) 1480-1720 Hz; (7) 2000-2320 Hz; (8) 2700-3150 Hz; (9) 3700-4400 Hz; (10) 5300-6400 Hz). We adopted this particular stimulation paradigm based on narrowband stimuli as it provides high sensitivity in detecting differences in frequency tuning [220]. Pure tones were presented binaurally in blocks of 7.5 seconds followed by randomly selected rest periods of either 7.5 or 10 seconds. The loudness of each block was modulated by a cosine ramp of 0.3 s, to fade in and out and mitigate the startle caused by stimulus onset. The onset of the first stimulus block was preceded by a rest period of 20 s (including 10 s of dummy scans) and each fMRI run ended with an additional 5 s period of silence. A scheme of the stimulation paradigm for one fMRI run is presented in Supplementary Figure S5.1. The ten frequency bands were played in a pseudorandom order across subjects and across the four runs that were acquired in the MRI session. Each frequency band was presented twice per run, summing up to a total of 20 trials per run and 80 trials per scan session, that is 8 trials per frequency band. The duration of one run was 5 minutes and 50 seconds, summing up to 23 minutes and 20 seconds for the whole functional scan. To ensure that all frequency bands were perceived as having comparable loudness, three subjects were asked to equalize the volume of 12 pure

tones ranging 100-8000 Hz with respect to a 1000 Hz reference frequency. This procedure was performed during an EPI scan to account for the scanner noise. The equalization was performed via the QUEST adaptive psychometric method [221], with an initial guess for the algorithm derived from the ISO-226 standard. Afterward, the loudness for each tone was derived via an interpolating fit and further adjusted for each subject to account for possible differences in scanner noise attenuation due to earphone positioning and head padding. Subjects were instructed to passively listen to the stimuli and keep their eyes closed during the entire acquisition.

Stimuli were designed in MATLAB 2017a (Mathworks, Natick, MA, USA) running Psychtoolbox and administered via MR-compatible in-ear earphones (VisuaStimDigital, Resonance Technologies, Los Angeles, USA), connected to a computer placed in the control room.

5.3.3 MRI system

Functional and anatomical MR images were acquired on a GE Healthcare Discovery MR950 7T MRI system (GE Healthcare, Chicago, Illinois) equipped with a two-channel transmitter/32-channel receiver head coil (Nova Medical, Wilmington, MA, USA) and a gradient system with maximum amplitude = 50 mT/m and slew rate = 200 T/m/s.

5.3.4 MRI acquisition

Functional scans were performed by using a 2D gradient echo EPI. Forty-nine slices were prescribed axially and acquired in interleaved ascending order (odd slices first). The prescription partially covered the brain starting from ventral regions, up to perisylvian frontal and parietal territories. The following acquisition parameters were employed for all functional runs: Echo Time (TE) = 21.3 ms, Repetition Time (TR) = 2.5 s, Flip Angle (FA) = 74°, Field Of View (FOV) = 230 × 230 mm^2, matrix size = 128 × 128, in-plane resolution = 1.8 mm, slice thickness = 1.8 mm, parallel imaging ASSET (Array coil Spatial Sensitivity Encoding

Technique) acceleration factor = 3, fat suppression. No resampling was performed during image reconstruction to preserve native resolution.

Each subject underwent one fMRI session, consisting of four runs of tonotopic mapping. To correct for geometric distortions associated with phase-encoding direction, we set opposite gradient polarity (either anterior-to-posterior or posterior-to-anterior) for odd and even runs. Four "dummy" volumes were discarded at the beginning of each run to allow the magnetization to reach the steady-state. The number of acquired volumes for each tonotopy run was 136. For each functional scan, we acquired the complex-valued signal and reconstructed the magnitude and the phase images using a custom code running in MATLAB 2019a.

For anatomical reference, a T1-weighted image was acquired using an MP2RAGE sequence [222]. This is a modified version of a Magnetization-Prepared Rapid Gradient Echo (MPRAGE) scan, based on the acquisition of two low-flip angle images at two different Inversion Times (TI). MP2RAGE sequence was prescribed axially to cover the whole brain and acquisition parameters were set as follows: TR = 6.6 ms; TE = 2.0 ms; Inversion Time $TI_{1,2}$ = 1000, 3200 ms; FA = 5°.; voxel size = 0.8 × 0.8 × 0.8 mm^3, in-plane FOV = 220 × 220 mm^2; sagittal coverage = 176 mm; scan duration = 11′36″).

5.3.5 Functional QSM data reconstruction

A susceptibility map was computed for each acquired volume as follows. Firstly, the raw phase image of each volume was unwrapped via a Laplacian-based algorithm [3,12]. A brain mask was generated using the Brain Extraction Toolbox (*bet*) [137] in FSL 5.0.9 (FMRIB Software Library, Oxford Centre for Functional MRI of the Brain, Oxford, UK) on the magnitude image and then used for the background phase removal. To this purpose, we employed an optimized pipeline for 2D EPI phase processing [223]: the background phase was removed via a 2D version of the Laplacian-based method V-SHARP, followed by 3D V-SHARP [8]. This joint 2D and 3D approach solves the issue of phase

inconsistencies across adjacent slices of 2D EPI. The 2D step removes the in-plane harmonic components of background noise and reduces the phase inconsistencies between slices; then, the 3D step removes the through-plane noise contributions. The iLSQR method [12,13] was applied to tissue phase images of each time-point to obtain QSM maps. The algorithms used for phase processing and QSM reconstruction are implemented in STI Suite (MATLAB toolbox from UC Berkeley, Berkley, CA, USA) [138]. The reconstruction pipeline is illustrated in Figure 5.1A.

5.3.6 Preprocessing of anatomical data

MP2RAGE raw data were reconstructed offline with a custom MATLAB code using Orchestra, a GE Healthcare reconstruction framework. Images corresponding to each inversion time were obtained via Autocalibrating Reconstruction for Cartesian imaging (ARC) followed by adaptive coil combination [224] and vendor-provided gradient non-linearities correction. The final MP2RAGE image was obtained by combining the images acquired with different TIs [222] to produce T1-weighted anatomical images virtually free of intensity bias. After reconstruction, the anatomical images were rigidly aligned along the Anterior Commissure (AC) - Posterior Commissure (PC) plane (AC-PC). Specifically, an affine transformation (12 degrees of freedom) was computed to transform the T1-weighted image into MNI space using *flirt* [136] in FSL 5.0.9. Then, the transformation was converted to rigid body transform (6 degrees of freedom) and applied to the anatomical dataset. Brain extraction was performed via antsBrainExtraction.sh routine in ANTs (Advanced Normalization Tools), using the OASIS dataset as a template. Tissue class segmentation was performed in SPM12 [225] to obtain gray and white matter probabilistic maps that were then resampled to EPI spatial resolution. Linear and non-linear registration to the MNI152 template were performed via *3dQwarp* in AFNI [196] adopting the wsinc5 interpolation method.

5.3.7 Preprocessing of functional data

Data were visually inspected to ensure the absence of excessive motion and scanning artifacts. Preprocessing of the functional datasets was performed in AFNI. Motion correction was carried out via *3dvolreg* in two sequential steps: in the first iteration, all volumes were aligned to the first of each time series to compute the framewise displacement between each pair of successive time points; then, the registration was repeated using the volume showing the smallest displacement as a reference. This procedure ensures that the reference time point is not corrupted by sudden head motion. Rigid body transformations (6 degrees of freedom) were computed and applied to functional time series. Head motion parameters were plotted and inspected to verify data quality and the absence of a significant correlation between motion and stimulus timing. Non-brain tissues were removed using *bet* routine in FSL 5.0.9. B_0 distortion was corrected by applying the following steps: the two pairs of scans acquired with the same gradient polarity were aligned together and averaged. Afterward, the two average images with opposite polarity were coregistered using 3dQwarp and the "meet in the middle" algorithm (*-plusminus* option). After computing the affine transformation matrix of the undistorted average EPI image to the skull-stripped T1-weighted scan via *align_epi_anat.py* routine, the two transformations (the B_0 distortion correction and the alignment to the anatomical scan) were concatenated and applied simultaneously to the functional scans via *3dNwarpApply*. Data were spatially blurred to a Full-Width at Half-Maximum (FWHM) of 6 mm using *3dBlurToFWHM*, a routine that iteratively estimates and increases the smoothness of data until reaching the desired level. Lastly, the time series were demeaned and scaled to percent signal change.

Functional QSM data were motion-corrected and aligned to the anatomical image by applying the transformation computed for conventional fMRI data. To preserve fQSM quantitative information, we applied nearest-neighbor interpolation method, in both fQSM and fMRI pipelines for consistency. Then, data were smoothed up to 6 mm FWHM (*3dBlurToFWHM*) and demeaned. Scaling was avoided to preserve the

quantitative information of the variation of tissue susceptibility, here reported in parts per billion (ppb). The preprocessing steps are summarized in Figure 5.1A.

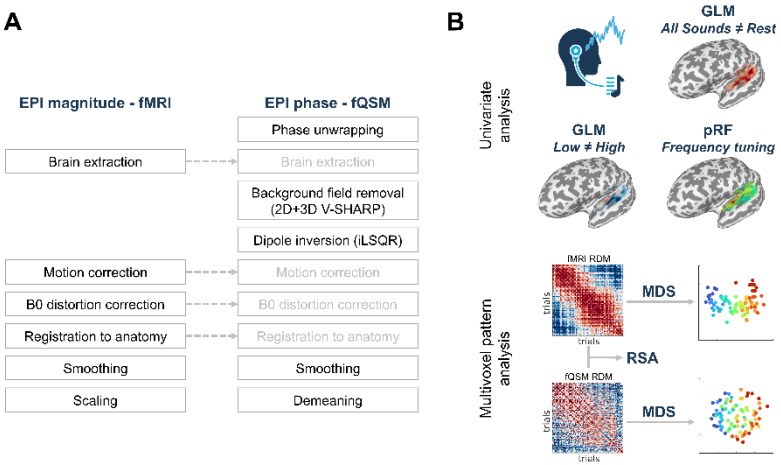

Figure 5.1: Graphical summary of the reconstruction and preprocessing pipelines (panel A) and of the analyses that were performed on the fMRI and fQSM datasets (panel B).

5.3.8 Selection of tone-responsive areas

For each subject, we used AFNI's *3dDeconvolve* to perform a mass-univariate voxelwise GLM analysis [226] on fMRI and fQSM data. Regressors for each individual trial were created by convolving a boxcar function with the canonical hemodynamic response function. Polynomial drifts and six motion parameters (three translations and three rotations) were included as nuisance regressors. For conventional BOLD fMRI, voxels responding to auditory stimulation - i.e., *All Sounds > Rest* - were identified by performing a non-parametric permutation test (two-tailed) on the t-statistic map of each trial using FSL *randomise*, setting a threshold of $p < 0.05$ voxel-wise corrected. We selected the two

largest clusters with positive fMRI response for each subject, together with voxels showing significant negative responses, so as to obtain a functionally defined mask of the Sound Responsive Area (SRA). Even though negative fMRI activations are not usually taken into account, their inclusion in the current analysis allows us to have a fair comparison between conventional BOLD fMRI and fQSM, where the presence of both positive and negative activations is frequently acknowledged. Similarly, a region of active voxels in fQSM with both positive and negative responses was defined via a permutation test with the same statistical threshold used for conventional fMRI. After alignment to the MNI space, a probabilistic SRA Region Of Interest (ROI) was computed by summing the masks across subjects. The peak values of R^2 obtained in SRA for fMRI and fQSM for all subjects were compared with a paired t-test.

5.3.9 Tonotopic mapping

A first contrast of interest was computed on single-subject GLM coefficients, testing the "Low frequencies" (pure tones ranging from 100 to 630 Hz; frequency bands 1 to 3) > "High frequencies" (pure tones ranging from 2700 to 6400 Hz; frequency bands 8 to 10) contrast. In addition, to estimate the frequency tuning curve of voxels in the SRA ROI, we employed the population Receptive Field (pRF) approach [217]. The population response was modeled as a one-dimensional Gaussian function, defined over log-scaled frequency [227]. The center frequency f_0 spanned the whole range of frequencies played during stimulation, from 100 Hz to 6400 Hz, covering an interval of 6 octaves, with a step size of 0.25 octaves. The values of the standard deviation σ ranged from 0.25 to 4 octaves, with 0.25 octaves step size. The expected response for a population whose tuning is described by one of the Gaussian functions is computed by evaluating the Gaussian curve at the frequency played at each time point. Models were fitted to the data via linear regression, after cleaning out the contribution of nuisance variables (i.e., drifts and head motion), and the tuning for each voxel was determined by selecting the combination of f_0 and σ that maximizes the t-score of the fit, that is

β/SE where β is the coefficient of the linear regression and SE is the standard error of the fit. For fQSM data, we selected the Gaussian function that provided the maximum negative t-score, as one should expect the fQSM activation to be sign-flipped as compared to conventional fMRI. The similarity of pRF maps obtained from fMRI and fQSM for each subject was quantified using Pearson's correlation. Statistical significance of the correlation coefficient was evaluated via permutation testing.

5.3.10 Multivariate pattern analysis

To evaluate the response pattern of SRA and to assess the ability of this region in discriminating pure tones based on their frequency, we employed RSA [218]. We conducted this analysis in an ROI defined as the intersection between fMRI and fQSM SRA masks, which identifies task-selective voxels regardless of the technique. For both fMRI and fQSM and for each subject, we obtained Representational Dissimilarity Matrices (RDM) by computing the pairwise correlation distance between tone-specific activity patterns. The correspondence between the fMRI and fQSM RDMs was tested through Pearson's correlation coefficient and statistical significance was assessed via permutation testing. Specifically, in each iteration, stimulus labels of fQSM trials were shuffled thus to obtain a null RDM, which was correlated with the one coming from conventional fMRI. This procedure generated a null distribution (10^5 permutations), which was used to test the significance of the actual correlation value. Lastly, to visualize the functional mapping of pure tones in the SRA region obtained from fMRI and fQSM data, we performed Multidimensional Scaling (MDS; *mdscale* function in MATLAB). Both single-subject and group-average RDMs were visualized in a two-dimensional MDS space. Analyses performed in this study are summarized in Figure 5.1B.

5.4 Results

5.4.1 Data quality and phase artifacts

All subjects involved in the study completed the exam session. However, two of them (M-28yo, F-27yo) reported having fallen asleep during the scan. Moreover, the analysis of motion parameters revealed extreme head motion for another subject (M-32yo): nearly 30% of total timepoints (up to 78% in one of the four runs) were corrupted by excessive framewise displacement (> 0.3 mm). These three subjects were not included in further analyses.

An exemplary fQSM image obtained from the 2D-EPI acquisition by applying the optimized background phase removal workflow [223] is shown in Figure 5.2B, together with the corresponding T2*-weighted image (Figure 5.2A). The across-slices phase-inconsistency artifact also reported in previous fQSM studies [110,113] was removed. Figure 5.2C shows fMRI and fQSM activity of a voxel located in the auditory cortex for a single functional run. Instead, Figure 5.2D depicts the peristimulus plots computed in a voxel showing positive fMRI and negative fQSM responses.

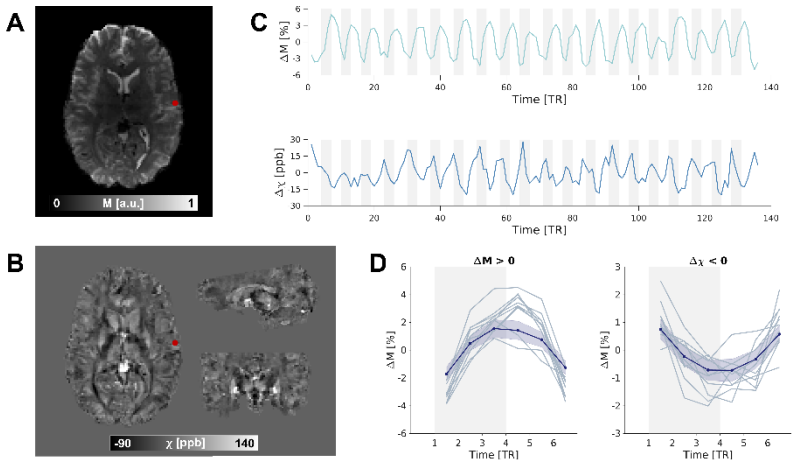

Figure 5.2: fMRI and fQSM data. In panel A, an exemplary T2*-weighted image obtained with EPI is presented, while panel B shows the corresponding QSM image obtained from the phase of the same acquisition. The optimized joint 2D-3D background field removal enables the reconstruction of susceptibility maps from 2D EPI with no phase inconsistencies across slices. Panel C shows the time course during one run of one exemplary voxel in SRA, indicated by the red dot in panel A and B, for fMRI (top) and fQSM (bottom) signal. The gray shaded area indicates stimulus presentation. In panel D we reported the average peristimulus plot for a voxel with positive fMRI and negative fQSM response (blue line, the shaded area indicates the standard error). The gray lines represent the peristimulus plot for an individual trial of each band for a representative subject. The gray shaded area indicates the stimulus period, lasting 3 TRs, that is 7.5 seconds.

5.4.2 GLM analysis and tone-responsive areas

Results of the *All Sounds* > *Rest* contrast showed that the average R^2 peak across subjects in PAC was 0.7 ± 0.1 for fMRI and 0.4 ± 0.1 for fQSM (systematically lower in fQSM than fMRI; $p < 10^{-6}$ in a paired t-test). Also, R^2 maps obtained from fMRI and fQSM data were significantly correlated (Pearson's correlation coefficient was 0.434, $p < 0.001$; Figure 5.3A). A linear fit yielded an angular coefficient of 0.17 (R^2 = 0.19),

indicating that the variance of fMRI data explained by the model is higher than for fQSM data (Figure 5.3A). Further, the average maximum signal increment observed for magnitude EPI during the task was 9 ± 1%. For fQSM, the maximum decrease in susceptibility was -47 ± 14 ppb, ranging from -79 ppb to -35 ppb depending on the subject. Maximum positive fQSM response was 39 ± 14 ppb. At the statistical significance threshold chosen in the current study, the minimum detectable variation of susceptibility ranged from -0.006 ppb to -0.9 ppb depending on the subject, with a median of -0.023 ppb.

The contrast All Sounds > Rest is shown in Figure 5.4 for fMRI and fQSM on the reconstructed cortical surface of each subject.

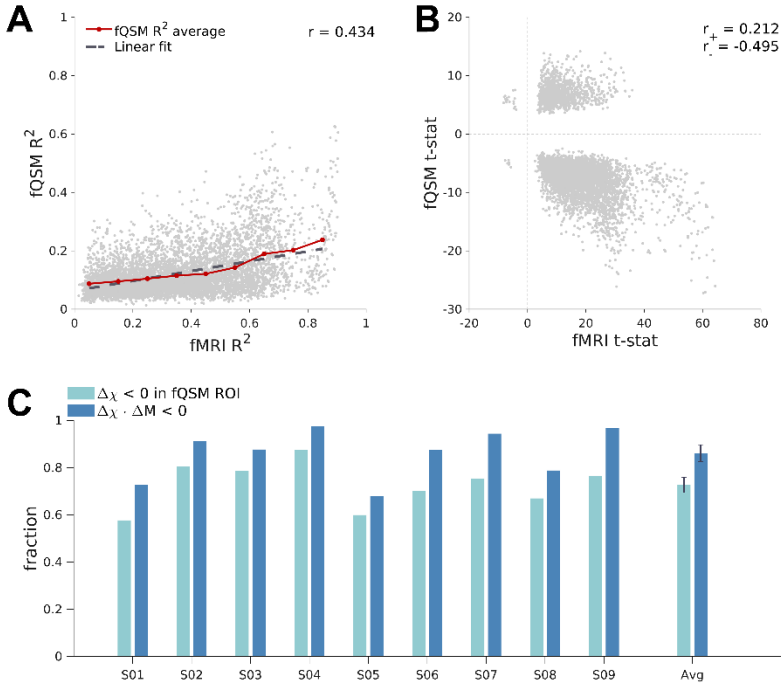

Figure 5.3: fMRI and fQSM responses from GLM analysis. Scatter plot showing the relationship between fMRI and fQSM R^2 values (panel A) of voxels that are

identified as tone-responsive ($p < 0.05$ voxelwise corrected) by both techniques, for all subjects. The red line indicates the average fQSM R^2 over 0.1-wide fMRI R^2 intervals and the result of the linear fit is displayed as a gray dashed line. We reported Pearson's correlation coefficient $r = 0.434$ ($p < 0.001$) and an angular coefficient of 0.17 from the linear fit ($R^2 = 0.19$). In panel B, the scatter plot shows the fQSM t-stat values corresponding to fMRI t-stat values. For voxels with responses of opposite sign we reported Pearson's correlation coefficient $r_- = -0.495$ ($p < 0.001$), while $r_+ = 0.212$ ($p < 0.001$) was found for voxels with responses with the same sign. Panel C displays the fraction of voxels showing negative fQSM response in the SRA ROI defined by fQSM (light blue) and voxels showing opposite response with respect to fMRI in shared tone-responsive areas (dark blue). The error bars indicate the standard error of the mean.

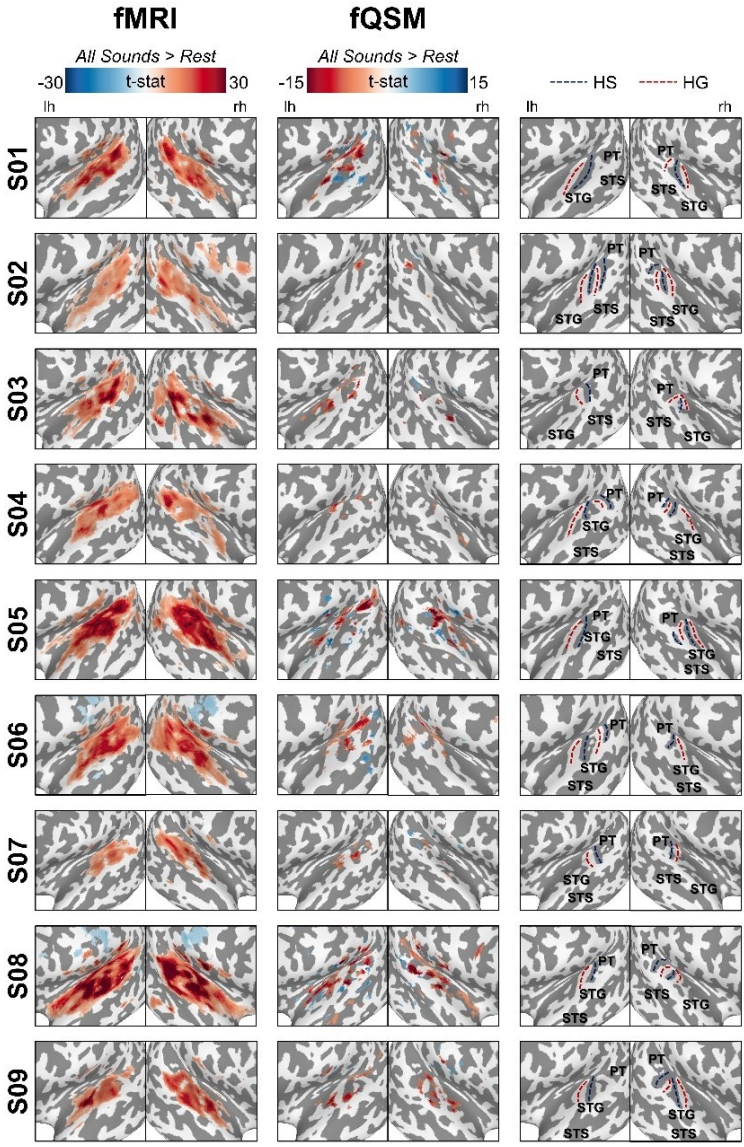

Figure 5.4: Activation maps overlaid onto the inflated cortical surface mesh of each subject. The first two columns display the t-statistics obtained for each

subject by summing the response to all stimulus trials in the SRA ROI identified via non-parametric permutation test ($p < 0.05$ voxelwise corrected), for fMRI and fQSM respectively. The colormaps corresponding to fMRI and fQSM are inverted to take the sign inversion of the response into account and allow a more direct comparison. The third column reports the anatomical landmarks of interest: Superior Temporal Sulcus (STS), Superior Temporal Gyrus (STG), Planum Temporale (PT) and Heschl's Sulcus (HS, blue line) and Gyrus (HG, red line).

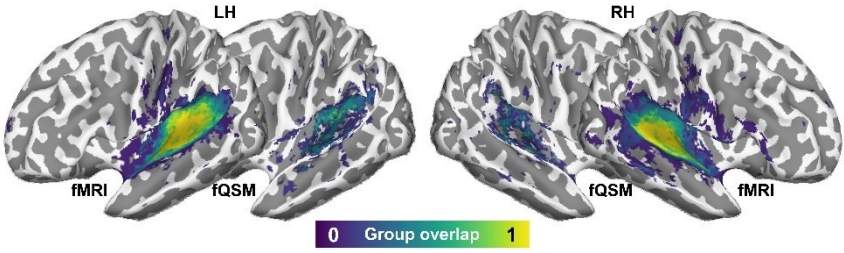

Figure 5.5: Probabilistic SRA ROIs obtained by computing the overlap in the MNI space of the SRA masks of all subjects. The ROI computed via fQSM was smaller and showed less inter-subject overlap than the fMRI ROI.

The probabilistic SRA ROI projected onto a group level MNI cortical mesh is shown in Figure 5.5. The tone-responsive areas identified by the two techniques differed in size, with the fQSM ROI being approximately 15 ± 9 % of the SRA ROI defined by fMRI. Also, the definition of SRA using fQSM data had higher inter-subject variability. Moreover, differently from fMRI results, voxels in these regions showed both increments and decrements in susceptibility (Figure 5.3B). For voxels with responses of opposite sign in fMRI and fQSM, we reported significant Pearson's correlation $r_- = -0.495$ ($p < 0.001$) between t-stats values, while $r_+ = 0.212$ ($p < 0.001$) was found for voxels with responses with the same sign. The fraction of voxels yielding a positive fQSM response was 27 ± 10 % in the SRA ROI defined by fQSM. This ratio dropped to 14 ± 10 % when we considered "unexpected" voxels in the

overlap between the tone-responsive areas of fMRI and fQSM (Figure 5.3C).

Voxels belonging to White Matter (WM) and Gray Matter (GM) were studied separately according to the segmentation of the anatomical image with a probability threshold of 0.5. The fraction of active voxels belonging to gray matter structures was 65 ± 4 % for fMRI and 73 ± 8 % for fQSM (Figure 5.6A). This statistically significant difference ($p < 0.01$ in a Wilcoxon signed rank test) indicates that fQSM provides patterns of activation that are more spatially specific than the one obtained via fMRI. We reported that the fraction of voxels with fQSM response of opposite sign with respect to fMRI was higher in GM than in WM. In fact, while in GM the fraction of voxels with "unexpected" fQSM response was 12 %, in WM it was 42 % (Figure 5.6B). The anatomical localization of active voxels can be also indicated by their structural tissue susceptibility, as measured by the fQSM time average. Figure 5.6C shows the relationship between the average susceptibility of tone-responsive voxels and the sign and magnitude of its response. Negative fQSM responses generally yielded a higher R^2 value with respect to positive fQSM. The median of the tissue susceptibility distribution in an fQSM t-stat interval shifts towards negative values when fQSM response becomes positive (Figure 5.6D). As negative values in QSM indicate the presence of a diamagnetic source, such as myelin, they are typically found in WM structures, whereas positive χ values in GM. Thus, fQSM activation of the same sign as fMRI were mostly located in WM, while in GM the expectations on fQSM behavior were met in the great majority of voxels.

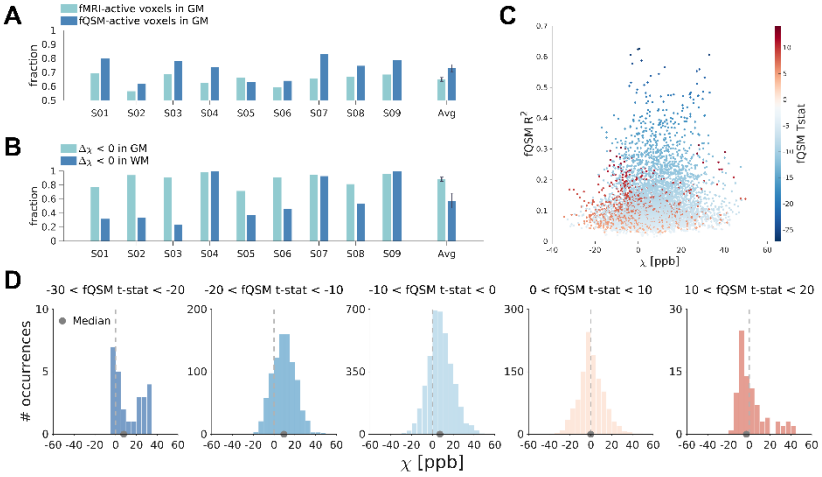

Figure 5.6: Anatomical distribution of active voxels. The fraction of voxels that belong to gray matter structures and show a significant response at the statistical threshold selected in this study was higher in fQSM (dark blue) than in fMRI (light blue) (Panel A), indicating that fQSM yields higher spatial selectivity than fMRI. The error bars indicate the standard error of the mean. Panel B shows the fraction of voxels with negative fQSM response in gray matter (light blue) and white matter (dark blue) for each subject and averaged over the whole group, highlighting that voxels with positive fQSM response were mostly found in white matter. Panel C displays in a scatter plot the relationship between fQSM R^2 values and the structural tissue susceptibility χ for all subjects. The colors of the dots represent the magnitude of fQSM response. Panel D shows the data plotted in panel C after dividing the values of the t-statistics into five intervals. The colors of the histogram bars represent the intensity of the fQSM response, while the gray dot indicates the median of the distribution. It can be seen that the median susceptibility shifts towards negative values when the response becomes positive. This suggests that the voxels showing positive responses were mainly located in white matter.

5.4.3 Comparison of tonotopic mapping

Regions in SRA that responded preferentially to lower and higher frequencies according to GLM analyses are displayed in the first two columns of Figure 5.7. In fMRI data, 34 ± 16 % of voxels were selective

for higher frequencies, whereas in fQSM this fraction was significantly higher ($p < 0.05$ in a paired t-test), reaching 52 ± 3 % and yielding more balanced GLM contrast maps. We obtained the fine-grained mapping of the frequency tuning of SRA voxels for both fMRI and fQSM data (third and fourth columns in Figure 5.7, respectively). Even though the maps obtained from fMRI data were smoother, fQSM frequency tuning maps showed the expected rostro-caudal high-low-high organization. Also, this arrangement extended to areas that did not reach significance for fQSM at the threshold selected in this study. The similarity between results obtained via fMRI and fQSM was also testified by the significant correlation between the pRF patterns ($p < 0.001$ for each individual; across-subjects average $r = 0.22 \pm 0.11$).

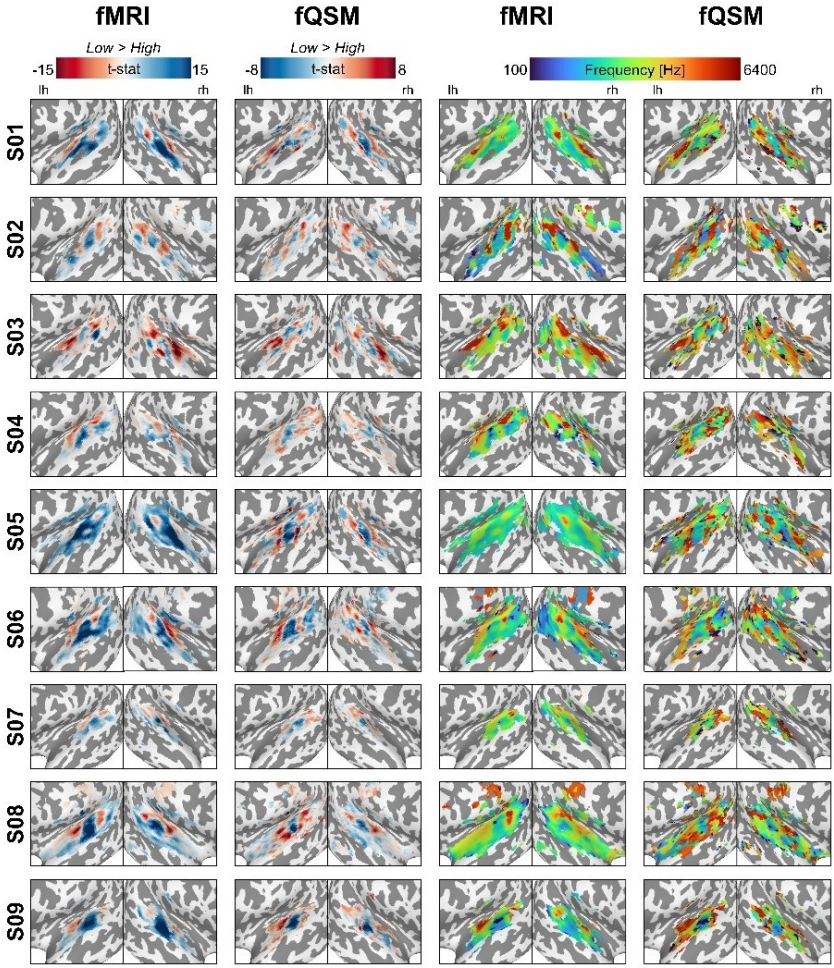

Figure 5.7: GLM-contrast and pRF maps. The first two columns display the areas in SRA ROI that responded preferentially to low frequencies belonging to the first three frequency bands (100-630 Hz) with respect to the high frequencies from the last three bands (2700-6400 Hz), for fMRI and fQSM respectively. The colormaps corresponding to fMRI and fQSM are inverted to take the sign inversion of the response into account and allow a more direct comparison, so that low and high frequencies are consistently represented in blue and red respectively. The third and fourth columns show the results of the pRF approach

for each subject for fMRI and fQSM respectively. The maps obtained by fMRI were smoother but a comparable pattern of frequency tuning preference was retrieved also for fQSM.

5.4.4 Similarity of activation patterns

The group average RDMs obtained from both fMRI and fQSM data are shown in Figure 5.8A. Single-subject RDMs are reported in Supplementary Figure S5.2. RSA analysis revealed significant correspondence between the RDMs obtained from the two approaches ($r = 0.72$ for the group average, 0.49 ± 0.15 for individual subjects, $p < 10^{-5}$).

The results of the MDS analysis are shown for the group-average RDMs and for two representative subjects in Figure 5.8B. The scatter plots for each individual subject are reported in Supplementary Figure S5.3. The MDS analysis on the group-average RDMs, as well as the results on the single subject, showed that trials of the same stimulus condition were clustered together along the first dimension for both fMRI and fQSM. As shown in Supplementary Figure S5.4, the second dimension highlighted two clearly distinguished clusters corresponding to the trials belonging to EPI runs with opposite polarities. Despite being noisier than fMRI, the activation patterns in fQSM retained enough information to enable the mapping of a fine-grained, topographically-arranged organization of SRA.

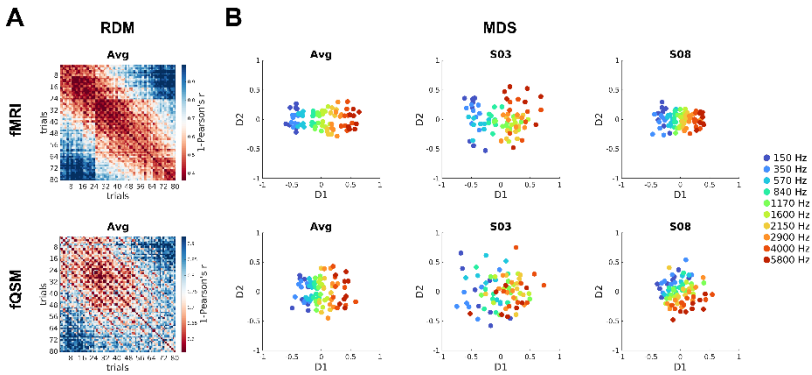

Figure 5.8: RDMs and the results of MDS analysis. Panel A shows the group average RDMs computed via the correlation distance between activation patterns in SRA ROI for fMRI (top) and fQSM (bottom). In panel B, the scatter plots representing in a 2-dimensional MDS space the group-average RDMs and the RDMs of two representative subjects are displayed. The first row refers to fMRI results while the second corresponds to fQSM. The colors represent the central frequency of the band of each trial. The activation patterns of trials corresponding to the same stimulus condition clustered along the first MDS dimension.

5.5 Discussion

In the current study, we acquired a complex-valued 2D-EPI dataset in a sample of healthy subjects using a 7T MRI scanner to assess the usefulness of fQSM in up-to-date human neuroimaging research. We particularly focused on the evaluation of fQSM spatial specificity and on the characterization of its sensitivity in discriminating patterns of activation associated with different stimulus conditions.

We report that, in fQSM data, voxels significantly activated by listening to pure tones are less numerous, but also more likely located in the gray matter, than above-threshold voxels identified using canonical fMRI. This suggests that the lower sensitivity of fQSM is, indeed, paralleled by higher spatial specificity. Interestingly, “unexpected” positive fQSM

activations are mainly limited to white matter. Moreover, both univariate GLM and pRF analyses provide similar results when comparing the two acquisition methods. Nevertheless, while maps obtained from fMRI are smoother in their spatial distribution, those coming from fQSM show a patchier organization and voxel tunings are more equally represented across the whole frequency range. This evidence is - again - in favor of the higher specificity of fQSM in capturing fine spatial variations related to the functional architecture of tone selective brain areas. Lastly, the representational similarity analysis highlights a significant correlation between patterns of brain activity derived from fQSM and canonical fMRI data.

In light of all this, our findings indicate that when univariate and multivariate methods are applied to fQSM data, they provide biologically plausible results and that fQSM and canonical fMRI data complement each other in the study of brain activity.

In agreement with previous studies [95,110–115], when the same statistical threshold is applied, the extent of tone-responsive areas identified by fQSM is five- to ten-fold smaller as compared to the one identified by fMRI. However, fQSM is sufficiently sensitive to detect significant variation of susceptibility in the order of -0.01 ppb, that is two orders of magnitude lower than what expected for pial veins [110]. This suggests its capability of revealing not only strong sources of susceptibility variation, such as big vessels that yield a signal alteration in the order of -10 ppb, but also weak activations in the parenchyma. Also, fQSM activation maps have a significantly greater fraction of voxels lying in gray matter tissues than fMRI, which we interpreted as a clue of higher spatial specificity. This is built on the assumption that brain activity should be typically observed in gray matter rather than white matter. By testing the spatial distribution of active voxels at different statistical thresholds, we reported higher specificity of fQSM for activations in gray matter for the majority of subjects, as described in Supplementary Materials and Supplementary Figure S5.5. However, a conclusive proof of this statement would require a ground truth measurement for tonotopic mapping. The higher spatial specificity of

fQSM can be explained by the deconvolution of the dipole kernel performed during QSM reconstruction and the subsequent removal of the non-local effect. Indeed, in conventional fMRI the perturbation of the magnitude signal extends to voxels surrounding the foci of the neural activation, hindering the accurate mapping of the true activation site [1]. Notably, the increased spatial specificity is not canceled by the small amount of spatial smoothing that was applied to the data, suggesting that the non-local dipole effect acts on a larger-scale distance. On the other hand, spatial smoothing allowed direct comparison with fMRI data and increased statistical robustness [228]. In addition, the analysis repeated with no spatial blurring applied yielded analogous results, indicating that activation pattern can be retrieved by fQSM data even in the absence of smoothing, as shown in Supplementary Figure S5.6.

Despite negative fQSM responses are expected to colocalize with positive fMRI activation, previous studies [110,112–114] reported sign inversion of the fQSM activity, that is voxels whose susceptibility time series showed significant positive correlation with stimulus presentation, just as the corresponding fMRI time series. This was especially observed in regions close to strong susceptibility sources such as large veins [113], suggesting that in these areas the QSM reconstruction step failed in completely removing the non-local field components [110,113]. On the other hand, positive fQSM was reported for several reconstruction methods, analysis approaches and acquisition parameters, indicating that it may underlie some physiological information. In this work, we observed the same effect and attempted to characterize its biophysical properties. Specifically, we characterized the anatomical substrate underlying these observations by labeling each activated voxel as belonging to gray or white matter, so as to test whether "unexpected" fQSM activations depended on the underlying anatomical structure. The labeling operation was performed based both on the tissue class segmentation obtained from the T1-weighted anatomical image and on the time-average susceptibility value of each voxel. We reported that the voxels showing positive fQSM activation were mainly located in white matter, while in gray matter more than 90% of voxels display the expected behavior. In fact, in our data, GLM contrasts were minimally

affected by unexpected fQSM responses. Instead, the interpretation of activations in white matter is not trivial, even for conventional fMRI, and represents an open question in neuroscience [229]. It is acknowledged that the conventional fMRI models may not be suitable to detect white matter task-specific activations [230] and that the lower density of vessels reported in white matter reduces the contribution of cerebral blood flow and volume to the fMRI signal [229]. Moreover, the anisotropic vascular architecture in white matter affects the GRE signal, i.e., the apparent R2* and magnetic susceptibility, as well as cerebral blood flow and volume, whose measured values depend on the orientation of vessels with respect to the static magnetic field B_0 [231]. Hence, the mismatch between fMRI and fQSM and its prevalence in white matter may be related to artifacts or it may be due to the detection of different contributions to the signal which could be interpreted by developing improved biophysical modeling, as the well-established model adopted for the cerebral cortex might be inadequate. Even though our characterization suggests that morphological properties of brain tissues are implicated in the generation of positive fQSM responses, further investigations are needed to clarify its underlying mechanisms.

On these premises, we compared fQSM and fMRI responses to different stimulus conditions, that is to different sound frequencies, using both univariate and multivariate methods. The "Low > High frequency" GLM map revealed the expected rostro-caudal high-low-high functional organization in SRA [227,232–237]. The morphological, functional and topographical organization of the human auditory cortex is highly variable [227,237–239] and both fMRI and fQSM maps displayed high inter-subject and inter-hemispheric variability. Voxels selective for higher frequencies were significantly more represented in fQSM-based maps than in the corresponding fMRI data, leading to more balanced GLM contrast maps. Accordingly, the pRF method yielded fine-grained frequency-tuning maps that were similar for fQSM and fMRI, as testified by Pearson's correlation coefficient. The smoother appearance of fMRI tonotopic maps may relate to the intrinsic blurring of the magnitude signal due to dipole effect, or to the higher noise level in fQSM. A test-retest analysis performed by splitting the data into two halves proved

the reproducibility of fQSM responses. In addition, the stability of the pRF estimates of frequency tuning was demonstrated by performing the fitting operation on a partition of the data and testing its reliability on the remaining part. Test-retest reproducibility was lower in fQSM with respect to fMRI and stable fQSM response was reported in a smaller fraction of voxels, likely due to the different sensitivity and specificity of the two techniques. Nonetheless, the high-low-high frequency tuning pattern was successfully retrieved. These analyses are described in the Supplementary Materials and shown in Supplementary Figures S5.7 and S5.8.

Multivoxel pattern analysis confirmed the correspondence between fMRI and fQSM information. For each technique, we obtained RDMs from patterns of activation corresponding to each stimulus trial and attested their similarity via RSA. Non-metric multidimensional scaling was employed to reduce matrix dimensionality and unveil RDMs structure. In both cases, the trials clustered along the first MDS dimension based on their frequency. Hence, similarly to fMRI, fQSM captures variations in brain activity associated with the processing of perceptual features. Unexpectedly, despite the correction for susceptibility-induced geometric distortions, the second dimension distinguished between trials belonging to acquisition runs with opposite phase-encoding polarities, which then left a trace in the response pattern of both techniques.

One interesting application that fQSM might find in neuroscience research concerns the study of cortical columnar- or layer-specific activation via sub-millimetric fMRI acquisitions, as the spatial accuracy of activity localization would be a powerful tool in disclosing small-scale functional differentiation and architecture. However, in order to enable such application, future studies should test whether fQSM sensitivity is sufficient to detect brain activity using sub-millimetric spatial resolution and no spatial smoothing. In this case, one limitation would be represented by the small brain coverage, which would disrupt fQSM quantification accuracy. In fact, QSM values are affected by partial coverage of the brain, especially in slices near the boundaries [89,90],

even though deep learning approaches may mitigate this issue [240]. In this study, we did not reach whole-brain coverage but the cortical areas of interest (i.e., SRA) are far from the borders of the acquired volume. Other factors affecting susceptibility quantification concern the choice of voxel size [90,93], echo time [91,92,116,157], and the orientation of the subject's head with respect to the external magnetic field, due to the tensorial nature of magnetic susceptibility [78]. However, this does not represent a confounding factor in gray matter, as susceptibility anisotropy in the brain is mainly related to the highly ordered microstructure of myelin sheath [28,77,78,156]. Further studies are needed to assess the accuracy of quantification of dynamic variations in tissue oxygenation obtained from fQSM.

In the current study, the use of an optimized pipeline for the processing of the phase of 2D-EPI data enabled the reconstruction of susceptibility maps devoid of phase inconsistency artifacts, reported in previous works [110,113]. The following functional processing pipeline was derived from the canonical workflow for fMRI with some minor adjustments: spatial transformations were computed on the magnitude images and then applied to susceptibility maps and sign inversion of fQSM time series with respect to fMRI signal was taken into account when computing statistics and when fitting pRF models.

One limitation of this study is related to the lack of a ground truth for non-invasive *in vivo* brain functional mapping, as magnitude-based fMRI only represents a surrogate of neural activation with well-known limits concerning spatial specificity. As for the studies on the neurophysiological correlates of BOLD activations [241], simultaneous recording of fQSM data and local field potentials or multi-unit spiking activity are needed to address this issue. Also, activations obtained from fQSM and spin-echo (SE) fMRI should be compared, as SE-EPI are characterized by higher spatial accuracy [242].

While the relatively small sample size included in the current study could be considered a limitation, the results were obtained at single-subject level. Moreover, the high across-participants consistency of

results for a wide range of analyses further corroborates the reliability of findings.

In conclusion, fQSM produces activation maps that are complementary to those obtained from conventional fMRI, as they seem to be characterized by a higher spatial specificity, though further studies comparing fQSM activation maps to ground truth measurement are needed. Not only have we been able to produce fine-grained tonotopic maps using univariate methods, but we also demonstrated that multivariate techniques can be applied to fQSM activity to access brain regional information content. Importantly, because fQSM is quantitative, information obtained at different scanning sites may be compared, thus providing a valuable, novel and cost-effective tool for pooling together data from different studies, including longitudinal as well as consortium and multicentric research and clinical projects. Of note, our results indicate that positive fQSM responses do not affect the interpretation of activations or contrasts of interest. Lastly, thanks to its higher spatial specificity, fQSM can detect brain activity more precisely, providing finer functional cerebral maps for brain surgery planning, as well as for other clinical investigations.

Supplementary Figures

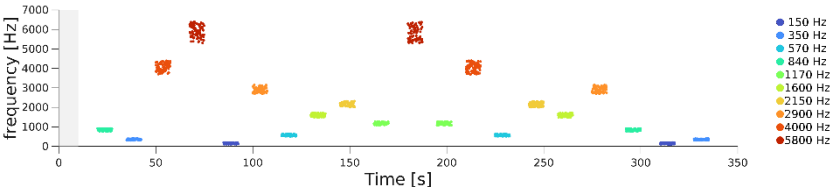

Figure S5.1: Schematic representation of the auditory stimulus played in one functional scan. Each dot represents a single pure tone, while different colors depict different frequency bands, whose central frequencies are reported in the legend. The gray shaded area indicates dummy volumes.

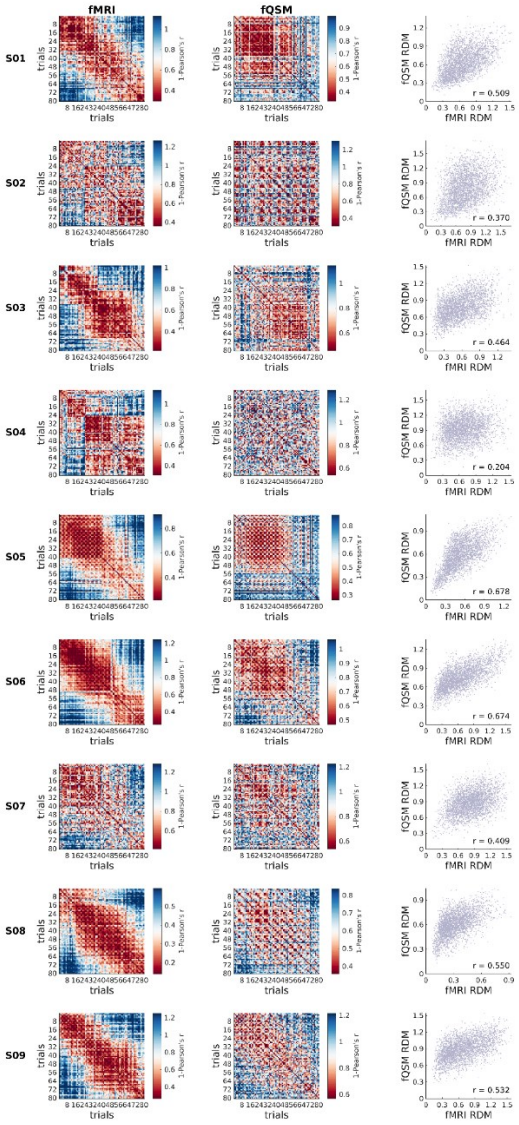

Figure S5.2: Single-subject RDMs computed via the correlation distance between activation patterns in PAC ROI for fMRI (top) and fQSM (bottom).

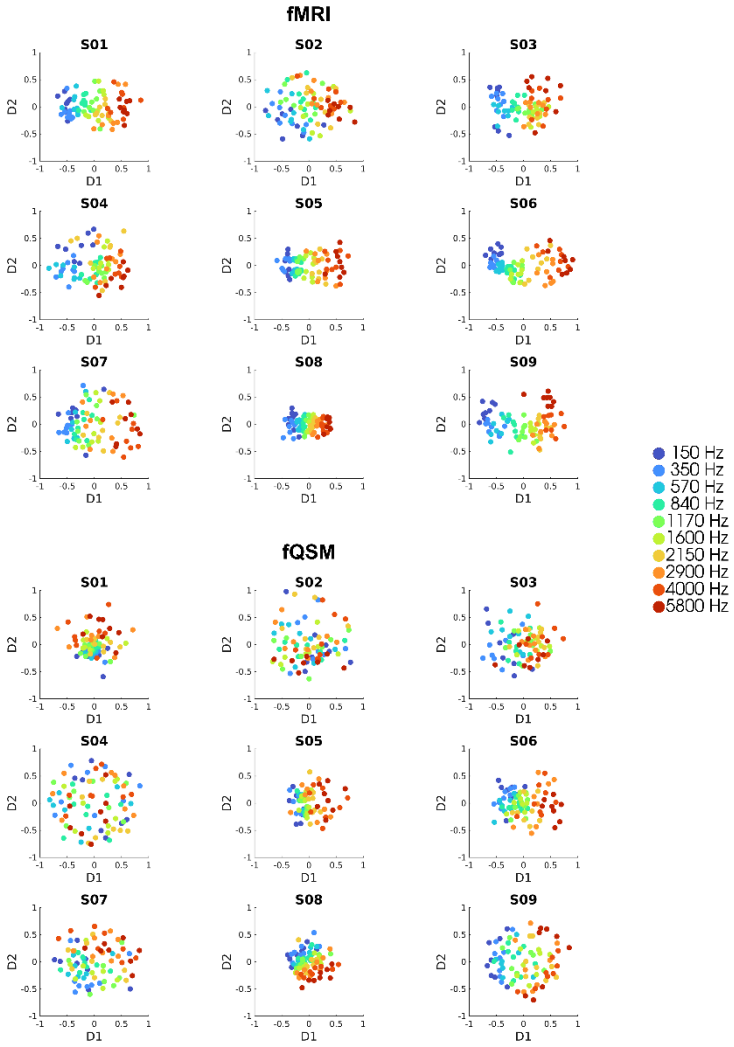

Figure S5.3: Scatter plots representing the single-subject RDMs in a 2-dimensional MDS space. The top panel refers to fMRI results while the bottom one corresponds to fQSM. The colors represent the central frequency of the band of each trial. The activation patterns of trials corresponding to the same stimulus condition clusters along the first MDS dimension.

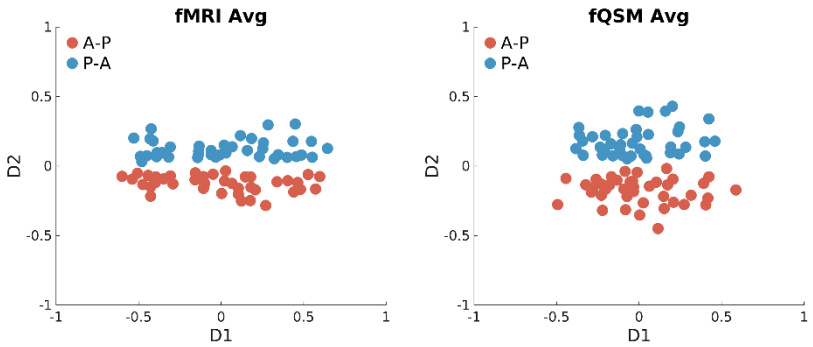

Figure S5.4: Scatter plots representing the RDMs in a 2-dimensional MDS space. The plot on the left refers to fMRI results while the one on the right corresponds to fQSM. The colors represent odd and even runs, which were acquired with opposite phase-encoding polarities.

Evaluation of spatial specificity

The evaluation of spatial detection accuracy is not straightforward, as no ground truth measurement is available. To provide a quantitative value for the accuracy assessment, the analysis reported in Figure 5.6A concerning the spatial distribution of fQSM activation was extended to multiple statistical thresholds. We assumed that during auditory stimulation all gray matter voxels in Heschl's gyrus should be detected as active voxels, while white matter voxels could be assumed to be non-active, based on the assumption that brain activity should be typically observed in gray matter rather than in white matter. An ROI of Heschl's gyrus was defined by thresholding the probabilistic ROI from the Harvard-Oxford Cortical Structural atlas to a probability of 0.1. Voxels were assigned to either white or gray matter based on single-subject tissue class segmentation. Afterward, we selected the voxels whose t-statistics was above a variable percentile threshold and defined active voxels in gray matter as true positives, non-active voxels in gray matter

as false negatives, active and non-active voxels in white matter as false positives and true negatives, respectively. The ROC curves in Figure S5.5 show that, given a sensitivity level, fQSM had higher specificity than fMRI in six out of nine subjects. In two subjects (S02 and S06) the curves overlap and in one subject (S05) the fQSM curve lies slightly below the fMRI one. While this test does not represent a conclusive proof, which would instead require a ground truth measurement of tonotopic mapping, it provides supporting evidence for the higher spatial specificity of fQSM.

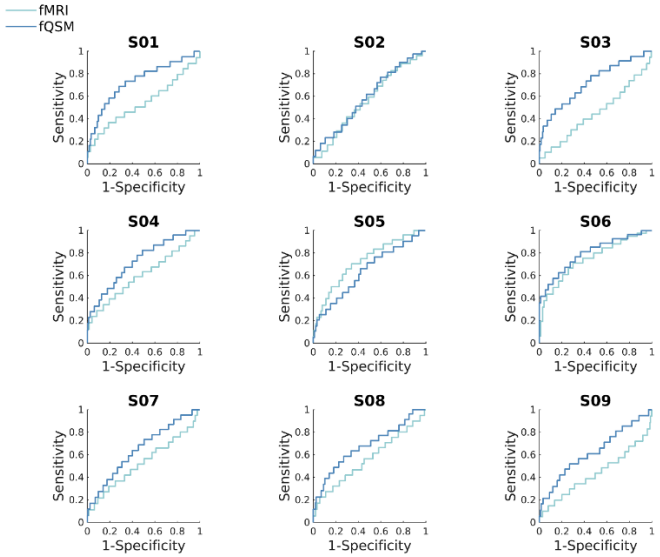

Figure S5.5: Single-subject ROC curves showing the sensitivity and the specificity of fQSM and fMRI in detecting brain activity in gray matter voxels, rather than in white matter.

Analysis with no spatial smoothing

The analysis was repeated with no spatial smoothing applied. Figure S5.6 displays the results of the RSA analysis for one exemplary subject

(S01). The RDMs show that the correlation distances between patterns were higher with respect to the ones obtained using smoothed data but the general structure of the matrix was preserved, leading to significant correlation between fMRI and fQSM (r = 0.91 for the group average, 0.78 ± 0.11 for individual subjects, p < 10-5). As the blurring operation may partially hide the response patterns, the correlation values yielded by RSA are higher when no smoothing is applied.

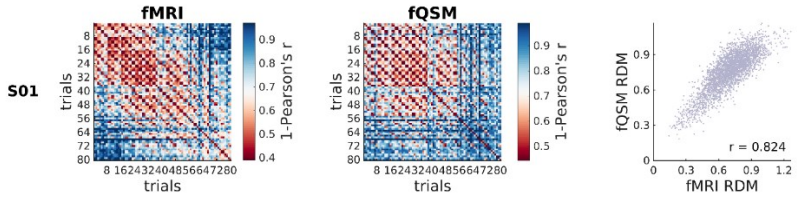

Figure S5.6: RDMs computed via the correlation distance between activation patterns in SRA ROI with no spatial smoothing applied for fMRI (left) and fQSM (center), for a representative subject (S01). The scatter plot (right) highlights the correlation between the RDMs obtained with the two methods.

Test-retest analysis

To assess fQSM reproducibility, a test-retest evaluation was performed by splitting the whole experiment into two parts, specifically by comparing the results of GLM analysis performed on the first and second runs and, separately, on the third and fourth runs. Pearson's correlation coefficient was calculated considering the t-statistics of the All sounds > Rest contrast in an anatomically defined probabilistic ROI of Heschl's gyrus from the Harvard-Oxford Cortical Structural atlas. The ROI was thresholded to a probability of 0.1. The correlation analysis yielded an across-subject average r = 0.91 ± 0.04 (p < 0.001) for conventional fMRI and r = 0.67 ± 0.14 (p < 0.001) for fQSM. Even though the reproducibility of fQSM is lower than that of fMRI, the results are significantly stable, even when obtained with half of the data used in this study for the other analyses.

Reliability of pRF estimates

The pRF maps in Figure 5.7 show the frequency tuning in the whole SRA. Here we report the frequency tuning map obtained for a representative subject (S01) considering only the voxels fitted by the pRF model with $p < 0.01$, which corresponds to a Pearson's correlation between the predicted and actual response above 0.11. Figure S5.7 shows that the tonotopic organization of the auditory cortex can be reliably retrieved via fQSM.

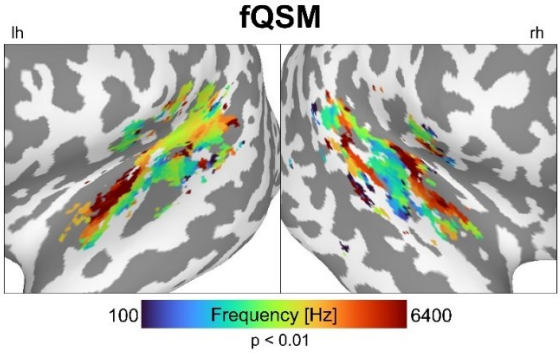

Figure S5.7: Results of the pRF mapping for a representative subject (S01) using fQSM, after applying a statistical threshold of $p < 0.001$ (Pearson's $r > 0.11$), showing the pattern of frequency tuning preference.

To evaluate the reliability and the stability of pRF parameters estimation, we partitioned the data, computed pRF fitting using the first three runs and tested the fit of the parameters on the fourth run. Panel A in Figure S5.8 shows the value of the Pearson's correlation coefficient in each voxel for fMRI and fQSM. Even though correlation values were generally lower in fQSM than in fMRI and a stable fQSM response was reported in a smaller fraction of voxels with respect to fMRI in the considered ROI, voxels passing the $p < 0.01$ threshold demonstrate the typical high-low-high frequency tuning pattern (Figure S5.8, panel B).

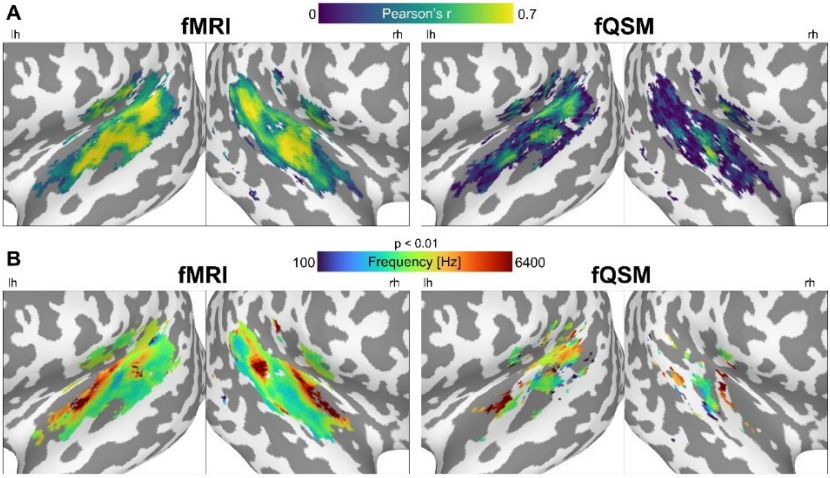

Figure S5.8: Stability of pRF parameters estimation. Panel A shows the Pearson's r obtained by correlating the time series of the fourth run and the predicted time series computed using the parameters fitted on the first three runs, for a representative subject (S01). Panel B displays the tonotopic organization retrieved considering voxels with Pearson's $r > 0.11$ ($p < 0.01$).

Chapter 6 Final remarks and outlook

This thesis focused on the assessment of potentials and pitfalls of Quantitative Susceptibility Mapping and on the application of this technique to both clinical and fundamental research questions. In the last few years, the histological validation of the correlation of QSM measurements to fundamental biomarkers, such as iron load and myelination, favored new clinical applications, especially concerning the study of neurodegenerative disorders. Moreover, the use of QSM in the study of brain function was recently suggested to obtain quantitative and spatially specific information on neural activity.

A fundamental requirement for a quantitative technique is its reproducibility and its transferability across scanners. For this reason, it is crucial to assess to what extent some acquisition parameters may impair χ measurements. In this work, we focused on the impact of echo time on QSM reproducibility (Chapter 2), assessed on a group of healthy controls that were scanned multiple times, and its diagnostic power, tested in a cohort of patients with Multiple System Atrophy (Chapter 3). In this study, the potential of histogram analysis in supporting differential diagnosis was also investigated. Afterward, we exploited the information provided by QSM to explore the mechanisms of iron accumulation in a sample of patients with Parkinson's diseases or in its prodromal stages, such as REM sleep behavior disorder (Chapter 4). Finally, we characterized functional QSM performances in tonotopic mapping and compared it to conventional fMRI using both univariate and multivariate methods (Chapter 5).

The first part of this research was motivated by the need to optimize the acquisition parameters for QSM in multi-center studies to ensure reproducibility and enable the translation of ultra-high field MRI results into clinical applications at lower field strength. To this purpose, we acquired susceptibility maps on a group of "traveling heads" on a 7T and a 3T MRI system and focused on the impact of echo time. Provided to keep it fixed across repeated measurements, we confirmed the excellent

repeatability of susceptibility measurements at 3T and, for the first time, assessed it at 7T in-vivo. We achieved high inter-scanner reproducibility by setting the TEs of the 3T and 7T sequences to a specific ratio (Chapter 2). Hence, careful protocol standardization is required in multi-center studies that involve scanners operating at different field strength.

The impact of TE on QSM measurements relates to sub-voxel microstructural organization. As it may be altered by diseases, TE-dependence may vary across populations with different pathological conditions. Using 7T multi-echo GRE images of healthy controls and MSA patients with both cerebellar and Parkinsonian phenotypes, we demonstrated that the choice of TE also affects the diagnostic value of QSM (Chapter 3). We reported iron overload in MSA patients with respect to healthy controls in several deep gray matter nuclei, such as putamen, substantia nigra, globus pallidus, caudate nucleus and dentate nucleus. However, these differences could not be detected irrespective of TE. In fact, susceptibility measured at short TEs provided higher discrimination accuracy between groups than those at longer TEs, as they can capture variations in rapidly-decaying contributions of high χ sources. Thus, a targeted choice of TE can boost QSM performance in the diagnosis and differential diagnosis of neurodegenerative diseases. Moreover, the analysis of histogram features yielded increased diagnostic power, as it can also reveal heterogeneities in the spatial distribution of iron deposition, rather than the overall alterations detected by the ROI mean value. Future studies focusing on radiomics second-order textures and multivoxel pattern analysis may unveil fine-grained textures of iron load and enhance QSM classification power.

Parkinson's disease is one of the main targets of QSM clinical investigations, as it is characterized by a diffuse pattern of iron accumulation, and the identification of presymptomatic biomarkers to support early diagnosis in prodromal stages with no motor symptoms would be crucial. In our study, we created a probabilistic ROI of nigrosome 1 from a group of healthy controls to evaluate iron deposition in PD and iRBD patients at 7T (Chapter 4). We reported iron overload in only PD patients with respect to iRBD and HC. However, we

demonstrated that N1 iron content in iRBD patients increases with disease duration and it may provide information on the mechanisms underlying conversion to α-synucleinopathies. Due to the limited time available for this project, we have not yet been able to observe the conversion in a significant number of patients. Future studies will focus on longitudinal follow-up of iRBD patients to observe how susceptibility of nigrosome 1 is affected by the development of α-synucleinopathies and to identify predictive hallmarks for the onset of motor impairment.

Finally, we applied QSM to the study of brain function as it may address the well-known drawback of conventional fMRI related to the blooming effect, which limits its spatial specificity. The characterization of functional QSM activations was carried out through both univariate and multivariate analysis approaches on a dataset acquired on a 7T MRI system on healthy controls during a stimulation paradigm for tonotopic mapping (Chapter 5). We proved that the lower sensitivity of this technique is compensated by higher spatial specificity. fQSM tonotopic maps obtained via pRF were comparable but more balanced across the whole frequency range of stimulation than those obtained via conventional fMRI. RSA revealed that activation patterns of fQSM and fMRI similarly encode fine-grained frequency information. Hence, fQSM yields complementary information to conventional fMRI, and, thanks to its quantification capability and spatial specificity, it may represent a promising method for multicentric studies and pre-surgical mapping. Future studies should investigate fQSM quantification accuracy and assess the precision of fQSM activation maps by comparing them to ground-truth -yet invasive- techniques.

In conclusion, by assessing its reproducibility and diagnostic accuracy and by characterizing the activation maps produced when applied to functional studies, the work presented in this thesis demonstrated the potential of QSM as a powerful and versatile tool in both clinical and fundamental neuroimaging.

Bibliography

1. Schenck JF. The role of magnetic susceptibility in magnetic resonance imaging: MRI magnetic compatibility of the first and second kinds. Med Phys. 1996;23(6):815–850. doi: 10.1118/1.597854.

2. Haacke E, Reichenbach J. Susceptibility weighted imaging in MRI: basic concepts and clinical applications. John Wiley & Sons; 2014.

3. Schofield MA, Zhu Y. Fast phase unwrapping algorithm for interferometric applications. Opt Lett. 2003;28(14):1194–1196. doi: 10.1364/OL.28.001194.

4. Volkov V V., Zhu Y. Deterministic phase unwrapping in the presence of noise. Opt Lett. The Optical Society; 2003;28(22):2156. doi: 10.1364/ol.28.002156.

5. Bagher-Ebadian H, Jiang Q, Ewing JR. A modified fourier-based phase unwrapping algorithm with an application to MRI venography. J Magn Reson Imaging. NIH Public Access; 2008;27(3):649–652. doi: 10.1002/jmri.21230.

6. Robinson SD, Bredies K, Khabipova D, Dymerska B, Marques JP, Schweser F. An illustrated comparison of processing methods for MR phase imaging and QSM: combining array coil signals and phase unwrapping. NMR Biomed. John Wiley and Sons Ltd; 2017. doi: 10.1002/nbm.3601.

7. Schweser F, Robinson SD, de Rochefort L, Li W, Bredies K. An illustrated comparison of processing methods for phase MRI and QSM: removal of background field contributions from sources outside the region of interest. NMR Biomed. John Wiley and Sons Ltd; 2017. doi: 10.1002/nbm.3604.

8. Schweser F, Deistung A, Lehr BW, Reichenbach JR. Quantitative imaging of intrinsic magnetic tissue properties using MRI signal phase: an approach to in vivo brain iron metabolism? Neuroimage. 2011;54(4):2789–2807. doi: 10.1016/j.neuroimage.2010.10.070.

9. Liu T, Spincemaille P, De Rochefort L, Kressler B, Wang Y. Calculation of susceptibility through multiple orientation sampling (COSMOS): A method for conditioning the inverse problem from measured magnetic field map to susceptibility source image in MRI. Magn Reson Med. John Wiley and Sons Inc; 2009;61(1):196–204. doi: 10.1002/mrm.21828.

10. Shmueli K, de Zwart JA, van Gelderen P, Li T-Q, Dodd SJ, Duyn JH. Magnetic susceptibility mapping of brain tissue in vivo using MRI phase data. Magn Reson Med. Wiley-Blackwell; 2009;62(6):1510–1522. doi: 10.1002/mrm.22135.

11. Wharton S, Schäfer A, Bowtell R. Susceptibility mapping in the human brain using threshold-based k-space division. Magn Reson Med. John Wiley & Sons, Ltd; 2010;63(5):1292–1304. doi: 10.1002/mrm.22334.

12. Li W, Wu B, Liu C. Quantitative susceptibility mapping of human brain reflects spatial variation in tissue composition. Neuroimage. 2011;55(4):1645–1656. doi:

10.1016/j.neuroimage.2010.11.088.

13. Li W, Wang N, Yu F, et al. A method for estimating and removing streaking artifacts in quantitative susceptibility mapping. Neuroimage. 2015;108:111–122. doi: 10.1016/j.neuroimage.2014.12.043.

14. Wei H, Dibb R, Zhou Y, et al. Streaking artifact reduction for quantitative susceptibility mapping of sources with large dynamic range. NMR Biomed. John Wiley and Sons Ltd; 2015;28(10):1294–1303. doi: 10.1002/nbm.3383.

15. Liu J, Liu T, De Rochefort L, et al. Morphology enabled dipole inversion for quantitative susceptibility mapping using structural consistency between the magnitude image and the susceptibility map. Neuroimage. NIH Public Access; 2012;59(3):2560–2568. doi: 10.1016/j.neuroimage.2011.08.082.

16. Liu Z, Spincemaille P, Yao Y, Zhang Y, Wang Y. MEDI+0: Morphology enabled dipole inversion with automatic uniform cerebrospinal fluid zero reference for quantitative susceptibility mapping. Magn Reson Med. John Wiley and Sons Inc; 2018;79(5):2795–2803. doi: 10.1002/mrm.26946.

17. Acosta-Cabronero J, Milovic C, Mattern H, Tejos C, Speck O, Callaghan MF. A robust multi-scale approach to quantitative susceptibility mapping. Neuroimage. 2018;183:7–24. doi: 10.1016/j.neuroimage.2018.07.065.

18. Bollmann S, Rasmussen KGB, Kristensen M, et al. DeepQSM - using deep learning to solve the dipole inversion for quantitative susceptibility mapping. Neuroimage. Academic Press Inc.; 2019;195:373–383. doi: 10.1016/j.neuroimage.2019.03.060.

19. Jung W, Bollmann S, Lee J. Overview of quantitative susceptibility mapping using deep learning: Current status, challenges and opportunities. NMR Biomed. John Wiley and Sons Ltd; 2020; doi: 10.1002/nbm.4292.

20. Schweser F, Deistung A, Lehr BW, Reichenbach JR. Differentiation between diamagnetic and paramagnetic cerebral lesions based on magnetic susceptibility mapping. Med Phys. 2010;37(10):5165–5178. doi: 10.1118/1.3481505.

21. Deistung A, Schäfer A, Schweser F, Biedermann U, Turner R, Reichenbach JR. Toward in vivo histology: A comparison of quantitative susceptibility mapping (QSM) with magnitude-, phase-, and R2*-imaging at ultra-high magnetic field strength. Neuroimage. Academic Press; 2013;65:299–314. doi: 10.1016/J.NEUROIMAGE.2012.09.055.

22. Straub S, Knowles BR, Flassbeck S, Steiger R, Ladd ME, Gizewski ER. Mapping the human brainstem: Brain nuclei and fiber tracts at 3 T and 7 T. NMR Biomed. John Wiley & Sons, Ltd; 2019;32(9):e4118. doi: 10.1002/NBM.4118.

23. Chandran AS, Bynevelt M, Lind CRP. Magnetic resonance imaging of the subthalamic nucleus for deep brain stimulation. J. Neurosurg. American Association of Neurological Surgeons; 2016. p. 96–105. doi: 10.3171/2015.1.JNS142066.

24. Dimov A V., Gupta A, Kopell BH, Wang Y. High-resolution QSM for functional

and structural depiction of subthalamic nuclei in DBS presurgical mapping. J Neurosurg. American Association of Neurological Surgeons; 2019;131(2):360–367. doi: 10.3171/2018.3.JNS172145.

25. Langkammer C, Schweser F, Krebs N, et al. Quantitative susceptibility mapping (QSM) as a means to measure brain iron? A post mortem validation study. Neuroimage. Academic Press; 2012;62(3):1593–1599. doi: 10.1016/J.NEUROIMAGE.2012.05.049.

26. Zheng W, Nichol H, Liu S, Cheng YCN, Haacke EM. Measuring iron in the brain using quantitative susceptibility mapping and X-ray fluorescence imaging. Neuroimage. Neuroimage; 2013;78:68–74. doi: 10.1016/j.neuroimage.2013.04.022.

27. Sun H, Walsh AJ, Lebel RM, et al. Validation of quantitative susceptibility mapping with Perls' iron staining for subcortical gray matter. Neuroimage. Academic Press Inc.; 2015;105:486–492. doi: 10.1016/j.neuroimage.2014.11.010.

28. Liu C, Li W, Johnson GA, Wu B. High-field (9.4T) MRI of brain dysmyelination by quantitative mapping of magnetic susceptibility. Neuroimage. 2011;56(3):930–938. doi: 10.1016/j.neuroimage.2011.02.024.

29. Argyridis I, Li W, Johnson GA, Liu C. Quantitative magnetic susceptibility of the developing mouse brain reveals microstructural changes in the white matter. Neuroimage. 2013;88C:134–142. doi: 10.1016/j.neuroimage.2013.11.026.

30. Lambrecht V, Hanspach J, Hoffmann A, et al. Quantitative susceptibility mapping depicts severe myelin deficit and iron deposition in a transgenic model of multiple system atrophy. Exp Neurol. Academic Press Inc.; 2020;329:113314. doi: 10.1016/j.expneurol.2020.113314.

31. Deh K, Ponath GD, Molvi Z, et al. Magnetic susceptibility increases as diamagnetic molecules breakdown: Myelin digestion during multiple sclerosis lesion formation contributes to increase on QSM. J Magn Reson Imaging. John Wiley and Sons Inc.; 2018;48(5):1281–1287. doi: 10.1002/jmri.25997.

32. Deistung A, Schweser F, Wiestler B, et al. Quantitative Susceptibility Mapping differentiates between blood depositions and calcifications in patients with glioblastoma. PLoS One. 2013;8(3):1–8. doi: 10.1371/journal.pone.0057924.

33. Straub S, Laun FB, Freitag MT, et al. Assessment of Melanin Content and its Influence on Susceptibility Contrast in Melanoma Metastases. Clin Neuroradiol 2019 303. Springer; 2019;30(3):607–614. doi: 10.1007/S00062-019-00816-X.

34. Koch KM, Meier TB, Karr R, Nencka AS, Muftuler LT, McCrea M. Quantitative susceptibility mapping after sports-related concussion. Am J Neuroradiol. American Society of Neuroradiology; 2018;39(7):1215–1221. doi: 10.3174/ajnr.A5692.

35. Chary K, Nissi MJ, Nykänen O, et al. Quantitative susceptibility mapping of the rat brain after traumatic brain injury. NMR Biomed. John Wiley and Sons Ltd; 2021;34(2):e4438. doi: 10.1002/nbm.4438.

36. Ravanfar P, Loi SM, Syeda WT, et al. Systematic Review: Quantitative

Susceptibility Mapping (QSM) of Brain Iron Profile in Neurodegenerative Diseases. Front Neurosci. Frontiers; 2021;15:618435. doi: 10.3389/fnins.2021.618435.

37. Düzel E, Costagli M, Donatelli G, Speck O, Cosottini M. Studying Alzheimer disease, Parkinson disease, and amyotrophic lateral sclerosis with 7-T magnetic resonance. Eur Radiol Exp 2021 51. SpringerOpen; 2021;5(1):1–17. doi: 10.1186/S41747-021-00221-5.

38. Acosta-Cabronero J, Williams GB, Cardenas-Blanco A, Arnold RJ, Lupson V, Nestor PJ. In Vivo Quantitative Susceptibility Mapping (QSM) in Alzheimer's Disease. Connor JR, editor. PLoS One. 2013;8(11):e81093. doi: 10.1371/journal.pone.0081093.

39. Ayton S, Fazlollahi A, Bourgeat P, et al. Cerebral quantitative susceptibility mapping predicts amyloid-β-related cognitive decline. Brain. Oxford University Press; 2017;140(8):2112–2119. doi: 10.1093/brain/awx137.

40. O'Callaghan J, Holmes H, Powell N, et al. Tissue magnetic susceptibility mapping as a marker of tau pathology in Alzheimer's disease. Neuroimage. Academic Press Inc.; 2017;159:334–345. doi: 10.1016/j.neuroimage.2017.08.003.

41. Kim HG, Park S, Rhee HY, et al. Quantitative susceptibility mapping to evaluate the early stage of Alzheimer's disease. NeuroImage Clin. Elsevier Inc.; 2017;16:429–438. doi: 10.1016/j.nicl.2017.08.019.

42. Cogswell PM, Wiste HJ, Senjem ML, et al. Associations of quantitative susceptibility mapping with Alzheimer's disease clinical and imaging markers. Neuroimage. Academic Press Inc.; 2021;224:117433. doi: 10.1016/j.neuroimage.2020.117433.

43. Lotfipour AK, Wharton S, Schwarz ST, et al. High resolution magnetic susceptibility mapping of the substantia nigra in Parkinson's disease. J Magn Reson Imaging. 2012;35(1):48–55. doi: 10.1002/jmri.22752.

44. Barbosa JHO, Santos AC, Tumas V, et al. Quantifying brain iron deposition in patients with Parkinson's disease using quantitative susceptibility mapping, R2 and R2*. Magn Reson Imaging. 2015;33(5):559–565. doi: 10.1016/j.mri.2015.02.021.

45. Langkammer C, Pirpamer L, Seiler S, et al. Quantitative Susceptibility Mapping in Parkinson's Disease. Kassubek J, editor. PLoS One. Public Library of Science; 2016;11(9):e0162460. doi: 10.1371/journal.pone.0162460.

46. Sjöström H, Granberg T, Westman E, Svenningsson P. Quantitative susceptibility mapping differentiates between parkinsonian disorders. Park Relat Disord. Elsevier Ltd; 2017;44:51–57. doi: 10.1016/j.parkreldis.2017.08.029.

47. Ito K, Ohtsuka C, Yoshioka K, et al. Differential diagnosis of parkinsonism by a combined use of diffusion kurtosis imaging and quantitative susceptibility mapping. Neuroradiology. Springer Verlag; 2017;59(8):759–769. doi: 10.1007/s00234-017-1870-7.

48. Guan X, Xuan M, Gu Q, et al. Regionally progressive accumulation of iron in

Parkinson's disease as measured by quantitative susceptibility mapping. NMR Biomed. John Wiley and Sons Ltd; 2017;30(4):e3489. doi: 10.1002/nbm.3489.

49. Acosta-Cabronero J, Cardenas-Blanco A, Betts MJ, et al. The whole-brain pattern of magnetic susceptibility perturbations in Parkinson's disease. Brain. 2017;140:118–131. doi: 10.1093/brain/aww278.

50. Bergsland N, Zivadinov R, Schweser F, Hagemeier J, Lichter D, Guttuso T. Ventral posterior substantia nigra iron increases over 3 years in Parkinson's disease. Mov Disord. John Wiley and Sons Inc.; 2019;34(7):1006–1013. doi: 10.1002/mds.27730.

51. Mazzucchi S, Frosini D, Costagli M, et al. Quantitative susceptibility mapping in atypical Parkinsonisms. NeuroImage Clin. Elsevier Inc.; 2019;24:101999. doi: 10.1016/j.nicl.2019.101999.

52. Faber J, Giordano I, Jiang X, et al. Prominent White Matter Involvement in Multiple System Atrophy of Cerebellar Type. Mov Disord. John Wiley and Sons Inc.; 2020;35(5):816–824. doi: 10.1002/mds.27987.

53. Thomas GEC, Leyland LA, Schrag AE, Lees AJ, Acosta-Cabronero J, Weil RS. Brain iron deposition is linked with cognitive severity in Parkinson's disease. J Neurol Neurosurg Psychiatry. BMJ Publishing Group; 2020;91(4):418–425. doi: 10.1136/jnnp-2019-322042.

54. Schweitzer AD, Liu T, Gupta A, et al. Quantitative susceptibility mapping of the motor cortex in amyotrophic lateral sclerosis and primary lateral sclerosis. Am J Roentgenol. American Roentgen Ray Society; 2015;204(5):1086–1092. doi: 10.2214/AJR.14.13459.

55. Costagli M, Donatelli G, Biagi L, et al. Magnetic susceptibility in the deep layers of the primary motor cortex in Amyotrophic Lateral Sclerosis. NeuroImage Clin. 2016;12:965–969. doi: 10.1016/j.nicl.2016.04.011.

56. Lee JY, Lee YJ, Park DW, et al. Quantitative susceptibility mapping of the motor cortex: a comparison of susceptibility among patients with amyotrophic lateral sclerosis, cerebrovascular disease, and healthy controls. Neuroradiology. Springer Verlag; 2017;59(12):1213–1222. doi: 10.1007/s00234-017-1933-9.

57. Acosta-Cabronero J, Machts J, Schreiber S, et al. Quantitative Susceptibility MRI to Detect Brain Iron in Amyotrophic Lateral Sclerosis. Radiology. Radiological Society of North America; 2018;289(1):195–203. doi: 10.1148/radiol.2018180112.

58. Weidman EK, Schweitzer AD, Niogi SN, et al. Diffusion tensor imaging and quantitative susceptibility mapping as diagnostic tools for motor neuron disorders. Clin Imaging. Elsevier Inc.; 2019;53:6–11. doi: 10.1016/j.clinimag.2018.09.015.

59. Donatelli G, Caldarazzo Ienco E, Costagli M, et al. MRI cortical feature of bulbar impairment in patients with amyotrophic lateral sclerosis. NeuroImage Clin. Elsevier Inc.; 2019;24. doi: 10.1016/j.nicl.2019.101934.

60. Contarino VE, Conte G, Morelli C, et al. Toward a marker of upper motor neuron impairment in amyotrophic lateral sclerosis: A fully automatic investigation of

the magnetic susceptibility in the precentral cortex. Eur J Radiol. Elsevier Ireland Ltd; 2020;124. doi: 10.1016/j.ejrad.2020.108815.

61. Fritzsch D, Reiss-Zimmermann M, Trampel R, Turner R, Hoffmann KT, Schäfer A. Seven-tesla magnetic resonance imaging in wilson disease using quantitative susceptibility mapping for measurement of copper accumulation. Invest Radiol. Lippincott Williams and Wilkins; 2014;49(5):299–306. doi: 10.1097/RLI.0000000000000010.

62. Doganay S, Gumus K, Koc G, et al. Magnetic susceptibility changes in the basal ganglia and brain stem of patients with Wilson's disease: Evaluation with quantitative susceptibility mapping. Magn Reson Med Sci. Japanese Society for Magnetic Resonance in Medicine; 2018;17(1):73–79. doi: 10.2463/mrms.mp.2016-0145.

63. Dezortova M, Lescinskij A, Dusek P, et al. Multiparametric Quantitative Brain MRI in Neurological and Hepatic Forms of Wilson's Disease. J Magn Reson Imaging. John Wiley and Sons Inc.; 2020;51(6):1829–1835. doi: 10.1002/jmri.26984.

64. van Bergen JMG, Hua J, Unschuld PG, et al. Quantitative Susceptibility Mapping Suggests Altered Brain Iron in Premanifest Huntington Disease. Am J Neuroradiol. 2016;37(5):789–796. doi: 10.3174/ajnr.A4617.

65. Domínguez JFD, Ng ACL, Poudel G, et al. Iron accumulation in the basal ganglia in Huntington's disease: Cross-sectional data from the IMAGE-HD study. J Neurol Neurosurg Psychiatry. BMJ Publishing Group; 2016;87(5):545–549. doi: 10.1136/jnnp-2014-310183.

66. Chen L, Hua J, Ross CA, Cai S, van Zijl PCM, Li X. Altered brain iron content and deposition rate in Huntington's disease as indicated by quantitative susceptibility MRI. J Neurosci Res. John Wiley and Sons Inc.; 2019;97(4):467–479. doi: 10.1002/jnr.24358.

67. Langkammer C, Liu T, Khalil M, et al. Quantitative Susceptibility Mapping in Multiple Sclerosis. Radiology. 2013;267(2):551–559. doi: 10.1148/radiol.12120707.

68. Wisnieff C, Ramanan S, Olesik J, Gauthier S, Wang Y, Pitt D. Quantitative susceptibility mapping (QSM) of white matter multiple sclerosis lesions: Interpreting positive susceptibility and the presence of iron. Magn Reson Med. 2015;74(2):564–570. doi: 10.1002/mrm.25420.

69. Zhang Y, Gauthier SA, Gupta A, et al. Longitudinal change in magnetic susceptibility of new enhanced multiple sclerosis (MS) lesions measured on serial quantitative susceptibility mapping (QSM). J Magn Reson Imaging. John Wiley and Sons Inc.; 2016;44(2):426–432. doi: 10.1002/jmri.25144.

70. Straub S, Mangesius S, Emmerich J, et al. Toward quantitative neuroimaging biomarkers for Friedreich's ataxia at 7 Tesla: Susceptibility mapping, diffusion imaging, R2 and R1 relaxometry. J Neurosci Res. John Wiley & Sons, Ltd; 2020;98(11):2219–2231. doi: 10.1002/JNR.24701.

71. Ward P, Harding IH, Close TG, et al. Longitudinal evaluation of iron

concentration and atrophy in the dentate nuclei in Friedreich ataxia. Mov Disord. Mov Disord; 2019;34(3):335–343. doi: 10.1002/MDS.27606.

72. Harding IH, Raniga P, Delatycki MB, et al. Tissue atrophy and elevated iron concentration in the extrapyramidal motor system in Friedreich ataxia: the IMAGE-FRDA study. J Neurol Neurosurg Psychiatry. BMJ Publishing Group Ltd; 2016;87(11):1261–1263. doi: 10.1136/JNNP-2015-312665.

73. Liu C. Susceptibility tensor imaging. Magn Reson Med. 2010;63(6):1471–1477. doi: 10.1002/mrm.22482.

74. Liu C, Li W, Wu B, Jiang Y, Johnson GA. 3D fiber tractography with susceptibility tensor imaging. Neuroimage. 2012;59(2):1290–1298. doi: 10.1016/j.neuroimage.2011.07.096.

75. Li W, Liu C, Duong TQ, van Zijl PCM, Li X. Susceptibility tensor imaging (STI) of the brain. NMR Biomed. 2017;30(4):e3540. doi: 10.1002/nbm.3540.

76. Cronin MJ, Bowtell R. Quantifying MRI frequency shifts due to structures with anisotropic magnetic susceptibility using pyrolytic graphite sheet. Sci Rep. 2018;8:6259. doi: 10.1038/s41598-018-24650-2.

77. Lancione M, Tosetti M, Donatelli G, Cosottini M, Costagli M. The impact of white matter fiber orientation in single-acquisition quantitative susceptibility mapping. NMR Biomed. 2017;30(11). doi: 10.1002/nbm.3798.

78. Li W, Wu B, Avram A V., Liu C. Magnetic susceptibility anisotropy of human brain in vivo and its molecular underpinnings. Neuroimage. 2012;59(3):2088–2097. doi: 10.1016/j.neuroimage.2011.10.038.

79. Emmerich J, Bachert P, Ladd ME, Straub S. On the separation of susceptibility sources in quantitative susceptibility mapping: Theory and phantom validation with an in vivo application to multiple sclerosis lesions of different age. J Magn Reson. Academic Press; 2021;330:107033. doi: 10.1016/J.JMR.2021.107033.

80. Shin HG, Lee J, Yun YH, et al. χ-separation: Magnetic susceptibility source separation toward iron and myelin mapping in the brain. Neuroimage. Academic Press; 2021;240:118371. doi: 10.1016/J.NEUROIMAGE.2021.118371.

81. Cheng YCN, Neelavalli J, Haacke EM. Limitations of calculating field distributions and magnetic susceptibilities in MRI using a Fourier based method. Phys Med Biol. NIH Public Access; 2009;54(5):1169–1189. doi: 10.1088/0031-9155/54/5/005.

82. Koch KM, Papademetris X, Rothman DL, De Graaf RA. Rapid calculations of susceptibility-induced magnetostatic field perturbations for in vivo magnetic resonance. Phys Med Biol. Phys Med Biol; 2006;51(24):6381–6402. doi: 10.1088/0031-9155/51/24/007.

83. Straub S, Schneider TM, Emmerich J, et al. Suitable reference tissues for quantitative susceptibility mapping of the brain. Magn Reson Med. 2017;78(1):204–214. doi: 10.1002/mrm.26369.

84. Feng X, Deistung A, Reichenbach JR. Quantitative susceptibility mapping (QSM) and R2* in the human brain at 3 T: Evaluation of intra-scanner repeatability. Z Med Phys. Urban & Fischer; 2017; doi: 10.1016/J.ZEMEDI.2017.05.003.

85. Acosta-Cabronero J, Betts MJ, Cardenas-Blanco A, Yang S, Nestor PJ. In Vivo MRI Mapping of brain iron deposition across the adult lifespan. Neurobiol Dis. 2016;36(2):364–374. doi: 10.1523/JNEUROSCI.1907-15.2016.

86. Meineke J, Wenzel F, De Marco M, et al. Motion artifacts in standard clinical setting obscure disease-specific differences in quantitative susceptibility mapping. Phys Med Biol. Institute of Physics Publishing; 2018;63(14). doi: 10.1088/1361-6560/aacc52.

87. Mattern H, Sciarra A, Lüsebrink F, Acosta-Cabronero J, Speck O. Prospective motion correction improves high-resolution quantitative susceptibility mapping at 7T. Magn Reson Med. John Wiley and Sons Inc; 2019;81(3):1605–1619. doi: 10.1002/mrm.27509.

88. Bazin PL, Nijsse HE, van der Zwaag W, et al. Sharpness in motion corrected quantitative imaging at 7T. Neuroimage. Academic Press Inc.; 2020;222:117227. doi: 10.1016/j.neuroimage.2020.117227.

89. Elkady AM, Sun H, Wilman AH. Importance of extended spatial coverage for quantitative susceptibility mapping of iron-rich deep gray matter. Magn Reson Imaging. Elsevier; 2016;34(4):574–578. doi: 10.1016/J.MRI.2015.12.032.

90. Karsa A, Punwani S, Shmueli K, Anita Karsa C. The effect of low resolution and coverage on the accuracy of susceptibility mapping. Magn Reson Med. 2018;1–16. doi: 10.1002/mrm.27542.

91. Sood S, Urriola J, Reutens D, et al. Echo time-dependent quantitative susceptibility mapping contains information on tissue properties. Magn Reson Med. Wiley-Blackwell; 2017;77(5):1946–1958. doi: 10.1002/mrm.26281.

92. Cronin MJ, Wang N, Decker KS, Wei H, Zhu W-Z, Liu C. Exploring the origins of echo-time-dependent quantitative susceptibility mapping (QSM) measurements in healthy tissue and cerebral microbleeds. Neuroimage. 2017;149:98–113. doi: 10.1016/j.neuroimage.2017.01.053.

93. Zhou D, Cho J, Zhang J, Spincemaille P, Wang Y. Susceptibility underestimation in a high-susceptibility phantom: Dependence on imaging resolution, magnitude contrast, and other parameters. Magn Reson Med. Wiley-Blackwell; 2017;78(3):1080–1086. doi: 10.1002/mrm.26475.

94. Haacke EM, Liu S, Buch S, Zheng W, Wu D, Ye Y. Quantitative susceptibility mapping: current status and future directions. Magn. Reson. Imaging. 2015. p. 1–25. doi: 10.1016/j.mri.2014.09.004.

95. Sun H, Seres P, Wilman AH. Structural and functional quantitative susceptibility mapping from standard fMRI studies. NMR Biomed. 2016; doi: 10.1002/nbm.3619.

96. Sati P, van Gelderen P, Silva AC, et al. Micro-compartment specific T2∗ relaxation

in the brain. Neuroimage. Academic Press; 2013;77:268–278. doi: 10.1016/J.NEUROIMAGE.2013.03.005.

97. Wharton S, Bowtell R. Fiber orientation-dependent white matter contrast in gradient echo MRI. Proc Natl Acad Sci U S A. National Academy of Sciences; 2012;109(45):18559–18564. doi: 10.1073/pnas.1211075109.

98. Xu T, Foxley S, Kleinnijenhuis M, Chen WC, Miller KL. The effect of realistic geometries on the susceptibility-weighted MR signal in white matter. Magn Reson Med. John Wiley & Sons, Ltd; 2018;79(1):489–500. doi: 10.1002/mrm.26689.

99. Chen WC, Foxley S, Miller KL. Detecting microstructural properties of white matter based on compartmentalization of magnetic susceptibility. Neuroimage. Neuroimage; 2013;70:1–9. doi: 10.1016/j.neuroimage.2012.12.032.

100. Pauling L, Coryell CD. The Magnetic Properties and Structure of Hemoglobin, Oxyhemoglobin and Carbonmonoxyhemoglobin. Proc Natl Acad Sci. Proceedings of the National Academy of Sciences; 1936;22(4):210–216. doi: 10.1073/pnas.22.4.210.

101. Guyton A, Hall J. Textbook of medical physiology. Elsevier Health Sciences; 2020.

102. Spees WM, Yablonskiy DA, Oswood MC, Ackerman JJH. Water proton MR properties of human blood at 1.5 Tesla: Magnetic susceptibility, T1, T2*, T2, and non-Lorentzian signal behavior. Magn Reson Med. John Wiley and Sons Inc.; 2001;45(4):533–542. doi: 10.1002/mrm.1072.

103. Jain V, Abdulmalik O, Propert KJ, Wehrli FW. Investigating the magnetic susceptibility properties of fresh human blood for noninvasive oxygen saturation quantification. Magn Reson Med. John Wiley and Sons Inc; 2012;68(3):863–867. doi: 10.1002/mrm.23282.

104. Haacke EM, Lai S, Reichenbach JR, et al. In vivo measurement of blood oxygen saturation using magnetic resonance imaging: A direct validation of the blood oxygen level-dependent concept in functional brain imaging. Hum Brain Mapp. Hum Brain Mapp; 1997;5(5):341–346. doi: 10.1002/(SICI)1097-0193(1997)5:5<341::AID-HBM2>3.0.CO;2-3.

105. Uwano I, Kudo K, Sato R, et al. Noninvasive Assessment of Oxygen Extraction Fraction in Chronic Ischemia Using Quantitative Susceptibility Mapping at 7 Tesla. Stroke. Lippincott Williams and Wilkins; 2017;48(8):2136–2141. doi: 10.1161/STROKEAHA.117.017166.

106. Fan AP, Khalil AA, Fiebach JB, et al. Elevated brain oxygen extraction fraction measured by MRI susceptibility relates to perfusion status in acute ischemic stroke. J Cereb Blood Flow Metab. SAGE Publications Ltd; 2020;40(3):539–551. doi: 10.1177/0271678X19827944.

107. Finnerty E, Ramasawmy R, O'Callaghan J, et al. Noninvasive quantification of oxygen saturation in the portal and hepatic veins in healthy mice and those with colorectal liver metastases using QSM MRI. Magn Reson Med. John Wiley and Sons Inc; 2019;81(4):2666–2675. doi: 10.1002/mrm.27571.

108. Tsvetanov KA, Henson RNA, Rowe JB. Separating vascular and neuronal effects of age on fMRI BOLD signals. Philos Trans R Soc B. 2021;376:20190631. doi: 10.1098/rstb.2019.0631.

109. SMART - Servier Medical ART. 2021. https://smart.servier.com/.

110. Balla DZ, Sanchez-Panchuelo RM, Wharton SJ, et al. Functional quantitative susceptibility mapping (fQSM). Neuroimage. 2014;100:112–124. doi: 10.1016/j.neuroimage.2014.06.011.

111. Bianciardi M, van Gelderen P, Duyn JH. Investigation of BOLD fMRI resonance frequency shifts and quantitative susceptibility changes at 7 T. Hum Brain Mapp. 2014;35(5):2191–2205. doi: 10.1002/hbm.22320.

112. Chen Z, Liu J, Calhoun VD. Susceptibility-based functional brain mapping by 3D deconvolution of an MR-phase activation map. J Neurosci Methods. Elsevier; 2013;216(1):33–42. doi: 10.1016/j.jneumeth.2013.03.003.

113. Özbay PS, Warnock G, Rossi C, et al. Probing neuronal activation by functional quantitative susceptibility mapping under a visual paradigm: A group level comparison with BOLD fMRI and PET. Neuroimage. 2016;137:52–60. doi: 10.1016/j.neuroimage.2016.05.013.

114. Costagli M, Lancione M, Cecchetti L, et al. Quantitative Susceptibility Mapping of Brain Function during Auditory Stimulation. IEEE Trans Radiat Plasma Med Sci. 2019;1–1. doi: 10.1109/TRPMS.2019.2894262.

115. Shih C-M, Lo H-C, Hsieh M-C, Chen J-H. Functional Quantitative Susceptibility mapping (fQSM) of Rat Brain during Flashing Light Stimulation. Neuroimage. Academic Press; 2021;117924. doi: 10.1016/j.neuroimage.2021.117924.

116. Lancione M, Donatelli G, Cecchi P, Cosottini M, Tosetti M, Costagli M. Echo-time dependency of quantitative susceptibility mapping reproducibility at different magnetic field strengths. Neuroimage. 2019;197:557–564. doi: 10.1016/j.neuroimage.2019.05.004.

117. de Rochefort L, Liu T, Kressler B, et al. Quantitative susceptibility map reconstruction from MR phase data using bayesian regularization: Validation and application to brain imaging. Magn Reson Med. Wiley Subscription Services, Inc., A Wiley Company; 2010;63(1):194–206. doi: 10.1002/mrm.22187.

118. Wang Y, Liu T. Quantitative susceptibility mapping (QSM): Decoding MRI data for a tissue magnetic biomarker. Magn Reson Med. 2015;73(1):82–101. doi: 10.1002/mrm.25358.

119. Deistung A, Schweser F, Reichenbach JR. Overview of quantitative susceptibility mapping. NMR Biomed. 2016; doi: 10.1002/nbm.3569.

120. Liu C, Li W, Tong KA, Yeom KW, Kuzminski S. Susceptibility-weighted imaging and quantitative susceptibility mapping in the brain. J. Magn. Reson. Imaging. 2015. p. 23–41. doi: 10.1002/jmri.24768.

121. Reichenbach JR, Schweser F, Serres B, Deistung A. Quantitative Susceptibility

Mapping: Concepts and Applications. Clin Neuroradiol. Springer Berlin Heidelberg; 2015;25(S2):225–230. doi: 10.1007/s00062-015-0432-9.

122. Li X, Allen RP, Earley CJ, et al. Brain iron deficiency in idiopathic restless legs syndrome measured by quantitative magnetic susceptibility at 7 tesla. Sleep Med. Elsevier; 2016;22:75–82. doi: 10.1016/J.SLEEP.2016.05.001.

123. Li X, Harrison DM, Liu H, et al. Magnetic susceptibility contrast variations in multiple sclerosis lesions. J Magn Reson Imaging. 2016;43(2):463–473. doi: 10.1002/jmri.24976.

124. Schmalbrock XP, Prakash RS, Schirda B, et al. Basal Ganglia Iron in Patients with Multiple Sclerosis Measured with 7T Quantitative Susceptibility Mapping Correlates with Inhibitory Control. Am J Neuroradiol. 2016;37:439–446. doi: 10.3174/ajnr.A4599.

125. Betts MJ, Acosta-Cabronero J, Cardenas-Blanco A, Nestor PJ, Düzel E. High-resolution characterisation of the aging brain using simultaneous quantitative susceptibility mapping (QSM) and R2* measurements at 7 T. Neuroimage. Academic Press Inc.; 2016;138:43–63. doi: 10.1016/j.neuroimage.2016.05.024.

126. Bian W, Tranvinh E, Tourdias T, et al. In Vivo 7T MR Quantitative Susceptibility Mapping Reveals Opposite Susceptibility Contrast between Cortical and White Matter Lesions in Multiple Sclerosis. Am J Neuroradiol. 2016;37(10):1808–1815. doi: 10.3174/ajnr.A4830.

127. Cronin MJ, Wharton S, Al-Radaideh A, et al. A comparison of phase imaging and quantitative susceptibility mapping in the imaging of multiple sclerosis lesions at ultrahigh field. Magn Reson Mater Physics, Biol Med. 2016;29(3):543–557. doi: 10.1007/s10334-016-0560-5.

128. Harrison DM, Li X, Liu H, et al. Lesion Heterogeneity on High-Field Susceptibility MRI Is Associated with Multiple Sclerosis Severity. Am J Neuroradiol. 2016;37(8):1447–1453. doi: 10.3174/ajnr.A4726.

129. Chen W, Gauthier SA, Gupta A, et al. Quantitative Susceptibility Mapping of Multiple Sclerosis Lesions at Various Ages. Radiology. 2014;271(1):183–192. doi: 10.1148/radiol.13130353.

130. Deh K, Nguyen TD, Eskreis-Winkler S, et al. Reproducibility of quantitative susceptibility mapping in the brain at two field strengths from two vendors. J Magn Reson Imaging. 2015;42(6):1592–1600. doi: 10.1002/jmri.24943.

131. Lin P-Y, Chao T-C, Wu M-L. Quantitative susceptibility mapping of human brain at 3T: a multisite reproducibility study. AJNR Am J Neuroradiol. 2015;36(3):467–474. doi: 10.3174/ajnr.A4137.

132. Wang R, Xie G, Zhai M, et al. Stability of R2* and quantitative susceptibility mapping of the brain tissue in a large scale multi-center study. Sci Rep. Nature Publishing Group; 2017;7:45261. doi: 10.1038/srep45261.

133. Santin MD, Didier M, Valabrègue R, et al. Reproducibility of R 2 * and quantitative susceptibility mapping (QSM) reconstruction methods in the basal

ganglia of healthy subjects. NMR Biomed. 2017;30(4):e3491. doi: 10.1002/nbm.3491.

134. Hinoda T, Fushimi Y, Okada T, et al. Quantitative Susceptibility Mapping at 3 T and 1.5 T. Invest Radiol. 2015;50(8):522–530. doi: 10.1097/RLI.0000000000000159.

135. Deh K, Kawaji K, Bulk M, et al. Multicenter reproducibility of quantitative susceptibility mapping in a gadolinium phantom using MEDI+0 automatic zero referencing. Magn Reson Med. Wiley-Blackwell; 2018;81(2):1229–1236. doi: 10.1002/mrm.27410.

136. Jenkinson M, Beckmann CF, Behrens TEJ, Woolrich MW, Smith SM. FSL. Neuroimage. 2012;62:782–790. doi: 10.1016/j.neuroimage.2011.09.015.

137. Smith SM. Fast robust automated brain extraction. Hum Brain Mapp. 2002;17(3):143–155. doi: 10.1002/hbm.10062.

138. Liu C. STI Suite. 2017. https://people.eecs.berkeley.edu/~chunlei.liu/software.html.

139. Denk C, Rauscher A. Susceptibility weighted imaging with multiple echoes. J Magn Reson Imaging. 2010;31(1):185–191. doi: 10.1002/jmri.21995.

140. Chen Z, Robinson J, Caprihan A, Calhoun V. High-resolution human brain functional χ mapping reveals focal and bidirectional BOLD responses. Biomed Phys Eng Express. IOP Publishing; 2017;3(1):015027. doi: 10.1088/2057-1976/aa5cc7.

141. Yablonskiy DA, Sukstanskii AL. Effects of biological tissue structural anisotropy and anisotropy of magnetic susceptibility on the gradient echo MRI signal phase: theoretical background. NMR Biomed. 2017;30(4):e3655. doi: 10.1002/nbm.3655.

142. Wu B, Li W, Avram AV, Gho S-M, Liu C. Fast and tissue-optimized mapping of magnetic susceptibility and T2* with multi-echo and multi-shot spirals. Neuroimage. NIH Public Access; 2012;59(1):297–305. doi: 10.1016/j.neuroimage.2011.07.019.

143. Li W, Avram A V, Wu B, Xiao X, Liu C. Integrated Laplacian-based phase unwrapping and background phase removal for quantitative susceptibility mapping. NMR Biomed. NIH Public Access; 2014;27(2):219–227. doi: 10.1002/nbm.3056.

144. Langkammer C, Schweser F, Shmueli K, et al. Quantitative susceptibility mapping: Report from the 2016 reconstruction challenge. Magn Reson Med. Wiley-Blackwell; 2018;79(3):1661–1673. doi: 10.1002/mrm.26830.

145. Schweser F, Deistung A, Sommer K, Reichenbach JR. Toward online reconstruction of quantitative susceptibility maps: Superfast dipole inversion. Magn Reson Med. John Wiley & Sons, Ltd; 2013;69(6):1581–1593. doi: 10.1002/mrm.24405.

146. Gilman S, Wenning GK, Low PA, et al. Second consensus statement on the diagnosis of multiple system atrophy. Neurology. Lippincott Williams and

Wilkins; 2008;71(9):670–676. doi: 10.1212/01.wnl.0000324625.00404.15.

147. Berg D, Hochstrasser H. Iron metabolism in parkinsonian syndromes. Mov Disord. John Wiley and Sons Inc.; 2006;21(9):1299–1310. doi: 10.1002/mds.21020.

148. Dickson DW, Lin WL, Liu WK, Yen SH. Multiple system atrophy: A sporadic synucleinopathy. Brain Pathol. International Society of Neuropathology; 1999. p. 721–732. doi: 10.1111/j.1750-3639.1999.tb00553.x.

149. Jellinger KA. Neuropathological spectrum of synucleinopathies. Mov Disord. John Wiley and Sons Inc.; 2003;18(S6):2–12. doi: 10.1002/mds.10557.

150. Dexter DT, Carayon A, Javoy-agid F, et al. Alterations in the levels of iron, ferritin and other trace metals in parkinson's disease and other neurodegenerative diseases affecting the basal ganglia. Brain. Brain; 1991;114(4):1953–1975. doi: 10.1093/brain/114.4.1953.

151. Matsusue E, Fujii S, Kanasaki Y, Kaminou T, Ohama E, Ogawa T. Cerebellar lesions in multiple system atrophy: Postmortem MR imaging - Pathologic correlations. Am J Neuroradiol. American Society of Neuroradiology; 2009;30(9):1725–1730. doi: 10.3174/ajnr.A1662.

152. Guan X, Huang P, Zeng Q, et al. Quantitative susceptibility mapping as a biomarker for evaluating white matter alterations in Parkinson's disease. Brain Imaging Behav. Springer New York LLC; 2019;13(1):220–231. doi: 10.1007/s11682-018-9842-z.

153. Wang EW, Du G, Lewis MM, et al. Multimodal MRI evaluation of parkinsonian limbic pathologies. Neurobiol Aging. Elsevier Inc.; 2019;76:194–200. doi: 10.1016/j.neurobiolaging.2019.01.004.

154. Azuma M, Hirai T, Nakaura T, et al. Combining quantitative susceptibility mapping to the morphometric index in differentiating between progressive supranuclear palsy and Parkinson's disease. J Neurol Sci. Elsevier B.V.; 2019;406. doi: 10.1016/j.jns.2019.116443.

155. Sugiyama A, Sato N, Kimura Y, et al. Quantifying iron deposition in the cerebellar subtype of multiple system atrophy and spinocerebellar ataxia type 6 by quantitative susceptibility mapping. J Neurol Sci. Elsevier B.V.; 2019;407:116525. doi: 10.1016/j.jns.2019.116525.

156. Wharton S, Bowtell R. Effects of white matter microstructure on phase and susceptibility maps. Magn Reson Med. 2015;73(3):1258–1269. doi: 10.1002/mrm.25189.

157. Biondetti E, Karsa A, David |, Thomas L, Shmueli K. Investigating the accuracy and precision of TE-dependent versus multi-echo QSM using Laplacian-based methods at 3 T. Magn Reson Med. 2020;84(6):3040–3053. doi: 10.1002/mrm.28331.

158. Zhang Y, Yang M, Wang F, et al. Histogram Analysis of Quantitative Susceptibility Mapping for the Diagnosis of Parkinson's Disease. Acad Radiol. 2020; doi: 10.1016/j.acra.2020.10.027.

159. Avants BB, Epstein CL, Grossman M, Gee JC. Symmetric diffeomorphic image registration with cross-correlation: Evaluating automated labeling of elderly and neurodegenerative brain. Med Image Anal. Elsevier; 2008;12(1):26–41. doi: 10.1016/j.media.2007.06.004.

160. Xiao Y, Fonov V, Chakravarty MM, et al. A dataset of multi-contrast population-averaged brain MRI atlases of a Parkinson's disease cohort. Data Br. Elsevier Inc.; 2017;12:370–379. doi: 10.1016/j.dib.2017.04.013.

161. Pauli WM, Nili AN, Tyszka & JM. Data Descriptor: A high-resolution probabilistic in vivo atlas of human subcortical brain nuclei. Sci Data. 2018;5:180063. doi: 10.1038/sdata.2018.63.

162. He N, Langley J, Huddleston DE, et al. Improved Neuroimaging Atlas of the Dentate Nucleus. Cerebellum. Springer New York LLC; 2017;16(5–6):951–956. doi: 10.1007/s12311-017-0872-7.

163. Spincemaille P, Anderson J, Wu G, et al. Quantitative Susceptibility Mapping: MRI at 7T versus 3T. J Neuroimaging. 2019;jon.12669. doi: 10.1111/jon.12669.

164. Rua C, Clarke WT, Driver ID, et al. Multi-centre, multi-vendor reproducibility of 7T QSM and R_2* in the human brain: results from the UK7T study. bioRxiv. Cold Spring Harbor Laboratory; 2020;2020.04.22.055624. doi: 10.1101/2020.04.22.055624.

165. Kim EY, Sung YH, Shin HG, Noh Y, Nam Y, Lee J. Diagnosis of early-stage idiopathic parkinson's disease using high-resolution quantitative susceptibility mapping combined with histogram analysis in the substantia nigra at 3 t. J Clin Neurol. Korean Neurological Association; 2018;14(1):90–97. doi: 10.3988/jcn.2018.14.1.90.

166. Li G, Zhai G, Zhao X, et al. 3D texture analyses within the substantia nigra of Parkinson's disease patients on quantitative susceptibility maps and R2 ∗ maps. Neuroimage. Academic Press Inc.; 2019;188:465–472. doi: 10.1016/j.neuroimage.2018.12.041.

167. Xiao B, He N, Wang Q, et al. Quantitative susceptibility mapping based hybrid feature extraction for diagnosis of Parkinson's disease. NeuroImage Clin. Elsevier Inc.; 2019;24:102070. doi: 10.1016/j.nicl.2019.102070.

168. Cheng Z, Zhang J, He N, et al. Radiomic Features of the Nigrosome-1 Region of the Substantia Nigra: Using Quantitative Susceptibility Mapping to Assist the Diagnosis of Idiopathic Parkinson's Disease. Front Aging Neurosci. Frontiers Media S.A.; 2019;11(JUL):167. doi: 10.3389/fnagi.2019.00167.

169. Balestrino R, Schapira AHV. Parkinson disease. Eur. J. Neurol. Blackwell Publishing Ltd; 2020. p. 27–42. doi: 10.1111/ene.14108.

170. Gibb WRG, Lees AJ. The relevance of the Lewy body to the pathogenesis of idiopathic Parkinson's disease. J. Neurol. Neurosurg. Psychiatry. BMJ Publishing Group; 1988. p. 745–752. doi: 10.1136/jnnp.51.6.745.

171. Fearnley JM, Lees AJ. Ageing and parkinson's disease: Substantia nigra regional

selectivity. Brain. Brain; 1991;114(5):2283–2301. doi: 10.1093/brain/114.5.2283.

172. Schenck CH, Bundlie SR, Ettinger MG, Mahowald MW. Chronic behavioral disorders of human REM sleep: A new category of parasomnia. Sleep. Sleep; 1986;9(2):293–308. doi: 10.1093/sleep/9.2.293.

173. Galbiati A, Verga L, Giora E, Zucconi M, Ferini-Strambi L. The risk of neurodegeneration in REM sleep behavior disorder: A systematic review and meta-analysis of longitudinal studies. Sleep Med. Rev. W.B. Saunders Ltd; 2019. p. 37–46. doi: 10.1016/j.smrv.2018.09.008.

174. Kang SH, Yoon IY, Lee SD, Han JW, Kim TH, Kim KW. REM sleep behavior disorder in the Korean elderly population: Prevalence and clinical characteristics. Sleep. Sleep; 2013;36(8):1147–1152. doi: 10.5665/sleep.2874.

175. Pujol M, Pujol J, Alonso T, et al. Idiopathic REM sleep behavior disorder in the elderly Spanish community: a primary care center study with a two-stage design using video-polysomnography. Sleep Med. Elsevier B.V.; 2017;40:116–121. doi: 10.1016/j.sleep.2017.07.021.

176. Haba-Rubio J, Frauscher B, Marques-Vidal P, et al. Prevalence and determinants of rapid eye movement sleep behavior disorder in the general population. Sleep. Oxford University Press; 2018;41(2). doi: 10.1093/sleep/zsx197.

177. Yao CW, Saha-Chaudhuri P, Zolfaghari S, Pelletier A, Postuma RB. Phenoconversion from Possible REM Sleep Behavior to Parkinsonism in the Population-Based CLSA. Mov. Disord. John Wiley and Sons Inc; 2021. doi: 10.1002/mds.28571.

178. Boeve BF, Silber MH, Ferman TJ, et al. Clinicopathologic correlations in 172 cases of rapid eye movement sleep behavior disorder with or without a coexisting neurologic disorder. Sleep Med. Sleep Med; 2013;14(8):754–762. doi: 10.1016/j.sleep.2012.10.015.

179. Blazejewska AI, Schwarz ST, Pitiot A, et al. Visualization of nigrosome 1 and its loss in PD: Pathoanatomical correlation and in vivo 7 T MRI. Neurology. Neurology; 2013;81(6):534–540. doi: 10.1212/WNL.0b013e31829e6fd2.

180. Cosottini M, Frosini D, Pesaresi I, et al. MR imaging of the substantia nigra at 7 T enables diagnosis of parkinson disease. Radiology. Radiological Society of North America Inc.; 2014;271(3):831–838. doi: 10.1148/radiol.14131448.

181. Cosottini M, Frosini D, Pesaresi I, et al. Comparison of 3T and 7T susceptibility-weighted angiography of the substantia nigra in diagnosing Parkinson disease. Am J Neuroradiol. American Society of Neuroradiology; 2015;36(3):461–466. doi: 10.3174/ajnr.A4158.

182. Frosini D, Cosottini M, Donatelli G, et al. Seven tesla MRI of the substantia nigra in patients with rapid eye movement sleep behavior disorder. Park Relat Disord. Elsevier Ltd; 2017;43:105–109. doi: 10.1016/j.parkreldis.2017.08.002.

183. De Marzi R, Seppi K, Högl B, et al. Loss of dorsolateral nigral hyperintensity on 3.0 tesla susceptibility-weighted imaging in idiopathic rapid eye movement sleep

behavior disorder. Ann Neurol. John Wiley and Sons Inc.; 2016;79(6):1026–1030. doi: 10.1002/ana.24646.

184. Barber TR, Griffanti L, Bradley KM, et al. Nigrosome 1 imaging in REM sleep behavior disorder and its association with dopaminergic decline. Ann Clin Transl Neurol. Wiley-Blackwell; 2020;7(1):26–35. doi: 10.1002/acn3.50962.

185. Murakami Y, Kakeda S, Watanabe K, et al. Usefulness of quantitative susceptibility mapping for the diagnosis of Parkinson disease. Am J Neuroradiol. American Society of Neuroradiology; 2015;36(6):1102–1108. doi: 10.3174/ajnr.A4260.

186. An H, Zeng X, Niu T, et al. Quantifying iron deposition within the substantia nigra of Parkinson's disease by quantitative susceptibility mapping. J Neurol Sci. Elsevier B.V.; 2018;386:46–52. doi: 10.1016/j.jns.2018.01.008.

187. Sun J, Lai Z, Ma J, et al. Quantitative Evaluation of Iron Content in Idiopathic Rapid Eye Movement Sleep Behavior Disorder. Mov Disord. John Wiley and Sons Inc.; 2020;35(3):478–485. doi: 10.1002/mds.27929.

188. Xuan M, Guan X, Gu Q, et al. Different iron deposition patterns in early- and middle-late-onset Parkinson's disease. Park Relat Disord. Elsevier Ltd; 2017;44:23–27. doi: 10.1016/j.parkreldis.2017.08.013.

189. Du G, Lewis MM, Sica C, et al. Distinct progression pattern of susceptibility MRI in the substantia nigra of Parkinson's patients. Mov Disord. John Wiley and Sons Inc.; 2018;33(9):1423–1431. doi: 10.1002/mds.27318.

190. Chen Q, Chen Y, Zhang Y, et al. Iron deposition in Parkinson's disease by quantitative susceptibility mapping. BMC Neurosci. BioMed Central Ltd.; 2019;20(1):23. doi: 10.1186/s12868-019-0505-9.

191. Takahashi H, Watanabe Y, Tanaka H, et al. Comprehensive MRI quantification of the substantia nigra pars compacta in Parkinson's disease. Eur J Radiol. Elsevier Ireland Ltd; 2018;109:48–56. doi: 10.1016/j.ejrad.2018.06.024.

192. Iranzo A, Lomeña F, Stockner H, et al. Decreased striatal dopamine transporter uptake and substantia nigra hyperechogenicity as risk markers of synucleinopathy in patients with idiopathic rapid-eye-movement sleep behaviour disorder: A prospective study. Lancet Neurol. 2010;9(11):1070–1077. doi: 10.1016/S1474-4422(10)70216-7.

193. Bae YJ, Kim JM, Kim KJ, et al. Loss of substantia nigra hyperintensity at 3.0-T MR imaging in idiopathic REM sleep behavior disorder: Comparison with 123I-FP-CIT SPECT. Radiology. Radiological Society of North America Inc.; 2018;287(1):285–293. doi: 10.1148/radiol.2017162486.

194. American Academy of Sleep Medicine. International Classification of Sleep Disorders – Third Edition (ICSD-3). 2014.

195. Hoehn MM, Yahr MD. Parkinsonism : onset, progression, and mortality. Neurology. 1967;17(5):427–442. http://www.neurology.org/content/17/5/427.citation. Accessed April 21, 2021.

196. Cox RW. AFNI: Software for Analysis and Visualization of Functional Magnetic Resonance Neuroimages. Comput Biomed Res. Academic Press; 1996;29(3):162–173. doi: 10.1006/CBMR.1996.0014.

197. Du G, Liu T, Lewis MM, et al. Quantitative susceptibility mapping of the midbrain in Parkinson's disease. Mov Disord. John Wiley and Sons Inc.; 2016;31(3):317–324. doi: 10.1002/mds.26417.

198. Takahashi H, Watanabe Y, Tanaka H, et al. Quantifying changes in nigrosomes using quantitative susceptibility mapping and neuromelanin imaging for the diagnosis of early-stage Parkinson's disease. Br J Radiol. British Institute of Radiology; 2018;91(1086). doi: 10.1259/bjr.20180037.

199. Youdim MBH, Riederer P. The role of iron in senescence of dopaminergic neurons in Parkinson's disease. J Neural Transm Suppl. 1993. p. 57–67. https://europepmc.org/article/med/8294901. Accessed May 7, 2021.

200. Kwan JY, Jeong SY, van Gelderen P, et al. Iron accumulation in deep cortical layers accounts for MRI signal abnormalities in ALS: Correlating 7 tesla MRI and pathology. PLoS One. Public Library of Science; 2012;7(4):35241. doi: 10.1371/journal.pone.0035241.

201. Bulk M, Abdelmoula WM, Nabuurs RJA, et al. Postmortem MRI and histology demonstrate differential iron accumulation and cortical myelin organization in early- and late-onset Alzheimer's disease. Neurobiol Aging. Elsevier Inc.; 2018;62:231–242. doi: 10.1016/j.neurobiolaging.2017.10.017.

202. Pyatigorskaya N, Gaurav R, Arnaldi D, et al. Magnetic resonance imaging biomarkers to assess substantia nigra damage in idiopathic rapid eye movement sleep behavior disorder. Sleep. Oxford University Press; 2017;40(11). doi: 10.1093/sleep/zsx149.

203. Lee JH, Han YH, Cho JW, et al. Evaluation of brain iron content in idiopathic REM sleep behavior disorder using quantitative magnetic resonance imaging. Park Relat Disord. Elsevier Ltd; 2014;20(7):776–778. doi: 10.1016/j.parkreldis.2014.03.023.

204. Zhang X, Chai C, Ghassaban K, et al. Assessing brain iron and volume of subcortical nuclei in idiopathic rapid eye movement sleep behavior disorder. Sleep. 2021; doi: 10.1093/sleep/zsab131.

205. Chen Q, Boeve BF, Forghanian-Arani A, et al. MRI quantitative susceptibility mapping of the substantia nigra as an early biomarker for Lewy body disease. J Neuroimaging. J Neuroimaging; 2021;jon.12878. doi: 10.1111/jon.12878.

206. Biondetti E, Santin MD, Valabrègue R, et al. The spatiotemporal changes in dopamine, neuromelanin and iron characterizing Parkinson's disease. Brain. 2021;144. doi: 10.1093/brain/awab191/6274641.

207. He N, Ling H, Ding B, et al. Region-specific disturbed iron distribution in early idiopathic Parkinson's disease measured by quantitative susceptibility mapping. Hum Brain Mapp. John Wiley and Sons Inc.; 2015;36(11):4407–4420. doi:

10.1002/hbm.22928.

208. Cheng Z, He N, Huang P, et al. Imaging the Nigrosome 1 in the substantia nigra using susceptibility weighted imaging and quantitative susceptibility mapping: An application to Parkinson's disease. NeuroImage Clin. Elsevier Inc.; 2020;25:102103. doi: 10.1016/j.nicl.2019.102103.

209. Noh Y, Sung YH, Lee J, Kim EY. Nigrosome 1 detection at 3T MRI for the diagnosis of early-stage idiopathic Parkinson disease: Assessment of diagnostic accuracy and agreement on imaging asymmetry and clinical laterality. Am J Neuroradiol. American Society of Neuroradiology; 2015;36(11):2010–2016. doi: 10.3174/ajnr.A4412.

210. Schwarz ST, Afzal M, Morgan PS, Bajaj N, Gowland PA, Auer DP. The "swallow tail" appearance of the healthy nigrosome - A new accurate test of Parkinson's disease: A case-control and retrospective cross-sectional MRI study at 3T. PLoS One. Public Library of Science; 2014;9(4). doi: 10.1371/journal.pone.0093814.

211. Lancione M, Costagli M, Handjaras G, et al. Complementing canonical fMRI with functional Quantitative Susceptibility Mapping (fQSM) in modern neuroimaging research. Neuroimage. 2021;244:118574. doi: 10.1016/J.NEUROIMAGE.2021.118574.

212. Chen W, Zhu W, Kovanlikaya Ii, et al. Intracranial Calcifications and Hemorrhages: Characterization with Quantitative Susceptibility Mapping. Radiology. 2014;270(2):496–505. doi: 10.1148/radiol.13122640.

213. Sun H, Klahr AC, Kate M, et al. Quantitative susceptibility mapping for following intracranial hemorrhage. Radiology. Radiological Society of North America Inc.; 2018;288(3):830–839. doi: 10.1148/radiol.2018171918.

214. Acosta-Cabronero J, Cardenas-Blanco A, Betts MJ, et al. The whole-brain pattern of magnetic susceptibility perturbations in Parkinson's disease. Brain. 2017;140(1):118–131. doi: 10.1093/brain/aww278.

215. Chen Z, Calhoun V. Intrinsic functional brain mapping in reconstructed 4D magnetic susceptibility (χ) data space. J Neurosci Methods. 2015;241:85–93. doi: 10.1016/j.jneumeth.2014.12.014.

216. Sun H, Wilman AH. Quantitative susceptibility mapping using single-shot echo-planar imaging. Magn Reson Med. John Wiley and Sons Inc; 2015;73(5):1932–1938. doi: 10.1002/mrm.25316.

217. Dumoulin SO, Wandell BA. Population receptive field estimates in human visual cortex. Neuroimage. 2008;39(2):647–660. doi: 10.1016/j.neuroimage.2007.09.034.

218. Kriegeskorte N, Mur M, Bandettini P. Representational similarity analysis - connecting the branches of systems neuroscience. Front Syst Neurosci. Frontiers Media SA; 2008;2:4. doi: 10.3389/neuro.06.004.2008.

219. Zwicker E. Subdivision of the Audible Frequency Range into Critical Bands (Frequenzgruppen). J Acoust Soc Am. Acoustical Society of America (ASA); 1961;33(2):248–248. doi: 10.1121/1.1908630.

220. Langers DRM, Krumbholz K, Bowtell RW, Hall DA. Neuroimaging paradigms for tonotopic mapping (I): The influence of sound stimulus type. Neuroimage. 2014;100:650–662. doi: 10.1016/j.neuroimage.2014.07.044.

221. Watson AB, Pelli DG. Quest: A Bayesian adaptive psychometric method. Percept Psychophys. Springer-Verlag; 1983;33(2):113–120. doi: 10.3758/BF03202828.

222. Marques JP, Kober T, Krueger G, van der Zwaag W, Van de Moortele PF, Gruetter R. MP2RAGE, a self bias-field corrected sequence for improved segmentation and T1-mapping at high field. Neuroimage. Neuroimage; 2010;49(2):1271–1281. doi: 10.1016/j.neuroimage.2009.10.002.

223. Wei H, Zhang Y, Gibbs E, Chen NK, Wang N, Liu C. Joint 2D and 3D phase processing for quantitative susceptibility mapping: application to 2D echo-planar imaging. NMR Biomed. 2016;(October 2015):n/a-n/a. doi: 10.1002/nbm.3501.

224. Walsh DO, Gmitro AF, Marcellin MW. Adaptive reconstruction of phased array MR imagery. Magn Reson Med. John Wiley and Sons Inc.; 2000;43(5):682–690. doi: 10.1002/(SICI)1522-2594(200005)43:5<682::AID-MRM10>3.0.CO;2-G.

225. Penny W, Friston K, Ashburner J, Kiebel S, Nichols T. Statistical Parametric Mapping: The Analysis of Functional Brain Images. Elsevier; 2011.

226. Friston KJ, Holmes AP, Worsley KJ, Poline J-P, Frith CD, Frackowiak RSJ. Statistical parametric maps in functional imaging: A general linear approach. Hum Brain Mapp. John Wiley & Sons, Ltd; 1994;2(4):189–210. doi: 10.1002/hbm.460020402.

227. Thomas JM, Huber E, Stecker GC, Boynton GM, Saenz M, Fine I. Population receptive field estimates of human auditory cortex. Neuroimage. Academic Press; 2015;105:428–439. doi: 10.1016/J.NEUROIMAGE.2014.10.060.

228. Worsley KJ, Friston KJ. Analysis of fMRI time-series revisited — Again. Neuroimage. Neuroimage; 1995;2(3):173–181. doi: 10.1006/nimg.1995.1023.

229. Gawryluk JR, Mazerolle EL, D'Arcy RCN. Does functional MRI detect activation in white matter? A review of emerging evidence, issues, and future directions. Front Neurosci. Frontiers Research Foundation; 2014;8(8 JUL). doi: 10.3389/fnins.2014.00239.

230. Li M, Newton AT, Anderson AW, Ding Z, Gore JC. Characterization of the hemodynamic response function in white matter tracts for event-related fMRI. Nat Commun. Nature Publishing Group; 2019;10(1):1–11. doi: 10.1038/s41467-019-09076-2.

231. Hernández-Torres E, Kassner N, Forkert ND, et al. Anisotropic cerebral vascular architecture causes orientation dependency in cerebral blood flow and volume measured with dynamic susceptibility contrast magnetic resonance imaging. J Cereb Blood Flow Metab. Nature Publishing Group; 2017;37(3):1108–1119.

232. Brewer AA, Barton B. Maps of the Auditory Cortex. Annu Rev Neurosci. 2016;39:385–407. doi: 10.1146/annurev-neuro-070815-014045.

233. Da Costa S, van der Zwaag W, Marques JP, Frackowiak RSJ, Clarke S, Saenz M. Human primary auditory cortex follows the shape of Heschl's gyrus. J Neurosci. Society for Neuroscience; 2011;31(40):14067–14075. doi: 10.1523/JNEUROSCI.2000-11.2011.

234. Da Costa S, Saenz M, Clarke S, van der Zwaag W. Tonotopic Gradients in Human Primary Auditory Cortex: Concurring Evidence From High-Resolution 7 T and 3 T fMRI. Brain Topogr. 2015;28(1):66–69. doi: 10.1007/s10548-014-0388-0.

235. Dick F, Tierney AT, Lutti A, Josephs O, Sereno MI, Weiskopf N. In vivo functional and myeloarchitectonic mapping of human primary auditory areas. J Neurosci. Society for Neuroscience; 2012;32(46):16095–16105. doi: 10.1523/JNEUROSCI.1712-12.2012.

236. Humphries C, Liebenthal E, Binder JR. Tonotopic organization of human auditory cortex. Neuroimage. 2010;50:1202–1211. doi: 10.1016/j.neuroimage.2010.01.046.

237. Saenz M, Langers DRM. Tonotopic mapping of human auditory cortex. Hear. Res. 2014. p. 42–52. doi: 10.1016/j.heares.2013.07.016.

238. Moerel M, De Martino F, Santoro R, et al. Processing of natural sounds: characterization of multipeak spectral tuning in human auditory cortex. J Neurosci. Society for Neuroscience; 2013;33(29):11888–11898. doi: 10.1523/JNEUROSCI.5306-12.2013.

239. Ren J, Xu T, Wang D, et al. Individual Variability in Functional Organization of the Human and Monkey Auditory Cortex. Cereb Cortex. Oxford Academic; 2021;31(5):2450–2465. doi: 10.1093/CERCOR/BHAA366.

240. Zhu X, Gao Y, Liu F, Crozier S, Sun H. Deep grey matter quantitative susceptibility mapping from small spatial coverages using deep learning. Z Med Phys. Urban & Fischer; 2021; doi: 10.1016/J.ZEMEDI.2021.06.004.

241. Logothetis NK, Pauls J, Augath M, Trinath T, Oeltermann A. Neurophysiological investigation of the basis of the fMRI signal. Nature. 2001;412(6843):150–157. doi: 10.1038/35084005.

242. Yacoub E, Shmuel A, Logothetis N, Uğurbil K. Robust detection of ocular dominance columns in humans using Hahn Spin Echo BOLD functional MRI at 7 Tesla. Neuroimage. Academic Press; 2007;37(4):1161–1177. doi: 10.1016/j.neuroimage.2007.05.020.